2023

Experimental and Numerical Studies on the Projective Dye Visualization Velocimetry in a Squared Vertical Tube

Mark Bradley Johnson
Wright State University

EXPERIMENTAL AND NUMERICAL STUDIES ON THE PROJECTIVE DYE VISUALIZATION VELOCIMETRY IN A SQUARED VERTICAL TUBE

A Dissertation submitted in partial fulfillment of the

requirements for the degree of

Doctor of Philosophy

by

MARK BRADLEY JOHNSON

B.S.M.E., Wright State University, 2015

M.S.M.E., Wright State University, 2016

2023

Wright State University

WRIGHT STATE UNIVERSITY

COLLEGE OF GRADUATE PROGRAMS AND HONORS STUDIES

14 April 2023

I HEREBY RECOMMEND THAT THE DISSERTATION PREPARED UNDER MY SUPERVISION BY MARK BRADLEY JOHNSON ENTITLED EXPERIMENTAL AND NUMERICAL STUDIES ON THE PROJECTIVE DYE VISUALIZATION VELOCIMETRY IN A SQUARED VERTICAL TUBE BE ACCEPTED IN PARTIAL FULFILLMENT OF THE REQUIREMENTS FOR THE DEGREE OF DOCTOR OF PHILOSOPHY.

_____
Zifeng Yang, Ph.D.
Dissertation Director

_____
Ahsan Mian, Ph.D.
Director, Engineering Ph.D. Program

_____
Shu Schiller, Ph.D.
Interim Dean, College of
Graduate Programs & Honors Studies

Committee on Final Examination:

_____
George Huang, Ph.D.

_____
Philippe Sucosky, Ph.D.

_____
Hamed Attariani, Ph.D.

_____
Bryan Ludwig, M.D.

ABSTRACT

Johnson, Mark Bradley. Ph.D., Engineering Ph.D. Program, Wright State University, 2023. Experimental and Numerical Studies on the Projective Dye Visualization Velocimetry in a Squared Vertical Tube

In fluid flow experiments, there have been numerous techniques developed over the years to measure velocity. Most popular techniques are non-intrusive such as particle image velocimetry (PIV), but these techniques are not suitable for all applications. For instance, PIV cannot be used in examining in-vivo measurements since the laser is not able to penetrate through the patient, which is why medical applications typically use X-rays. However, the images obtained from X-rays, in particular digital subtraction angiography, are projective images which compress 3D flow features onto a 2D image. Therefore, when intensity techniques, such as optical flow method (OFM), are applied to these images the accuracy of the velocity measurements suffer from 3D effects. To understand the error introduced in using projective images, a vertical square tube chamber was constructed to achieve various water flow rates with variable dye injection points to perform dye visualization velocimetry (DVV). The results from DVV were compared with PIV measurements to quantify the error associated with DVV. Results from DVV were comparable with PIV, but a machine learning correction method, more specifically multilayer perceptron (MLP), was needed to adjust the DVV results. To train the

MLP model, CFD simulations were conducted to generate detailed velocity distributions in the tube and projected dye images which would be used for DVV analysis and thus used as input for training. These CFD simulations were compared with PIV measurements and dye visualization images to validate proper boundary conditions and meshing. For the laminar case, MLP reduces the error associated with DVV from 35% down to 6.9%. When MLP was used to correct instantaneous DVV measurements for the turbulence cases, the error decreased from 22% to 9.8% for measurements 20 mm downstream of the dye inlet. For a time-averaged turbulent case, MLP was able to decrease the v-velocity error down to 5% and reduce the error of DVV by 50% for shear stress near the dye inlet.

Contents

List of Figures

List of Tables

1. Introduction

1.1. Velocimetry based on projective imaging

Researchers conducting experiments involving fluids have been interested in results related to wall shear stress, turbulence kinetic energy, vorticity, and streamlines. Each of these results require knowledge of the velocity field. Over the years, scientists and engineers have developed various methods for extracting or obtaining the velocity field. Early techniques involved intrusive methods such as hot-wire and pitot-static tubes, which required devices to be inserted into the flow field. Since these methods interfere with subsonic flow upstream and all flows downstream, more sophisticated methods were developed in which the flow was not disturbed or, in other terms, non-intrusive methods. These methods include particle image velocimetry, particle tracking velocimetry, and more. One non-intrusive method is generalized as projective imaging velocimetry. In general, these methods incorporate some type of ray emitting source which transmits through the fluid flow and produces a contrast projection onto an image. These images are then evaluated using an algorithm which compares the image intensity between successive images to calculate a correlation pattern of the pixel displacements. Since the time between images is known, the velocity is determined with the displacement over time. Some techniques such as Schlieren image velocimetry require only a light source, an optics system, and a camera for producing contrast images. However, most techniques require the fluid to be seeded. Seeding the flow could involve anything from smoke, fluorescent particles, dye, or even air bubbles in a liquid flow. Particle shadow velocimetry is one method which requires particles

be inserted into the flow. Other techniques use some type of dye contrast agent to provide intensity gradients in the image. These techniques include, but are not limited to, dye visualization velocimetry and digital subtraction angiography. Each of these methods have their own advantages and disadvantages, but a common trait they share is the projection of a 3D flow field onto a 2D image which will be discussed further in this paper.

1.1.1. DSA – digital subtraction angiography

The method of digital subtraction angiography (DSA) is used with x-ray imaging, where DSA subtracts high contrast structures such as bone and tissue from the image prior to iodine-contrast injection. This type of subtraction is specific to temporal subtraction since a "mask" image, or an image without contrast administered into the region, is required for subtraction. The mask image subtracts from the current x-ray image allowing visualization of dye contrast through the vessels. Contrary to film subtraction, temporal subtraction in digital radiography uses the logarithm of the transmitted x-ray intensity. The advantage of using the logarithm as opposed to the intensity itself becomes apparent when a vessel overlaps with a bone structure, because the density of the vessel in the subtracted image decreases when the overall tissue thickness increases when using intensity itself [1]. During the subtraction process, the two x-ray images must record the intensities with extremely high precision since the iodine contrast may be a small portion (1-3%) of the unsubtracted image contrast [1]. Errors associated with DSA are largely a result of motion effects. Even the smallest movement of 1 mm will cause significant distortion in the subtracted image. Causes for these movements involve uncooperative patients as well as moving structures such as the heart. More subtle movements including vascular pulsation or peristalsis can cause blurring of the image. In general, the lower the iodine concentration, the higher risk of motion generated artifacts within the image [1]. Study of carotid artery bifurcations in 100 patients was

performed to determine the quality of DSA examination. Conclusions from this study stated DSA is safe, rapid, and accurate in evaluating carotid bifurcations in 70% of the arteries examined [2]. The feasibility of using DSA in measuring blood flow velocity has been conducted where time resolved visualizations of contrast through arterial vasculature allowed researchers to calculate flow rates within 10% of velocities measured from a flow meter [3].

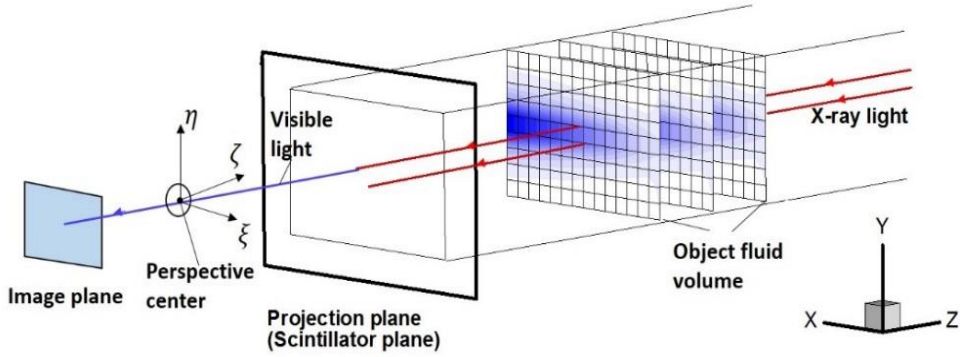

Figure 1: Depiction of x-ray angiography through an object fluid volume.

1.1.2. Schlieren image velocimetry

The "Schlieren" method was first developed and applied by Töpler in 1864 by observing changes in density of a fluid [4]. Töpler also studied compression waves emitted from a spark discharge, which was rendered visible with the Schlieren method. The method has been used in investigating forced and natural convection cooling over heated wires, which led to a relation between the schlieren photographs and temperature of the air. In general, the method produces an image of a sharp-edged stop which is illuminated by a condensing system by use of an optical element, lens or mirror. Another stop is positioned in a manner to cut off nearly all of the light with only a small fraction of light transmitting through a lens system by which an image of the main optical element is formed on a screen or viewing piece [4]. Variations of the refractive index in the fluid between the two stops causes deviations in the light rays which results in either the light being completely blocked by the second stop or passes through with more displacement

than usual. As a result, the projected image displays darker or lighter regions than the background due to modified refractive index. With respect to the optical element, the experimental setup differs if a lens or mirror is selected. Simplest arrangement uses a lens; however, the field of view must be at least as large as the lens which becomes expensive. Using a mirror results in a lower cost, but the complexity of the setup increases. These images provide a contrast amongst the varying density regions within the fluid which allows researchers to calculate the velocity with various methods such as those used in particle image velocimetry (PIV). In 2011 Hargather et al., investigated schlieren image velocimetry (SIV) measurements using a seedless method which uses naturally occurring refractive turbulent eddies in performing velocimetry [5].

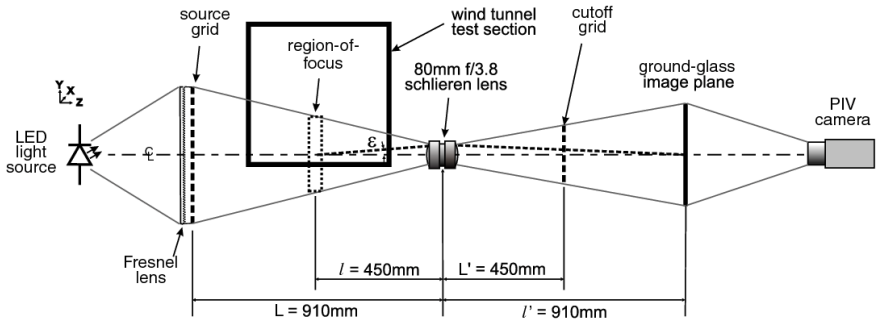

Figure 2: Schlieren image velocimetry setup based on the work of Hargather [5].

The investigators had success with a custom MATLAB code as opposed to commercial PIV algorithms for analyzing the images. This improvement was a result of the commercial's algorithm built specific to high contrast PIV images with small search windows, whereas the MATLAB code could evaluate large search windows containing hundreds of pixels. Larger search windows were necessary due to the nature of the large turbulent structures coupled with the grayscale texture of the schlieren images. Results of the SIV method in a subsonic turbulent boundary layer were compared with pitot static tubes and had comparable results. To provide

variations in the incompressible fluid, the inlet contained heating elements to provide temperature gradients. Understanding Aero-acoustic fields are important in the design process of projects containing rocket engines, which is why extensive research has been performed with laboratory-scale jets. For instance, Ozawa et al. explored the convection velocity distribution for a supersonic jet flow without a laser system by applying SIV to calculate the velocimetry field [6]. Another research team sought the convection velocity of a transverse jet operating at Mach 2 supersonic flow by implementing time-series schlieren images [7].

1.1.3. Particle shadow velocimetry

Particle shadow velocimetry (PSV) is a variant of the common practice particle image velocimetry (PIV). Most PIV systems require laser light sources which are capable of producing short, high-power pulses to illuminate seeded particles [8]. The imaging system then captures the scattered light produced by the illuminated particles. In PSV, a low-power light source namely LEDs replace the laser system which results in an in-line volume illumination of the particle. Since this illumination incorporates a 3D flow, an imaging-optics setup must be able to create a narrow depth of field for 2D plane imaging [8]. Spacers between the various lenses and camera are used to adjust the depth of field, working distance, and field of view. In creating a thin, focused plane, a large aperture is coupled with an increased spacer to decrease the depth of field [8]. Estevadeordal et al. incorporated a setup which allowed them to capture a field of view varying from millimeters to several centimeters based on the addition of more than one lens. From the post-processing perspective, the depth of field could be modified by filtering image intensities outside a designated threshold, which would be based on the particle's location from the center of the focal plane.

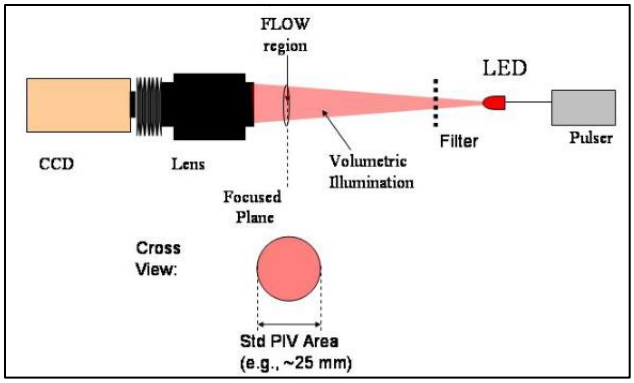

Figure 3: Particle Shadow Velocimetry setup using an LED light source along with a cross-sectional representation of the field of view [8].

Benefit of PSV is the natural simplicity of the illumination setup which results in an in-line, zero-degree-deviation direct illumination. Analyzing the shadow cast on a bright background allows for easier velocimetry as compared to techniques involving fluorescence, scattering, or tagging. Comparison between different light sources used in velocimetry such as LED vs laser sheet, concluded the differences were negligible. This technique is also applicable to internal water flow where the seeding element is gas bubbles [9]. These images were analyzed with PIV and particle tracking velocimetry (PTV) algorithms, which resulted in good agreement with turbulence parameters and velocity profiles. Researchers have demonstrated the advantages in using PSV to evaluate velocity measurements near walls, in cavities, and near model surfaces. More specifically, experiments were performed on a cylinder in cross flow and on a rearward facing step. Conclusion of these results state PSV provides well suited measurements near surfaces which would usually exhibit surface glare in laser-based PIV methods [10]. Improved PSV techniques have also been used in high-speed flow applications where the contrast of the seeding particles and the intensity of the light transmitting to the image plane have increased significantly [11]. The inexpensive technique has even extended to cost savings by using

smartphones as opposed to expensive high-speed cameras. This study used four smartphones in "slo-mo" mode to capture a time-resolved tomography of a vortex ring [12].

1.1.4. Dye Visualization velocimetry

Injecting dye into experiments has been common over the years for visualizing the fluid flow. Dye has been used in aerospace experiments for demonstrating the vortical behavior over a double delta wing with various kink angles in a water channel [13]. Another research group has studied the use of photochromic dye in two-phase flows which used a pulsed beam of UV light to activate the dye molecules and therefore resulting in a darker color in the liquid [14]. Kawaji et al., calculated the velocity by determining the displacement over consecutive images with a known elapsed time between frames. The authors, Kawaji et al., acknowledged the uncertainty in the velocity profiles begin to increase when the end point becomes unclear, but for simple flows the relative error can be as low as 2.5% [14]. Yang and Johnson have conducted research with dye visualization specific to pulsatile flow through a horizontal tube [15]. Dye was injected upstream of the test region using a syringe pump with a constant volume flow rate and images were captured with a high-speed camera. Velocity was calculated from the dye concentration through the use of the optical flow method (OFM), which compares each pixel intensity between two successive images. To determine the accuracy of the OFM velocity field, PIV was used to determine the center plane velocity and compared with the OFM results. Results revealed the dye visualization method underestimated the center plane velocity by 16%-24% in the central region and by about 29%-43% in the outer region [15]. The large discrepancy between PIV and OFM near the outer region was explained by a thick wall effect, where the light transmits through a low-speed region (near the wall), a high-speed region (further from the wall), and another low-speed region (near the wall).

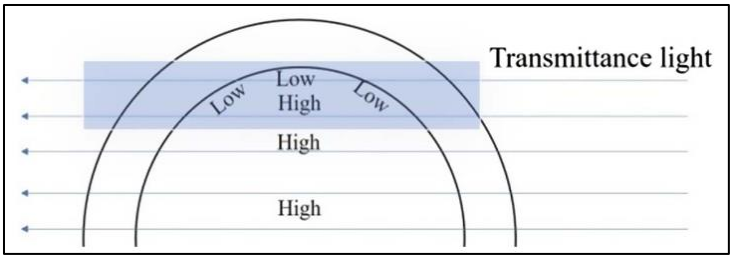

Figure 4: Illustration of light transmitting through the horizontal tube, where the light transmits through two low speed regions and one high speed region resulting in an overall low speed region [15].

Yu et al., have also used multiple dye colors in visualizing the flow patterns within the circle of Willis (COW) for an in-vitro experiment [16]. These images demonstrated how blood from two different inlets travel downstream through the COW and the amount of mixing which occurs prior to reaching the outlet.

1.2. Experimental and Numerical Analysis

This research investigates the accuracy of using projective image velocimetry, more specifically dye visualization velocimetry (DVV). Several experimental setups were used, which included pulsatile flow through a horizontal tube, pulsatile flow through an in-vitro aneurysm model, and constant flow through a vertical squared tube. The vertical flow chamber was controlled by a flow valve to achieve flow regimes between laminar and turbulent flow. Each of the experimental setups injected dye upstream of the test section, so projective images could be acquired and later evaluated for velocity measurements. LED light bulb and a high-speed camera were used in picture acquisition for DVV. To serve as a benchmark in the velocity comparison, the well-known PIV method was used. Fluorescent particles were used in seeding the water and the syringe pump contained the same seeded mixture to maintain consistency between the PIV experiment and DVV experiment. High-pass filter was attached to the camera to reduce noise in

the PIV image from undesired reflective light and therefore mitigated error in the process of calculating the velocity.

Numerical analysis was performed with commercial computational fluid dynamic (CFD) software from Cradle Co., Ltd. More specifically, SC/Tetra v2021 was used which is a general-purpose thermo-fluid program with unstructured tetrahedral mesh. Governing equations included continuity, momentum (in all directions), and the species equation for simulating dye diffusion. The use of CFD was to produce results of the dye diffusion, dye pattern, and velocity field. Validation of the simulation required comparisons with the PIV results as well as the dye movement obtained by dye visualization through time. Once these parameters were validated, the CFD simulation could be used in aiding the DVV results through a correction method based on a machine learning algorithm. Code written in MATLAB was used to generate projection images from the CFD results, where the pixel intensity was determined through a discretized form of the light attenuation equation.

2. Background

2.1. Angiographic imaging

Angiographic images are used in the medical field to visualize inside the body. Specific regions of interest include the heart, veins, cranium, and arteries. To obtain these images, x-rays are emitted towards the intended region where some of the rays are attenuated through soft tissue and bone. This attenuation causes intensity variations within the image, for instance, soft tissue will absorb less energy from the x-rays than bone which results in darker regions caused by bone. Since blood does not provide large contrast in images, the veins and/or arteries are injected with a contrast agent which provides a large contrast within the image. Typically, the contrast agent of choice is iodine due to its high k-edge value. The k-edge represents the amount of energy needed to knockout a k-shell electron, which for tissue is relatively small but iodine and barium require around 30-40 keV [17]. There are two ways in which diagnostic x-rays interact with tissue: 1) Photoelectric effect and 2) Compton scattering. Photoelectric effect occurs when a photon uses all of its energy to dislodge an electron from an atom and causes the electron to ionize neighboring atoms. This effect, however, does not involve any photon scattering. When a photon does not use all of its energy to eject an electron, the photon changes direction. This is described as Compton scattering. When the photon changes direction, the photon may return back toward the x-ray tube emitter, pass through the patient, or scatter again. Any energy from the photon interaction which is absorbed by the tissue is referred to as dose. Dose is energy per kilogram of tissue and medical professionals try to mitigate this quantity as it is not healthy for

the patient. The amount of energy absorbed, or attenuation, is governed by the Beer-Lambert law which determines the amount of radiation that passes through the patient.

$$I_{out} = I_{in}e^{-\lambda d} \quad (1)$$

Here the intensity of the radiation is denoted by I, the linear attenuation coefficient is λ, and the distance the photon travels through is indicated by d. To reduce the dosage level, medical professionals can increase the voltage which means higher photons and therefore leads to less skin attenuation which is good for larger patients [17]. However, increasing the voltage leads to reduced contrast in the image and thus the quality of the image suffers. Angiographic images have been used to detect blood clots, tumors, arterial stenosis caused by plaque build-up, arteriovenous malformation, and aneurysms [18]. These disorders can be severe and lead to serious health risks, such as the rupturing of an intracranial aneurysm.

2.2. Hemodynamics associated with vascular disease

Aneurysms occur when the blood vessel wall becomes weak and allows the pressure of the blood to create a ballooning effect on the vessel wall. There are several types of aneurysms which can occur, however the most prevalent of cerebral aneurysms are saccular. Saccular aneurysms are also referred to as “berry” aneurysms and look like a sac protruding from the vessel wall. There are two subcategories of saccular aneurysms: side wall and bifurcation [19].

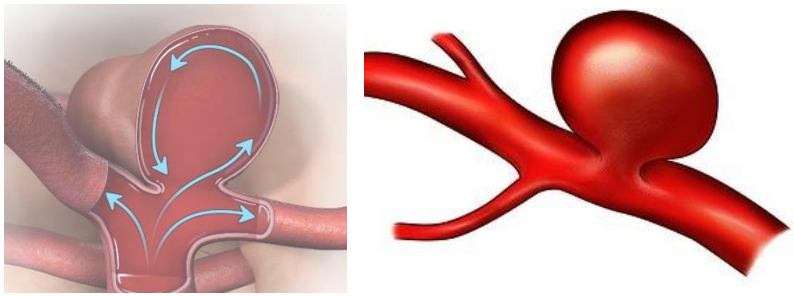

(a) (b)

Figure 5: Illustrations of the types of saccular aneurysms which include (a) bifurcation and (b) side wall [25,26].

When the saccular aneurysm is located on the lateral walls of the artery this is specified as sidewall which typically results in flow impinging on the neck of the aneurysm and very unlikely to encroach the dome [20]. Conversely, the dome of a bifurcation aneurysm is often directly affected by the blood flow jet because the parent artery splits into two or more discharging arteries. Bifurcation aneurysms commonly form in the middle cerebral artery or the basilar artery [20]. The formation of aneurysms occurs from weakening or disappearing of the internal elastic lumina (IEL), thinning of the tunica media, and remodeling of extracellular matrix (ECM) proteins [20]. The ECM proteins assist with cell adhesion and elasticity which allows cells to stretch and return to their original state. Therefore, altering the structure of the ECM proteins leads to deficiencies in retaining the vessel wall shape. Weakening the elastic lumina is a result of disrupting the signals sent by the endothelial cells to sustain vascular homeostasis [21]. There is a correlation between wall shear stress and the response signals from the endothelial cells as well as the aneurysmal shape. Since wall shear stress influences the endothelial cells and therefore the IEL, it is reasonable to study the effect of high wall shear stress and low wall shear stress on the growth of aneurysms. Previous research was conducted on the effects of wall shear stress on aneurysm growth however the results were inconclusive. There are two theories: 1)

high wall shear stress and 2) low wall shear stress. High wall shear stress was hypothesized to cause endothelial damage and vascular remodeling [22]. While low wall shear stress was theorized to cause inflammatory cell infiltration of the endothelial layer [23]. Despite the inconclusiveness of the two theories, the common trait is that the wall shear stress is important in understanding aneurysm growth. Recall wall shear stress, τ, in fluid mechanics is proportional to the velocity gradient at the wall, $\partial u/\partial y$.

$$\tau = \mu \left.\frac{\partial u}{\partial y}\right|_{y=0} \tag{2}$$

Hence, a high spatially resolved velocity field near the wall is necessary to calculate accurate wall shear stress. Note μ represents the dynamic viscosity of the fluid.

The impact of wall shear stress on aneurysm growth and rupturing is significant as concluded by previous research [21-24]. Techniques for identifying and treating aneurysms have been available, however surgeons are hesitant about treating every unruptured aneurysm due to the risk involved. Currently, there is a morbidity and mortality rate of 2.6% and 1.3%, respectively, with regards to surgical procedure of coil treatment [27]. Previous studies have observed aneurysms of size 7mm or less are at minimal risk of rupture, while those larger have merit for treatment [24]. When intracranial aneurysms rupture, or subarachnoid hemorrhage (SAH) occurs, the rates of morbidity and mortality are significantly higher [28]. Approximately 75% of SAH cases are caused by a saccular aneurysm rupture which typically occurs within the circle of Willis or branch artery [28]. If the patient does survive SAH, about half of the survivors undergo drastic life changes with needing daily assistance through the rest of their life. The occurrence of an unruptured aneurysm in someone over the age of 30 is prevalent in 3.6-6.0% of the

population. Females have a higher risk than men and those who smoke have a higher probability than those who do not [28].

2.3. Previous/current blood flow velocity techniques

Over the years, there have been multiple techniques used to determine the velocity field of the blood flow. Techniques include 4D flow MRI, laser doppler velocimetry, and DSA. In 4D flow MRI, or sometimes referred to as 3D time-resolved phase-contrast MRI, the ability to obtain 3D flow measurements is possible which has helped with calculating wall shear stress, pressure differences, and kinetic energy. The accuracy of wall shear stress is dependent on the spatial and temporal resolution of the 4D flow MRI, where the steep velocity change near the wall relies on interpolation of the velocity between neighboring voxels [24]. The accuracy of wall shear stress is difficult to quantify seeing that a standard for measuring wall shear stress in vivo has not been established [29]. Results from Szajer's research exploited the pitfalls of using 4D flow MRI to determine 3D flow features. For instance, the measurement errors are more significant in complex flow patterns containing slower flow regions. Another conclusion was MRI has poor accuracy when the boundary layers become thinner in higher velocity regions because of spatial resolution. This conclusion was confirmed by Cibis et al. who investigated the effects of reducing spatial resolution in CFD models and observed a decrease in wall shear stress, hence the spatial resolution has significant impact on the wall shear stress [30]. Some of the error associated with MRI may be a result of the velocity sensitivity encoding parameter. This parameter is set to cut off velocities larger than itself, but increasing this value tends to increase the amount of noise [24]. Another method uses laser doppler velocimetry to obtain instantaneous and continuous measurements in tissue microcirculation. This method has been able to obtain blood flow measurements in disrupted and basal flow [31]. However, the accuracy of this

method relies heavily on the linearity of the flow meter output in red blood cell flux [32]. Signal processing, such as electronic linearization, has aided the flow meter output, but this technique must be used carefully when the percentage of red blood cells in circulating blood is above 0.2% since the response of the power spectral density algorithm becomes poor above this point [32]. Additionally, laser doppler flowmetry should only be used to quantify relative changes in blood flow because of the skin's microvasculature variability and complexity across the body which results in complex light-scattering in tissue [32]. With DSA, there are multiple advantages as well as disadvantages. Advantages include digital post-processing, the capability to capture images at a high frame rate, low-contrast performance, and digital image subtraction [33]. Pitfalls of DSA are high sensitivity to patient movement, geometric distortion, and small round field of view [33]. In a comparative study between magnetic resonance angiography (MRA) and DSA on young adults, DSA was able to recognize lesions in cortical areas because MRA has a lower spatial resolution than DSA [34]. From the research of Cibis, it is clear that in choosing a method for evaluating wall shear stress the method must recover high spatial resolution, hence DSA would be preferred over MRA.

2.4. Previous/current CFD regarding blood flow

From the early 2000's, researchers have been applying CFD to medical applications ranging from general blood flow studies to investigating wall shear stress on intracranial aneurysms. The use of CFD in these applications has gained insightful information about hemodynamics and has inspired new techniques for evaluating blood flow. Though there are still challenges with simulating blood flow with regard to non-Newtonian fluid as well as elastic wall boundary conditions. In 2004, Byun and Rhee studied the effects of inserting coil embolization in saccular aneurysms to determine flow characteristics when the coil does not completely fill the aneurysm

[35]. These simulations considered the vessel walls as rigid since the cerebral arteries are less elastic than other arteries and to compensate for the non-Newtonian viscosity the model from Carreau was adopted [35]. The Carreau model is a four-parameter model which is valid for a broad range of shear rates, unlike the power law model which suffers in accuracy when the shear rates are very high or very low [36]. Yi et al. have investigated Newtonian flow through an internal carotid artery sidewall aneurysm by conducting PIV testing to validate an in-silico model [37]. Additional research from Yi et al. have validated in-silico cerebral aneurysm models using non-Newtonian blood analogues which compared hemodynamic characteristics such as wall shear stress (WSS) and oscillatory shear index (OSI) [38]. Comparisons between the use of Newtonian and non-Newtonian fluids in the simulation were made and concluded the Newtonian model generally underestimates WSS and OSI in most regions of the aneurysmal sac. Szajer and Ho-Shon compared multiple flow features between 4D flow MRI and CFD methods for intracranial aneurysms. The best considered method for reference standard on wall shear stress *in vivo* is CFD, since it is the most studied for wall shear stress [24]. However, Szajer did hypothesize CFD may overestimate the wall shear stress since the boundary conditions focus on using a rigid wall whereas *in vivo* the walls are elastic which reduce the wall shear stress. Therefore, other researchers have investigated the effects of fluid solid interaction which allows them to model arterial walls as an isotropic hyperelastic material [39]. The objective was to determine a correlation between flow induced wall shear stress and geometry of the artery by computing the artery wall shear stress within a finite element analysis (FEA) software. Results from the FEA simulation and the rigid wall CFD model showed the wall shear stress distribution was significantly affected by the wall boundary condition, especially the minimum and maximum extrema [39]. CFD can provide detailed flow information, however, it is time

consuming, sensitive to boundary conditions as well as patient specific conditions, vastly dependent on CFD abilities, which impede the wide adoption of this technique in clinical use. Therefore, obtaining flow information directly from the imaging process is an optimum pathway for clinical use. Dye visualization velocimetry is an analogy of the blood flow angiography. To study the feasibility of velocity field quantification based on angiographic images, we need to know the velocity field for validation. CFD simulation can provide known flow field with dye injection, and then the simulated projection images serve as the analogy of X-ray imaging. Dye diffusion in CFD has been studied by Javadi et al. through Marangoni instabilities during drop exchange [40]. They compared their CFD results with an experiment they performed to ensure accuracy within the CFD boundary conditions. In the experiment they used brilliant green dye which was estimated to have a diffusion coefficient of $5\times 10^{-10}\ m^2/s$. Other research has incorporated dye into their simulation, but as passive advection as opposed to active advection. Passive advection uses prescribed velocity flow field to guide the dye which results in a linear problem. Active advection incorporates a non-linear problem which is more complex but leads to more accurate dye diffusion in experiments. Karch et al. studied the distribution of dye in unsteady flows, where they implemented their own weighted essentially non-oscillatory (WENO) reconstructed scheme [41]. In this study, the significance of CFD meshing was noted due to the overly sensitive numerical diffusion with respect to mesh grid sizing. Neglecting the care needed for the mesh size results in deviations in the true physical behavior.

3. Motivation

There has been numerous research regarding aneurysm model simulations with CFD and has provided full detailed information including the velocity distribution and wall shear stress. However, the use of CFD for every patient specific aneurysm is not feasible with regards to time, cost, and accuracy. Generating an aneurysm model for CFD requires high resolution imaging such as 3D rotational angiography, which requires time and money. The 3D images then require filtering, such as sharpening and/or vessel enhancement, and smoothing to create a volumetric model [42]. Creating a viable mesh and boundary conditions for the model involves time and highly trained individuals in CFD to produce accurate simulations. With regards to accuracy, CFD must fully represent the application which entails elastic wall boundary conditions and non-Newtonian fluid conditions. Therefore, a process involving less time and overall cost efficiency as well as a method for estimating velocity flow features based on medical images is needed. Numerous studies have applied OFM, cross-correlation, or other algorithms to projection-based images to obtain velocity profiles [3,5,8,9,15]. However, the accuracy of the velocity estimation is hindered by the acquisition of images. Projection images are a result of some type of ray energy transmitting through a 3D volumetric flow field which is then compressed onto a 2D image. Without isolating a 2D plane within the flow, as a laser sheet from PIV would do, the velocity becomes an average representation and therefore leads to inaccuracy. These conclusions have been depicted by Yang and Johnson [15], where they investigated velocimetry of dye visualization in a horizontal, pulsatile tube flow. Velocity distributions from the dye visualization

were compared with PIV results located at the center-plane of the tube, which ensued a 20% underestimation from the dye visualization at the center of the tube and a 25-60% underestimation near the wall [15]. Again, this dissimilitude is a result of the fundamental problem in compressing the 3D volumetric flow onto a 2D projection image. Therefore, a method to correct the raw DVV measurements is required to improve the velocity flow measurements. Parameters dependent on velocity would therefore be more accurate through the improvement of velocity measurements. For instance, wall shear stress is dependent on the velocity gradient near the wall and turbulent kinetic energy is dependent on the variances of velocity components. This method incorporates machine learning which reads in raw DVV measurements to approximate new velocities. The program will detect patterns in the projective dye images during the learning process and correct the velocity field obtained from DVV. Since experimental images incorporate uncertainty, for instance light refraction and blemishes on the test section surface, projective dye images can be generated from CFD simulations to avoid these uncertainties. Additionally, using CFD provides the exact known flow field which allows supervised machine learning. Prior to generating the projective images from CFD, experimental measurements are required to validate the CFD simulation. Therefore, PIV is needed to validate the CFD velocity and dye visualization is required for comparisons with the CFD generated projective images. To provide good comparisons with the CFD simulation by mitigating the uncertainty in experimental results, a vertical squared tube was selected as opposed to an aneurysm model. With regards to PIV measurements, the squared tube allows easier confirmation of the laser position whereas the laser position through the center of the aneurysm proves more difficult. Another benefit of the squared tube over the aneurysm is the flat perpendicular surface to the light rays which mitigate light refraction. With the aneurysm model,

the curved surfaces enhance light refraction and during the manufacturing process noticeable surface blemishes are present.

For the medical field, this research would provide a translational method for determining more accurate velocity fields which in turn would allow more accurate wall shear stress calculations on blood vessels and aneurysms. In providing details regarding the wall shear stress, medical professionals could develop criteria to justify operating or not operating on vascular diseases such as unruptured aneurysms.

4. Experimental Analysis

4.1. Angiographic Analogy

In acquiring angiographic images, an x-ray beam, which is directed toward the region of interest, transmits through the patient, and generates a projected image on the scintillator plane. Contrast within the image is a result of x-ray attenuation through soft tissue, muscle, bone, and iodine-contrast agent where the k-edge value among these items varies. Among the items listed, the contrast agent has the highest value by far. Therefore, images are taken prior to injecting the contrast agent into the patient to create a reference image or masking image. This masking image is later used to subtract from the images containing iodine-contrast, therefore resulting in an image containing only the distribution of the contrast agent. This type of image can be replicated in-vitro without the use of an x-ray by considering a light source as the x-ray source and injecting typical dye into water as opposed to injecting iodine-contrast agent into a blood vessel. The light rays pass through water and the dye with the attenuation occurring only through the dye. Thus, the projected image consists of the accumulation of dye concentrations through the entire 3D domain. Using this setup an angiographic analogy can be made where the x-rays are replaced by light rays, soft tissue and bone is replaced with water (since DSA omits the soft tissue and bone), and iodine-contrast is replaced with dye. This provides a cost-effective method for studying projective image velocimetry without using harmful x-rays.

4.2. Flow diagnostic techniques

4.2.1. Particle Image Velocimetry

Particle Image Velocimetry (PIV) is a technique in which a flow field is filled with marked particles that are captured through successive imaging. PIV includes a thin laser sheet that illuminates the seeding particles within a specific plane while simultaneously recording the image. Additionally, a second pulse is initiated, after the first pulse has disappeared, to capture the succeeding time frame of the image. These images are then used for further analysis to establish an instantaneous velocity field that encompasses the planar section of the observed flow [43]. PIV can provide a large spatial resolution with thanks to the advancement of high-resolution cameras, but the time domain is fairly limited due to the laser technology [44]. This technique is of growing interest as it is non-intrusive, so for boundary layers near a wall, PIV is highly applicable [44]. Other advantages include the capability of measuring and visualizing complicated unsteady flow fields [45]. These images can be compared through a technique called cross-correlation, which was derived by Adrian in 1988, where the light intensity at two points of time along with a separation vector contributes to the cross-correlation [46]. This development leads to the decomposition of the cross-correlation estimator into three components: Convolution of the mean intensities, noise fluctuation, and the correlating displacement [46]. These three components are byproducts of the cross-correlation process in which the images are divided into equal sized windows for further comparisons. Each window, within the first image, is evaluated inside a search region of the second image. The search region is larger than image one's window in order for the window to move around within the search region therefore providing multiple correlation values. For instance, one can consider a window of 3x3 pixels that is contained by a 5x5 search region. The window would be initially placed in the center of the search region where

the intensity values are compared. Once a correlation is derived for that set, the window would be moved by one pixel in a step and evaluated again until all possibilities have been compared within the search region. Figure 6 gives a more visual representation of this process.

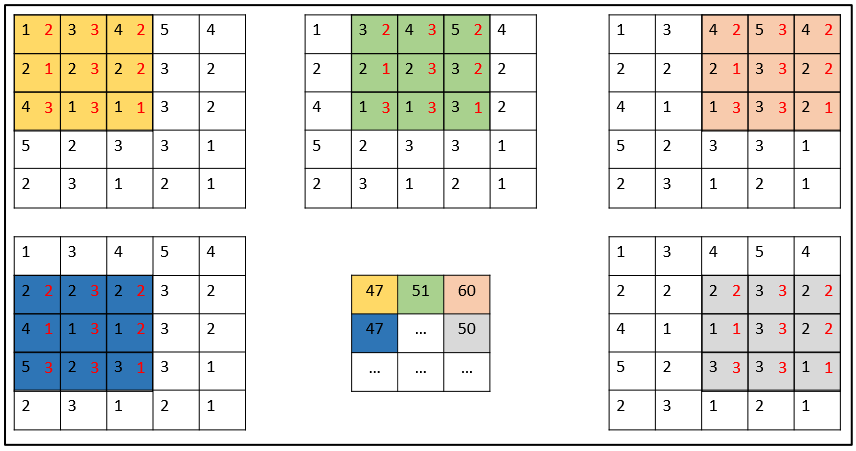

Figure 6: Numerical demonstration of the cross-correlation plane process

After all of the possibilities are evaluated, the region with the highest correlation coefficient is used as the indicator for how far the particles, for that window, traveled between the succeeding images. This process continues until each window from the initial image has an associated region from the second image. Notice that these displacement vectors are of linear form only, therefore these vectors are strictly limited to first order [44]. Cross-correlation is the basis for multiple methods such as the direct correlation method, Hart correlation, and the Fast Fourier Transform (FFT). Direct correlation evaluates the intensity at each pixel within the search region with respect to the window from the first image. However, high correlation values were observed with high density regions of particles. Thus, a normalizing scheme was placed to associate the equivalent number of particles with the correct displacement in order to avoid regions with large average intensities. Other methods, like the Hart method take on a different approach. The Hart method uses a technique which avoids the dependency associated with the image characteristics

as well as the need to correlate small data sets by implementing an algorithm for recursive correlation [47]. Principle behind the recursive correlation is to approximate the displacement for a large region that acts as a constraint for correlating the smaller regions within the large region [47]. Up to this point the methods mentioned involve the use of correlating intensity levels based on space which requires a large amount of calculations. For a given square window of size L, the number of calculations required is L^4 [48]. Therefore, a new method was created in order to perform these tasks at a faster rate, hence FFT. The method converts the intensity in space into a frequency domain. Thus, by using the complex conjugate multiplication, the correlation between successive images can be determined [44]. One item of concern for these methods, however, is that the displacement is only as accurate as the size of the pixel since the displacement is calculated for an integer value. Analyzing the displacement for a fraction of a pixel is called sub-pixel interpolation. Two methods are of popularity: Center of gravity and Gaussian fit. Center of gravity utilizes the points that correspond to the correlation peak, for which the position of each point is multiplied by the respective intensity and then added together. The summation is then normalized through division of the accumulated intensities. For regions with higher number of identified points, the more accurate the center of gravity method becomes. This particular method does not assume a local maximum point, but an alternative form uses only three identified points with the local maximum peak included [49]. Other methods, such as the Gaussian fit, utilize the fact that the peak is a function with a central maximum and incorporate the Gaussian function to determine the fractional displacement. Recently, a hybrid method was developed by Yang in which the advantages of cross-correlation and OFM were combined to provide higher spatial resolution compared to typical cross-correlation and allowed larger displacements to occur that OFM by itself would not be able to handle [50]. Results of this work

showed consistent improvement over various PIV processing algorithms such as FFT, Hart, and direct correlation.

Over the years technology has advanced rapidly and with these new advancements there have been significant improvements upon existing techniques. For instance, experimental equipment for PIV testing, including the use of laser and camera technology, have improved. Growth in laser technology has allowed for the development of new lasers that feature higher frequencies and consistent power output between pulses. These two advancements alone are crucial to the accuracy of PIV results. For PIV algorithms, the intensity is crucial in calculating displacement. If the power output from the first laser pulse to the second pulse differs, then the intensity of the particles from the first image to the second image are not constant. Therefore, a higher level of error is introduced into the calculation of the displacement. Also, with these new laser innovations the intensity difference between images can be minimized and consequently the error. Furthermore, by developing higher frequencies the time in between laser pulses can be minimized, thus causing a smaller time step amongst images. Decreasing the time between images allows for less displacement of the particles. Eliminating large particle movement permits for particle patterns to remain intact. These patterns allow for the PIV algorithms to calculate displacement values. To involve large particle displacements within two images is essentially introducing large portions of error in the results. Improvements in laser technology are inadequate if the camera being used is unable to operate at the same level as the laser. Hence the need for progress in camera technology was equivalently important. In order to capture the laser pulses with higher frequencies, the camera's frame rate had to be improved. Current cameras can reach a quarter of a million frames per second. To put in perspective, the normal motion picture is played back in twenty-four frames per second. Another progressive camera

feature is the resolution. Increasing the resolution of a picture allows for more defined images and in effect more accurate results. Recall that the cross-correlation method is a statistical approach. By introducing more pixel values the amount of "sample" correlation values also increases. Therefore, when a displacement value is calculated, the size of the pixel is smaller and therefore more concise as opposed to images with lower resolution. Some cameras are able to record images with a resolution of 5.5 million pixels, like the LaVision Imager sCMOS. Each of these new developments have contributed greatly to acquiring commendable PIV images, which in turn establishes the foundation to provide accurate results after being applied to the PIV algorithms.

4.2.2. Optical Flow Method

In 1981, Horn and Schunck first proposed a brightness constraint in order to determine the flow's motion while a variational formulation was used to develop a velocity field, or optical flow, which alters one image into the next through a time sequence [51; 52]. Use of the brightness constraint assumes that the intensities of the particles are constant from one image to the next. However, this assumption does not hold any physical truth due to the fact that the derivation of the equation does not come from any physical principle [52]. Thus, Liu and Shen (2008), developed experiments for classic flow fields that incorporated shadowgraph and transmittance imaging in density-varying flows, transmittance and scattering of particulate flows, transmittance through transported passive scalar, laser sheet-induced fluorescence, and schlieren for the purpose of deriving projected motion equations [53]. Results yielded a physical meaning that the Optical Flow is proportional to the path-averaged velocity of fluid or particles in flow visualizations [53]. Improving the accuracy of the optical flow method for PIV use was conducted extensively by Quènot et al. (1998) through the inclusion of Dynamic Programming

that divides PIV images into parallel strips that calculate the displacement in the direction of the strips [54]. B. Wang et al. (2014) also conducted mathematical analysis of the Optical Flow methods' fundamental equations including the physics-based Optical Flow equation and the Euler Lagrange equation. From the physics-based Optical Flow equation, they developed a theorem that confirms a unique solution of the minimization problem, thus verifying that the minimization preserves discontinuities in a fluid velocity field [53]. Other work includes the study of optical flow with regards to an optimal control problem, where divergence free criteria, for flow conservation, is applied that leads to a proof for the optimal conditions for the optical flow [55]. Furthermore, the Optical Flow equation shares a common form with the transport equation [56]. Most studies involving the improvement of the optical flow method incorporate a parameter for regularizing space as a consequence of the flow's smoothness for a small region, but it has been proven that this approach effects the magnitude of divergence and vorticity field in a negative manner [57]. Liu et al. (2015) compared the optical flow's performance with recognized cross-correlation methods for synthetic images containing Oseen vortex pair within a uniform flow. Results yielded larger error for the correlation methods than the optical flow near the center of the vortex, where the velocity gradient is largest. This indicates that the optical flow can capture sharp changes in the flow, which is of high importance for applications such as mesoscale dynamics with respect to clouds. Mesoscale dynamics are characterized by systems with a range of motion greater than 10 km, therefore satellite imagery is particularly useful when coupled with computer vision programs in order to calculate cloud velocity. However, the techniques were not admirably adapted to the spatial displacement, thus a method incorporating a correlation method and the optical flow method were used to calculate the cloud flow more accurately [58]. Steps were taken further by utilizing the optical flow method with early storm

warning systems such as the Short-range Warning Intense Rainstorms in Localized System (SWIRL) for Hong Kong [59]. Researchers have also been particularly interested with the dynamics of the sun's outer layers as they have been very influential over extreme phenomenon in the solar system. Exploiting the optical flow method for use in understanding the sun's dynamics provided insight to a relationship with the local magnetic field [60]. Theory involved with this method has been studied extensively as well as validated, which has created multiple opportunities for applications, including PIV, to become more resourceful.

Deriving the Optical Flow method was credited by Horn and Schunck in 1981. The premise behind the Optical Flow method was initially based off of assumptions and constraints that were not related to any physical meaning. Not until the work of Liu and Shen, did the Optical Flow method contain physics-based concepts. Both methods entail the same procedure, in which velocity components are calculated for further error analysis and once the error has become minimal the velocity components are selected.

4.2.2.1. Horn-Schunck Method

Basis of the Optical Flow method follows the work of Horn and Schunck [51], which incorporates a constraint regarding the rate of change of the image brightness must be held constant. However, the image brightness alone cannot detect the flow's movement, thus a supplementary constraint based upon the smoothness of the flow is introduced. Horn and Schunck's method is based off of the principle of minimizing the amount of error associated with the brightness constraint and the displacement in smoothness within the velocity flow, by optimizing the velocity parameters that create the Optical Flow field. Due to the instability in the brightness constraint introduced by noise and quantization error, a weighting factor, α, is provided for the smoothness constraint. Therefore, applying more emphasis on the minimization

of the smoothness constraint. The essential factor in minimizing the total error lies within the optimization of the Optical Flow velocity (u, v). Therefore, in order to determine these values, the calculus of variation is applied to the total error, which leads to two equations for two unknowns.

$$Q_{x_1}^2 u + Q_{x_1} Q_{x_2} v = \alpha^2 \nabla^2 u - Q_{x_1} Q_t \tag{3}$$

$$Q_{x_2}^2 v + Q_{x_1} Q_{x_2} u = \alpha^2 \nabla^2 v - Q_{x_2} Q_t \tag{4}$$

Here the pixel intensity is represented by Q, the x- and y-coordinates are denoted as x_1 and x_2, respectively, and the subscripts represent partial derivatives with respect to the subscript variable. Calculating the $\langle u, v \rangle$ components require an iterative process which calculates an error for each iteration until the error is below an optimal value. This process is explained in more detail within the paper of Horn and Schunck [51].

4.2.2.2. Physics based Optical flow

Horn and Schunck created the foundation of the Optical Flow method; however, their method was not based on any physical approach. Liu and Shen [52] developed the Optical Flow method based on a physical meaning and was represented as the following.

$$\frac{\partial Q}{\partial t} + \nabla \cdot (Q\boldsymbol{V}) = f(x_1, x_2, Q) \tag{5}$$

Where Q is the intensity and $\boldsymbol{V}$ represents the velocity components (u, v). Using the simplicity of the Horn-Schunck smoothness constraint and the variation formula, an expression is derived.

$$J(u) = \int_A \left[\frac{\partial Q}{\partial t} + \nabla \cdot (Q\boldsymbol{V}) - f\right]^2 dx_1 dx_2 + \alpha \int_A (|\nabla u|^2 + |\nabla v|^2) dx_1 dx_2 \tag{6}$$

Where α represents the Lagrange multiplier which is used to emphasize the smoothness constraint over the brightness constraint. Through the use of the Variation of Calculus, four different expressions are derived, which combine to form the Euler-Lagrange equation displayed below.

$$Q\nabla \cdot \left(\frac{\partial Q}{\partial t} + \nabla \cdot (Q\boldsymbol{V}) - f\right) - \alpha\nabla^2\boldsymbol{V} = 0 \tag{7}$$

In order to evaluate whether or not the velocity components are accurate, the error due to the intensity (ΔQ) and the error in velocity ($\Delta\boldsymbol{V}$) have to be included. Thus, when the errors associated with the intensity and velocity are included into equation (7), we derive an equation for ($\Delta u, \Delta v$).

$$Q\nabla[H_I + \nabla Q \cdot (\Delta\boldsymbol{V})] + \alpha\nabla^2(\Delta\boldsymbol{V}) = \alpha\left(\frac{\Delta Q}{Q}\right)\nabla^2\boldsymbol{V} \tag{8}$$

Where,

$$H_I = \Delta\left(\frac{\partial Q}{\partial t}\right) + \Delta(\nabla Q) \cdot \boldsymbol{V} + Q\Delta(\nabla \cdot \boldsymbol{V}) + \Delta Q(\nabla \cdot \boldsymbol{V}) \tag{9}$$

From Equation (8) the error associated with the approximated values for $\langle u, v\rangle$ can be found. More importantly, Equations (8) and (9) demonstrate how the intensity error is the leading cause for calculating inaccurate velocity components. The velocity components are found through multiple iterations, where each iteration incorporates an error between then new $\langle u, v\rangle$ values and the previous values. If the error is too large, then the next set of $\langle u, v\rangle$ values are calculated through the use of the Euler-Lagrange equation. New approximations are calculated through the discrete scheme described by Liu and Shen, more specifically the Jacobi blockwise iteration method

4.2.2.3. OFM Validation

Optical flow method was developed under the constraint of smoothness, as stated earlier, and to establish smoothness a Gaussian filter is applied. Parameters for the Gaussian filter, however, were never correlated to the accuracy of the Optical flow. Thus, it was imperative to conduct a study between the Gaussian filter parameters and the error associated with these said parameters for use in the Optical flow method. This study incorporated a single PIV image which was later used to generate a successive PIV image. Yang et al. (2016) developed a program to create a second image that resembled a uniform flow through which a pair of vortices were generated by manipulating the PIV image. Then, both images went through a Gaussian filter of equal parameter values. To identify the difference between various parameters for the Gaussian filter, a characterized intensity gradient, γ, was derived.

$$\gamma = \sum_{i=1}^{n_x} \sum_{j=1}^{n_y} \left(Q_x^2 + Q_y^2\right)^{\frac{1}{2}} \tag{10}$$

The intensity gradients in the x- and y- directions are presented as Q_x and Q_y, respectively, and the number of pixels in the x- and y- direction are represented by n_x and n_y, respectively. Central differencing scheme was used in the calculation of the intensity gradients. For the reason that the second image was generated, the exact solution was known and therefore used in analyzing the error associated with optical flow corresponding to the characterized intensity gradient. Figure 7 displays the generated images that correspond to the characterized intensity gradients: (a) γ=2.9; (b) γ=6.1; (c) γ=13.4; (d) γ=17.2.

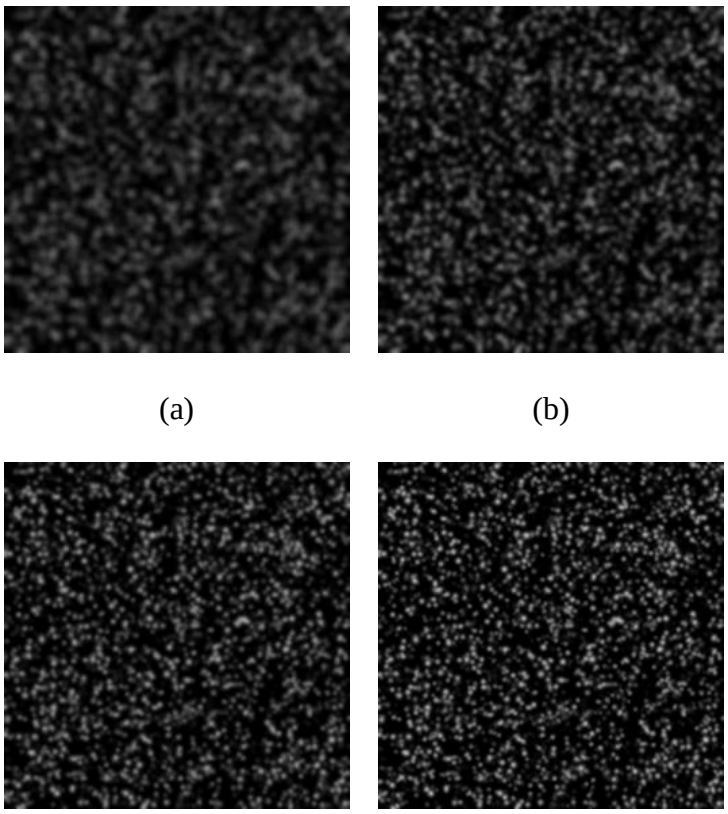

(a) (b)

(c) (d)

Figure 7: Generated images with various characterized intensity gradients.

In Table 1 the Gaussian parameters (mask size and standard deviation) are shown with the corresponding characterized intensity gradient as well as the error associated with each velocity component.

Table 1: Average error corresponding to characterized intensity gradient.

Intensity Gradient, γ	s_1	σ_1	s_2	σ_2	$Error_u$	$Error_v$
2.9	12	4.8	5	2.0	2.90	2.40
6.1	8	3.2	3	1.2	0.87	0.73
9.3	5	2.0	3	1.2	0.48	0.40

13.4	3	1.2	3	1.2	0.43	0.33
17.2	3	1.2	N/A	N/A	0.51	0.37

Results of this analysis gives insight into two conclusions. One, for images that incorporate small intensity gradients the amount of error tends to increase. Two, when a Gaussian filter is applied to generate an intensity gradient of 13.4 the error is minimized. Therefore, when analyzing with optical flow, cases that incorporate an intensity gradient of 13.4, with the help of the Gaussian filter, are highly desirable.

The study above concentrated on the accuracy of OFM when parameters for the Gaussian filter were varied for a typical PIV image, however the accuracy associated with typical dye visualization is needed. To quantify the accuracy of OFM for dye visualization, an image was created with regions of high intensity gradients and a second image was generated with a uniform displacement. The displacement was varied from 0.1 pixels up to 2.0 pixels to determine optimal displacement conditions. Below is the original image along with the error associated with each displacement.

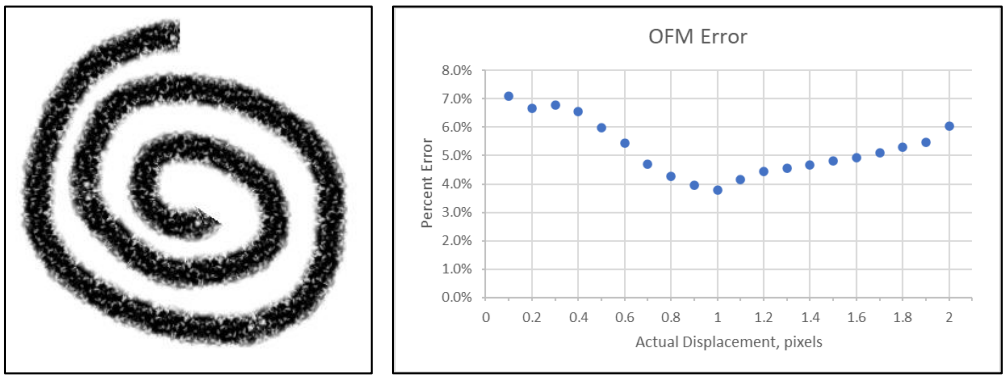

Figure 8: Original test image used to generate a displaced image (left) and the OFM error associated with various pixel displacements (right).

From the error plot in Figure 8, the OFM accuracy suffers when the displacement is less than 0.5 pixel with maximum error of 7.1% at 0.1 pixels. Between 0.7- and 1.6-pixel displacement the error is below 5% with the lowest error occurring when the displacement is 1.0 pixel which corresponds to a 3.8% error. The plot also exhibits an increasing trend in error when increasing the pixel displacement past 1.2 pixels. Therefore, optimal conditions for OFM occur when the displacement is between 0.7- and 1.6-pixels.

4.3. Dye Contrast Comparison

To provide optimal conditions for OFM, a set of dye concentrations were tested to see which mixture provided the best intensity gradient. Three dye mixtures were created with various amounts of dye droplets into 200mL of water. Dye1 used one droplet of dye, Dye2 used two droplets of dye, and Dye3 used three droplets of dye. These mixtures were injected into an average flow rate of 0.0052 m/s which equates to a Reynolds number $Re = 148$. The syringe pump used to inject the dye was set at a constant rate of 9.99 mL/min and the camera was set to a frame rate of 3200 frames-per-second (fps). Additional settings were used for the camera to reduce noise caused by blemishes on the acrylic square-tubing by adjusting the gain to +1.0, gamma to +1.0, and brightness to -0.65. A further adjustment was including a convex lens in between the LED light and test section since this would create parallel light rays and consequently create a more uniform intensity distribution prior to transmitting through the test section. The images below provide a comparison between the three dye mixtures with respect to the contrast gradients present in the image. Dye1 and Dye2 provide some contrast gradients near the inlet, whereas Dye3 has an opaquer representation.

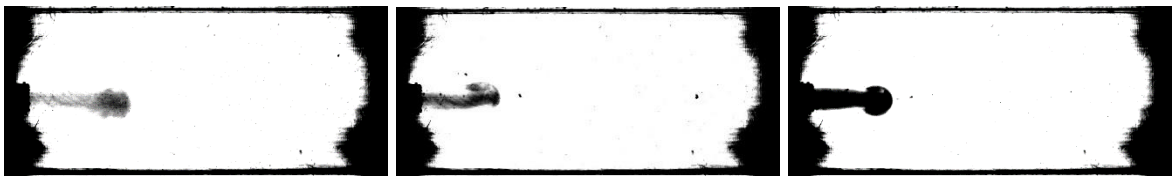

Figure 9: Dye mixture comparison between Dye1 (left), Dye2 (center), and Dye3 (right).

OFM was applied to multiple image sets through time for each of the dye mixtures to provide a general velocity flow field. If two or more image sets calculated a vector at the same coordinate, then those velocity vectors were averaged with one another. Dye1 was analyzed first by extracting velocity along y = 135 pixels. The absolute velocity plot shows a maximum velocity of 0.008 m/s near the "head" of the dye. Having a maximum value of 0.008 m/s is reasonable since the average velocity of the measured flow rate was 0.005 m/s. The average velocity would include the slow region near the wall, approximately zero, and the high-speed region in the center which would be larger than 0.005 m/s. Since the dye is located in the center, which is the high-speed region, a velocity of 0.008 m/s is within reason.

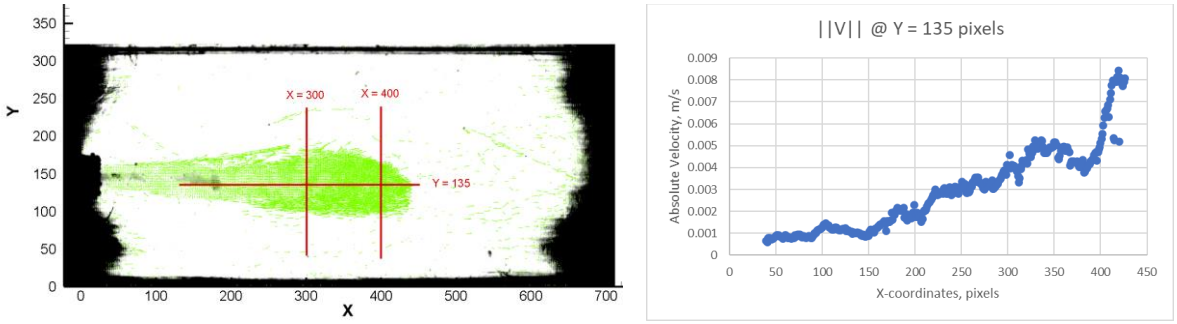

Figure 10: Averaged velocity vector field from multiple image sets of the Dye1 mixture (left); Absolute velocity distribution along Y = 135 pixels for Dye1 flow field.

Dye2 was evaluated in an equivalent manner where an absolute velocity profile was extracted along y = 135 pixels. Maximum velocity was around 0.008 m/s and the velocity distribution

displayed a similar pattern as Dye1, where the velocities located upstream have a relatively small velocity of 0.001 m/s then increases downstream as it reaches the head of the dye.

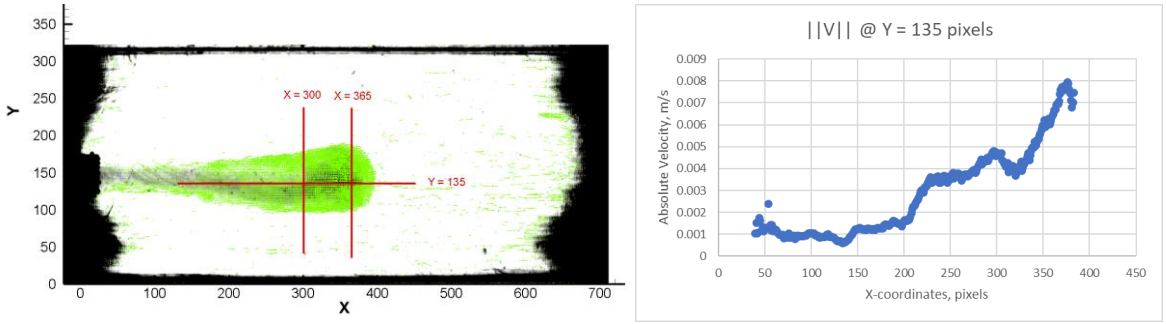

Figure 11: Averaged velocity vector field from multiple image sets of the Dye2 mixture (left); Absolute velocity distribution along Y = 135 pixels for Dye2 flow field.

Dye3 has a unique flow field distribution as it appears discontinuous in comparison to the previous dye patterns. This is due to the small intensity gradient within the dye trajectory, which results in zero velocity vectors in that region. The only vectors calculated occur at the head of the dye for each image set. Below are multiple images to show this phenomenon.

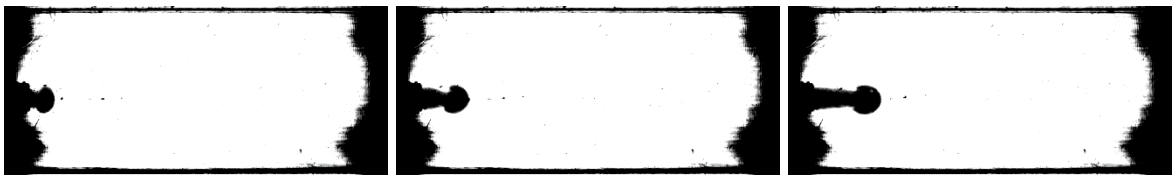

Figure 12: Various images throughout time of Dye3, where the intensity gradient within the dye trajectory is extremely low therefore very small velocities, if any, are calculated in that region.

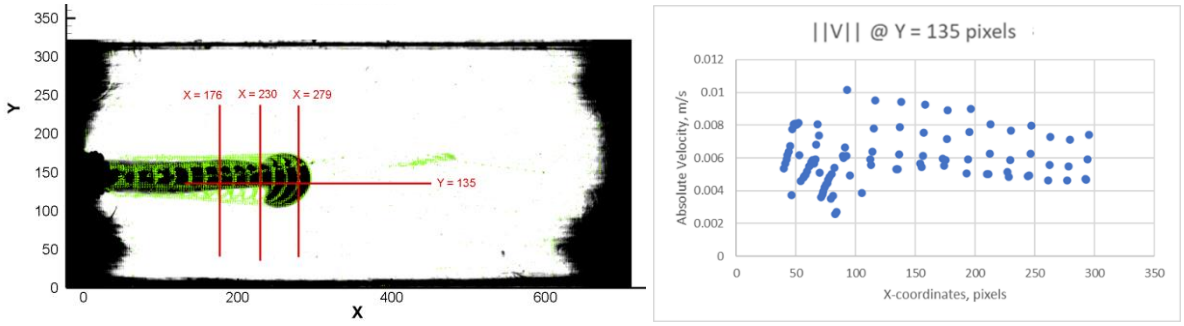

Figure 13: Averaged velocity vector field from multiple image sets of the Dye3 mixture (left); Absolute velocity distribution along Y = 135 pixels for Dye3 flow field.

Notice the absolute velocity distribution for Dye3 does not exhibit a similar trend as Dye1 and Dye2. The distribution is more uniform with mean velocity values between 0.006 m/s and 0.008 m/s. This type of distribution is ideal since it provides a way to calculate the overall flow field without averaging slower vectors caused from low intensity gradients as demonstrated in Dye1 and Dye2. Dye3 mitigates these slower velocities since the program specifically omits vectors which are calculated based on low intensity values. For instance, if pixel (10,5) from image A has an intensity $Q_A \leq 1$ and pixel (10,5) from image B has an intensity $Q_B \leq 1$ then the vector is omitted. From these results, Dye3 was selected for further testing with the vertical flow experiment.

4.4. Pulsatile water flow with dye injection through a horizontal tube

Study focused on comparative flow measurements using both the dye visualization technique based on transmittance light and PIV for a pulsatile tube flow. The pulsatile flow has the essential feature of blood flow being pumped from the heart. Visualization of the soluble dye injected into the water flow, taking advantage of the transmittance of visible light, served as the analogy of the X-ray angiographic imaging process. The results from the dye visualization measurements were compared with the PIV flow measurements in the middle plane of the tube at

different time instants for a pulsatile flow. The purpose of this study was to quantify the accuracy of velocity field estimation from the transmittance-based two-dimensional projection image of the three-dimensional volumetric flow field in comparison with the PIV measurements.

4.4.1. Dye Visualization

As shown in Figure 14, a physiological blood flow phantom has been built with a pulsatile pump (Harvard Apparatus pulsatile blood pump for large animals), two reservoirs, bifurcate connectors, and Tygon tubing. The pulsatile pump creates waveforms similar to cardiac flows. The nominal average flow rate of 20 ml/s, a pulse rate of 55 Hz, ratio of systole to diastole of 35/65 was adjusted to match human condition. A syringe pump (Harvard Apparatus 11 Plus) with a constant flow rate of 20 ml/min was used to inject the red dye into the flow. The fluorescent red dye (rhodamine WT, Cole-Parmer) was noncarcinogenic. A 0.8 mm (1/32 inch) diameter (inner) tube serving as the catheter was inserted just upstream of the test section to allow the injection of the red dye with an approximate concentration of 5000 ppm (parts per million). A spiral fixture ring was used to fix the position of the catheter in the cross section of the Tygon tube. The tube in the test section had an outer diameter of 12.7 mm (1/2 inch) and an inner diameter of 9.5 mm (3/8 inch). A clear mainstream flow was required to make the dye flow more distinct thus the flow could not be circulated. Instead, an open-circuit tubing flow was set up for the dye visualization experiment, thus two reservoirs were used in this experiment. The measurement was conducted under stable cyclic pulsatile flow conditions (constant pulse rate and steady volume flow waveform). Water bath was maintained at room temperature of 20 ± 0.5 °C.

A visualization system including a bulb light source with a light diffuser sheet and a complementary metal-oxide semiconductor (CMOS) high-speed camera (TSI, Powerview HS-

2000) were used to capture the transmittance-based visualization images continuously at a frame rate of 2000 frame/sec. By introducing the diffuser sheet in front of the light bulb, the intensity of light became more uniform and therefore mitigates intensity caused error when using optical flow algorithm to analyze the images. The camera was triggered by a pulsed signal from a laser tachometer (Monarch, PLT200) detecting the cyclic motion of the pump. Therefore, the starting time instant relative to the cyclic pulsatile flow was fixed for all experimental trials. The camera image plane size was set as 1024 × 256 pixel (87 × 22 mm) to fit the current tubing flow which allowed for over 4000 images to be collected at a time. By repeating the same process, 200 trials of the dye visualization experiments were carried out in order to obtain the averaged velocity field for each time step. Time-resolved velocity fields were estimated from the cinema sequence of 4000 images within two seconds for each trial by using the optical flow method. The mean velocity field was calculated by averaging the instantaneous velocity at each time step for 200 trials.

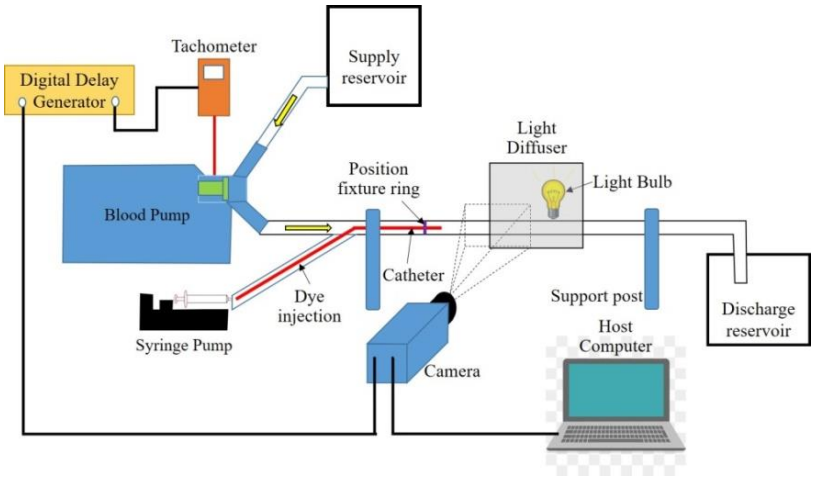

Figure 14: Dye visualization experiment features a supply reservoir containing clear water which is passed through a blood pump. Water flows through the horizontal tube where dye is injected via a syringe pump. Camera is activated when the tachometer sends a signal to the delay generator then signals the camera to start recording. Water and dye pass through the test section where light transmits through the mixture and projects an image for the camera.

4.4.2. PIV

All settings for the pulsatile flow condition were maintained the same as the dye visualization. Instead of dye being injected through the catheter, the syringe was filled with a mixture of water and fluorescent particles. Since PIV method required the illumination of particles, the flow downstream of the injection region was discharged back into the supply tank to conserve particles.

As shown in Figure 15, a digital PIV system was employed to make the flow measurement in the middle plane crossing the centerline of the tubing flow. The flow was seeded by fluorescent particles (fluorescent red polyethylene microspheres) with an averaged diameter of 10~45 μm and a density of 0.996 kg/m^3. A double-pulsed Nd: Yag laser (New Wave Gemini 120) was employed to provide two laser pulses of 120mJ at a wavelength of 532 nm. Laser sheets were produced by a set of spherical and cylindrical lenses. A mirror was used to redirect the laser sheet to illuminate the flow in the tube. The laser sheet thickness in the measurement region was about 0.5 mm. The fluorescent particle was excited by the laser and emitted fluorescent light at a wavelength of 610 nm. A 14-bit charge-coupled device (CCD) camera (PCO, Pixelfly QE) with a resolution of 1392 × 1040 pixel (66 × 49 mm) was used for the double-image acquisition with the axis of the camera perpendicular to the measurement plane. A long pass optic filter (transmission >600nm) was installed on the lens of the camera to filter out the laser illumination and reflection. This method can significantly reduce the effect of the light reflection from boundaries on the particle image. Since the maximum repetition rate of the laser is about 20 Hz, time-resolved measurements on the pulsatile flow cannot be obtained. Therefore, a phase-locked PIV technique was utilized to obtain phase-averaged flow measurements for the pulsatile flow. To accomplish this, a tachometer detected the cyclic motion of the pump, and two digital delay

generators were used to synchronize the whole PIV system with the cyclic flow. The pulse signal from the laser tachometer triggered the first digital delay generator (Stanford Research Systems, Model DG535), which added a given time delay controlling the phase, and then the first generator produced a pulse signal to trigger the second digital delay generator (Berkeley Nucleonics Corp, Model 575). The second digital delay generator controlled the entire PIV system and synchronized the double-pulsed laser with the CCD camera imaging processing. Through this technique, the particle image was taken at the same timing (phase) relative to the cyclic pulsatile flow for all successive images. The camera was connected to a workstation as well for image view and storage.

Insight 4G software (TSI Inc.) was used to obtain the instantaneous velocity vectors through a frame-to-frame cross-correlation methodology for particle image patterns in an interrogation window size of 32 × 32 pixel. An effective overlap of 50% was used for the cross-correlation processing. After the instantaneous velocity was determined, phase-averaged velocity was obtained by averaging the cinema sequence of 200 frames of the instantaneous velocity field at the same phase of the pulsatile flow. The uncertainty for the velocity vector measurements was estimated as 2% of the velocity magnitude.

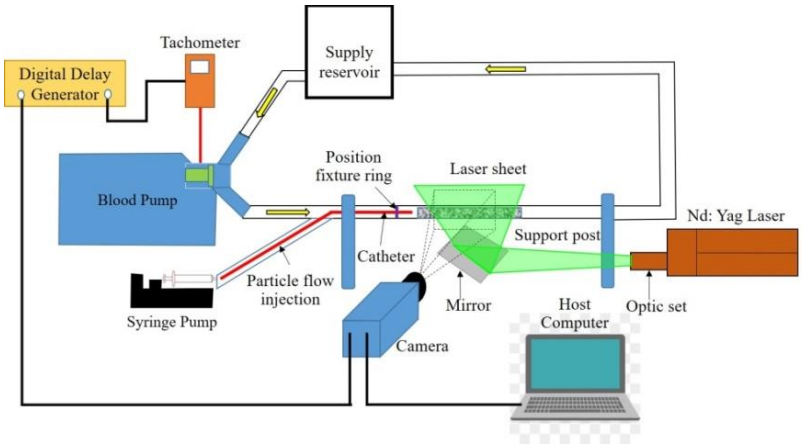

Figure 15: Experimental setup for PIV measurements used a closed system to retain particles in the flow. Laser sheet illuminated the test section in an orientation perpendicular to the camera view. Water and particle mixture was used within the syringe pump to maintain particle presence within the test section.

4.4.3. Results

Figure 16 shows the dye visualization image for optical flow analysis and the particle images for PIV analysis. For the dye visualization image (Figure 16 (a)), the distribution of the dye was observed in the middle region of the tube. Due to the turbulent effect and diffusion, the dye successfully diffused and filled into the whole cross section. Although the dye infusion was continuous with a constant flow rate, as the pressure inside the tube and the velocity of the flow suddenly increased due to the pulsatile feature, the dye did not flow out of the catheter for a short time interval. Therefore, a blank region without dye has been observed immediately downstream of the catheter for the current time instant t/T = 0.2, where t represents a time instant, and T represents the time period of the cyclic pulsatile flow. The similar pattern of dye distribution was also observed in the particle image from the PIV measurements as shown in Figure 16(b). It can be observed that the right end of the tube was slightly tilted up for better diffusion of the dye. This was not observed in the dye visualization image in Figure 16 (a) because the camera was

adjusted at an angle to make the tube horizontal in the image. The final PIV results were re-oriented as a horizontal tube to compare with the dye visualization results.

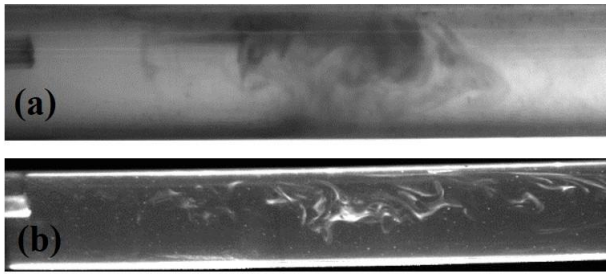

Figure 16: (a) Dye visualization image at t/T=0.2; (b) Particle image from PIV measurements at t/T=0.2.

For phase-locked PIV measurements, ten time instants from t/T = 0 ~ 0.9, with a step size of 0.1 were selected for the velocity measurements. Averaged volume flow rate calculated based on the averaged velocity has been plotted in Figure 17. For the dye visualization measurements, as the camera view size is limited, at some time instant such as t/T=0.3, the dye completely moved out of the camera window due to the sudden change in velocity and pressure, so this case cannot be used to estimate the velocity. For other time instants, the moving velocity was too low, thus the dye cannot diffuse effectively into the whole cross section. Therefore, only two time instants, as two blue dots indicate in Figure 17, were selected for the velocity distribution comparison.

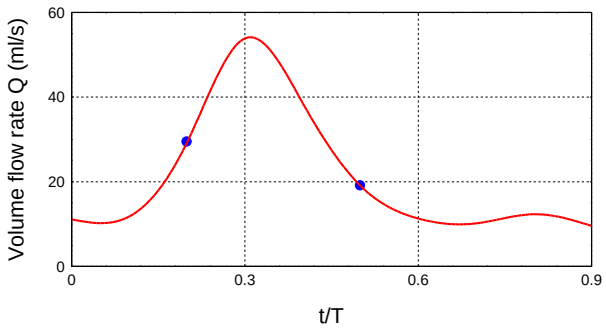

Figure 17: Volume flow rate waveform of the pulsatile flow.

Figure 18 (a) shows the instantaneous velocity field by using the OFM on the dye visualization image at t/T = 0.2. The velocity vectors were superimposed on top of the dye image, so the correlation between the dye distribution and the velocity distribution can be clearly seen. In the region of uniform dye distribution, for example in the region between X = 0 to X = 14 mm, the velocity vectors cannot be calculated correctly, i.e., the movement of the brightness pattern cannot be discerned. In the region between X = 16mm and X = 42mm, the brightness pattern is good for velocity estimation, but in the region after X = 44mm, very little dye can be observed thus poor velocity distribution was calculated. The velocity recovered from the OFM highly depends on the quality of the brightness distribution in the dye visualization image. Figure 18 (b) shows the velocity distribution with velocity magnitude contours. In general, the high-speed region is well-correlated with the good-quality brightness distribution, and this region is so-called "effective region". Figure 18 (c) presents the averaged velocity distribution at the same time instant from 200 trials of dye visualization measurements. Compared to the phase-averaged PIV measurement results as shown in Figure 18 (d), the velocity magnitude in the effective region from the dye visualization measurements is lower. A quantitative comparison of the velocity profiles at two locations indicated by the blue dashed lines is presented in Figure 19 (a) and (b). The averaged velocity profile together with two instantaneous velocity profiles from the OFM are compared with the averaged velocity profile from the PIV measurements at X = 34 mm, and X = 42 mm. For both locations, in the central region between Y = -3 mm and Y = +3 mm, the OFM results underestimated the velocity magnitude by 0.1 m/s approximately, which corresponds to about 20% of the velocity magnitude of the PIV measurements. Outside of the central region, as indicated by the black box region as shown in Figure 19, the OFM results underestimated the velocity magnitude by 25% to 60% of the PIV measurements.

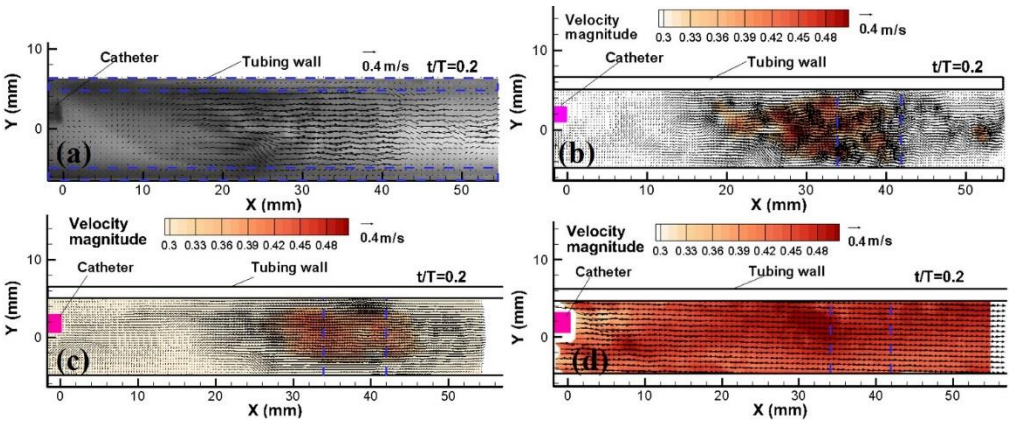

Figure 18: Velocity distribution results from OFM and PIV at t/T = 0.2 (a) Instantaneous velocity distribution superimposed on the dye visualization image from OFM; (b) Instantaneous velocity distribution with velocity magnitude contour from OFM; (c) Phase-averaged velocity distribution over 200 trials for the same time step from OFM; (d) Phase-averaged velocity distribution over 200 trials from PIV.

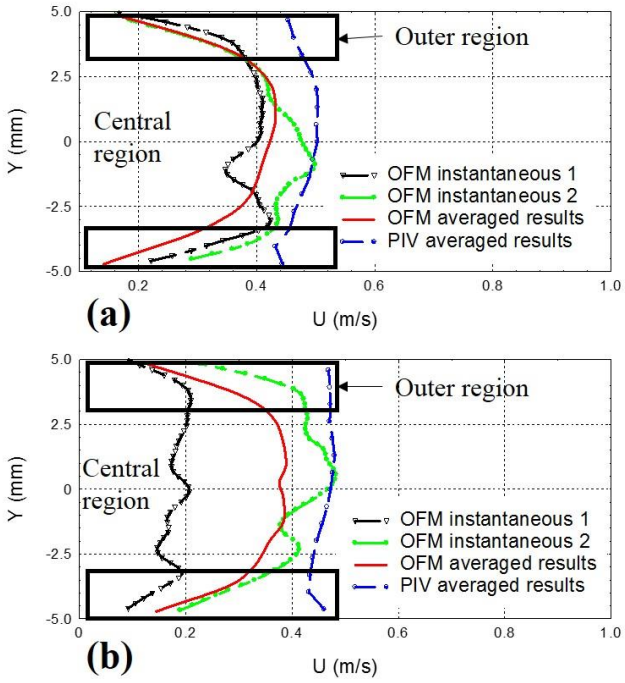

Figure 19: Velocity profiles comparison for OFM instantaneous velocity field, OFM averaged velocity field, and PIV averaged velocity field at (a) X = 34 mm, (b) X = 42 mm, for t/T = 0.2.

The reason for this large discrepancy is mainly attributed to the thick wall effect. This thick wall effect has been depicted and explained earlier in Figure 4. As shown in the shaded region, the

light has to pass through two relatively thick walls, two low-speed regions and a relatively high-speed region to generate the projection of the dye image. As the two low speed regions are adjacent to the high-speed region, the brightness pattern of the high-speed region is significantly affected by the dye distribution in the two-neighboring low-speed regions. Therefore, a consistent underestimation of the flow velocity was obtained in all cases. It should be noted the current experiment serves as an analogy of the X-ray angiography. For X-ray angiography, the thick wall effect from the blood vessel would be less significant since the penetrability of X-ray is substantially higher than the visible light.

Instantaneous velocity profiles for the two time instants were also compared with the PIV results. At both locations, the instantaneous velocity can match the PIV velocity profile at a certain region for some instances, while it can also produce a much lower velocity profile for other instances. The comparison implies a significantly unstable distribution of the dye within the tube. If the distribution of the dye is in a thin layer that is close to the middle plane which is also the PIV measurement plane, the velocity estimated from the dye visualization agrees with the PIV results. When the dye distribution is off the middle plane, the velocity estimation would be lower than the PIV results. By averaging all instances, the velocity estimation based on dye visualization is always lower than the PIV measurement results in the middle plane.

Figure 20 shows the velocity measurement results from both dye visualization and PIV at t/T = 0.5, which represents the end of systole flow, and the beginning of diastole flow. At this transition time instant, as shown in PIV results in Figure 20 (d), half of the tube flow above the centerline maintained a relative high velocity, while the half below the centerline slowed down. This phenomenon was also presented in the dye visualization image in Figure 20 (a) as sparse amounts of dye was diffused into the region below the centerline. As the pressure inside the flow

decreased according to the waveform, the dye flowing out of the catheter diffused well downstream of the catheter. As shown in Figure 20 (b), the high-speed region extends until the end of the current window. A very low-speed region below the centerline is mainly caused by the extremely low concentration of the dye. This feature is also shown in the averaged results in Figure 20 (c).

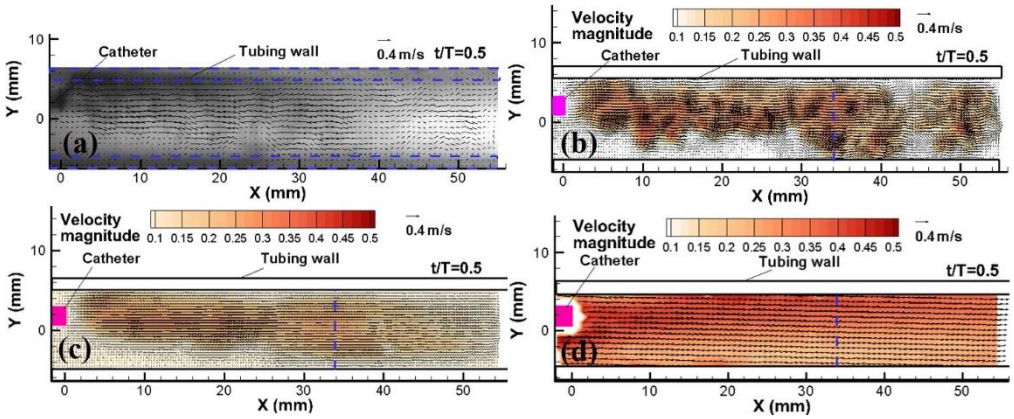

Figure 20: Velocity distribution results from OFM and PIV at t/T = 0.5 (a) Instantaneous velocity distribution superimposed on the dye visualization image from OFM; (b) Instantaneous velocity distribution with velocity magnitude contour from OFM; (c) Phase-averaged velocity distribution over 200 trials for the same time step from OFM; (d) Phase-averaged velocity distribution over 200 trials from PIV.

The quantitative comparison of the velocity profiles at x = 34 mm is presented in Figure 21. The dye visualization result does not capture the high-speed region above the centerline well. The averaged result from the dye visualization underestimates the velocity by 15% - 45% between y = 0 mm and y = 2.5 mm, and by 3% - 15% between y = -3 mm and y = 0 mm. In the region near to the wall as indicated by the black box, the OFM results underestimate the velocity magnitude by 35% to 80% of the PIV measurements for this case.

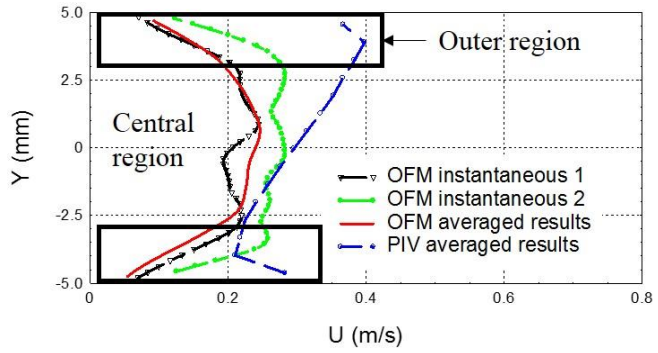

Figure 21: Velocity profiles comparison for OFM instantaneous velocity field, OFM averaged velocity field, and PIV averaged velocity field at X = 34 mm, for t/T = 0.5.

The averaged velocity magnitude was calculated for both the central region ($|y| \leq 3$ mm) and the outer region ($|y| > 3$ mm), and the total volume flow was also calculated, based on the velocity profile at X = 34 mm for t/T = 0.2 and 0.5 from both the dye visualization and PIV measurements. The results are summarized in Table 2. The estimated error in the averaged velocity magnitude for the central region is about 16% for the case of t/T = 0.2, and about 24% for the case of t/T = 0.5. In the outer region, the estimated error in the averaged velocity magnitude is about 29% for the case of t/T = 0.2 and 43% for the case of t/T = 0.5. The error in the total volume flow is approximately 15% and 29%, respectively.

Table 2: Comparison of the averaged velocity magnitude in the central and outer region, and the total volume flow rate $\dot{Q}$ at X = 34 mm for t/T = 0.2 and 0.5.

t/T	**Dye Central (m/s)**	**PIV Central (m/s)**	**Error**	**Dye Outer (m/s)**	**PIV Outer (m/s)**	**Error**	**Dye $\dot{Q}$ (ml/s)**	**PIV $\dot{Q}$ (ml/s)**	**Error**
0.2	0.41	0.49	16%	0.24	0.34	29%	25.3	29.9	15%
0.5	0.22	0.29	24%	0.13	0.23	43%	13.4	19.0	29%

Based on the comparison results between the dye visualization method and the PIV measurements, although there is some discrepancy, we can still see the potential of the visualization technique based on transmittance imaging for flow velocity quantification, which is particularly meaningful for many medical imaging applications. Inherently, transmittance-based imaging has its illness by projecting the three-dimensional volumetric distribution of the dye into a two-dimensional plane for OFM analysis. This compression effect from three-dimensional to two-dimensional field would result in a lower velocity estimation compared with the middle plane velocity distribution, which has been observed from the present experiment.

4.4.4. Conclusion

Although velocity field recovered from medical X-ray angiographic images and magnetic resonance images with optical flow method have been widely used for blood flow analysis and validation of CFD simulations on hemodynamics, there is still lack of solid validation of this technique for blood flow quantification. The inherent drawback of the transmittance-based image is that the three-dimensional volumetric flow field is projected onto a two-dimensional image plane. A dye visualization experiment in tubing flow was conducted as an analogy of the X-ray angiographic imaging process. The accuracy of the velocity field for a pulsatile tubing flow recovered from the dye visualization images based on transmittance light was estimated by comparing the results with the PIV measurements in the middle plane. It has been observed that the mean velocity in the central region was underestimated by approximately 16% - 24% on average. But outside the central region, the mean velocity could be underestimated by about 29% - 43%, which is mainly attributed to the thick wall effect. This effect would be less significant for X-ray angiography due to the excellent penetrability of X-ray. The improvement of the accuracy of the velocity recovery might be achieved by improving the diffusion and distribution

of the dye in the flow and applying appropriate correction model to correct the velocity magnitude.

4.5. Pulsatile water flow with dye injection through an aneurysm model

The error associated with dye visualization was quantified in a horizontal tube which resembles flow through a straight blood vessel, however the need for quantifying the error within a more complex geometry was needed. Thus, an experiment focused on pulsatile flow through a patient specific aneurysm was designed. The lab consisted of a Harvard Apparatus pump which replicated the flow pattern of a human heart. To represent a human heart, the pump incorporated settings such as systole to diastole phase ratio and pump rate measured in revolutions per minute (RPM). The systole to diastole phase ratio was set at 35% to 65%, respectively. The pump pushed water through the system with a rate of 55 RPM. Since the flow was time dependent, a MONARCH PLT200 tachometer was used to identify when the pump accomplished one cycle. The tachometer required a reflective strip of tape on the rotating portion of the pump to indicate the start of the cycle. The tachometer delivered a signal to a delay generator, which allowed various delay times. For instance, the delay was set constant for the dye visualization to ensure recording was initiated at the same point in time between trial runs. The delay time was varied for PIV measurements to allow phase-averaged measurements. Clear vinyl tubing was used to transport the water from the supply tank through the pump and into the aneurysm model. The aneurysm model was 3D printed out of silicone and consisted of one inlet and two outlets as shown in Figure 22. The silicone model was submerged in water to minimize optical distortion since the index refraction of water and silicone are similar with values of 1.333 and 1.336, respectively. The aneurysm sac was also positioned downward to mitigate the number of bubbles attached to the aneurysm wall.

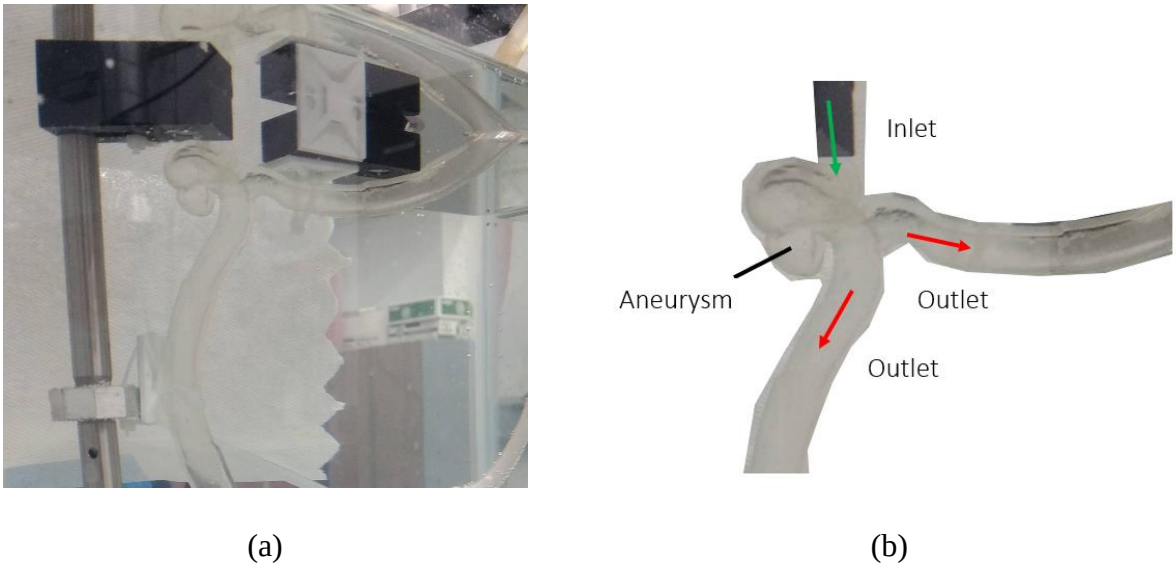

(a) (b)

Figure 22: Aneurysm model within the water tank (a); inlet and outlet regions of the aneurysm identified.

A catheter was inserted upstream of the aneurysm where either dye, for dye visualization, or particle filled water, for PIV, was injected into the system. The fluid was pumped through the catheter via syringe pump from Harvard Apparatus. The volume flow rate of the syringe pump was set at 20mL/min.

4.5.1. Dye Visualization

The setup for dye visualization consisted of an open system. Two tanks were used: The first was the supply tank of clear water and the second tank was for the discharge of dye and water mixture. This setup required an open system because the contrast of dye and water was crucial in obtaining accurate results. Blue dye was injected via the syringe pump at a rate of 20mL/min. Images were gathered by a Photron HS-2000 high speed camera at a frame rate of 2000 frames per second and a resolution of 512 x 512 pixels. The camera was triggered by the delay generator signal. When the tachometer sent a signal to the delay generator, the delay generator waited 50 milliseconds before triggering the speed camera each run. This allowed each run to start at the

same time in the pump flow cycle. This process was repeated for 100 runs, where each run consisted of two full cycles, thus a total of 200 trials were conducted.

4.5.2. PIV

For the PIV setup, the system was altered to a closed system. Instead of the water discharging to a second tank the water was recycled into the supply tank. The reasoning behind this setup was the particles used to seed the flow were already in the supply tank, therefore the recycling of the water prevents the need to add particles throughout the trials. Another reason was because the syringe was filled with the supply tank water, which contained the particles. Therefore, the contrast needed from the dye visualization was not needed in this setup. Particles used in this experiment were fluorescent red polyethylene microspheres with a diameter of 75-90 micrometers and a density of 0.9932 grams per cubic centimeter. Since the particles had a lower density than water, the particles required some preparation to prevent particles non-homogeneous mixtures. Water was heated and boiled for five minutes, then 0.2 grams of dish soap was added to 200 mL of water [61]. Particles were then added and mixed until the particles and water were homogeneous. The laser used was a 532-nanometer laser from New Wave Research. The laser was triggered directly by a second delay generator which controlled the timing for both laser pulses as well as the camera. Images were acquired through a PCO pixelfly camera. The first delay generator, activated by the tachometer, delivered a signal to the second delay generator. For this setup the first delay generator had various values since PIV can only capture one instant in the pump's phase. Thus, the PIV system consisted of phase-lock measurements. Results at each phase were averaged, where each phase consisted of 200 recordings.

4.5.3. Results

There were ten different phase-lock measurements from PIV which could be compared with the dye visualization measurements. However, dye was not present within the aneurysm for all phases which resulted in only two of the time periods suitable for comparison. Comparisons for times at 0.590 seconds (t/T = 0.54) and 0.698 seconds (t/T = 0.63) were made between the dye visualization and PIV measurements. The differences in u-velocity and v-velocity between PIV and dye measurements for the two phases were analyzed and discussed. For phase t/T = 0.54, the u- and v-velocities were compared across horizontal lines at y-locations 2.45mm, 1.64mm, 0.025mm, and -0.78mm. These locations are shown below overtop of the DVV and PIV vector fields.

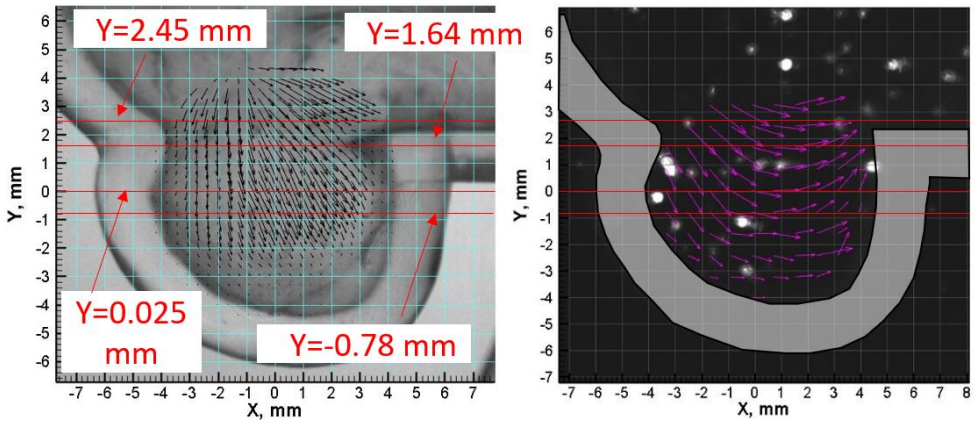

(a) (b)

Figure 23: Velocity field comparison at t/T = 0.54 of (a) DVV and (b) PIV for four y-locations

Results for t/T = 0.54, indicate the dye setup calculates a u-velocity value 23% of the PIV measurement at y = 2.45mm. The PIV results provide a maximum u-velocity of 0.13 m/s and the dye visualization had a maximum velocity of 0.03 m/s. Comparing the v-velocity shows the dye visualization was 36% of the maximum PIV v-velocity. Though DVV underestimates the

velocity, DVV was able to resemble similar profiles for the u- and v-velocities, except at x = 1.2mm where the v-velocity moves upward in PIV. At y = 1.64mm the dye measurements have a similar percentage for the u-velocity and v-velocity when comparing to the PIV values, 23% and 36%, respectively. However, the v-velocity profiles indicate DVV was not able to resolve the change in fluid motion at x = 0.9mm. Related results are seen at y = 0.025mm and y = -0.78mm, where the u-velocity and v-velocity magnitudes are less than the PIV results by almost an entire order of magnitude. Maximum u-velocity for PIV at y = 0.025mm was 0.116 m/s and DVV was 0.021 m/s. V-velocity for PIV peaked at -0.099 m/s whereas DVV peaked at -0.037 m/s. For y = -0.78mm, PIV had a maximum u-velocity and v-velocity of 0.104 m/s and -0.078 m/s, respectively, whereas DVV had velocities of 0.014 m/s and -0.028 m/s, respectively. Notice in figures (b), (c), and (d) below, the v-velocity plots show a change in direction around x = 1mm for the PIV results, but DVV fails to capture the upward motion of the flow.

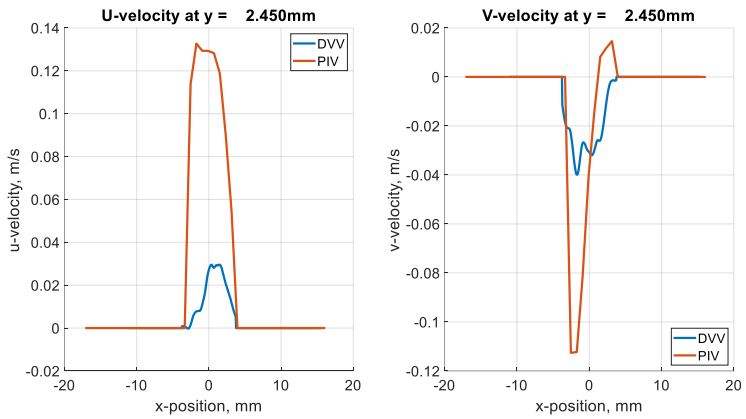

(a)

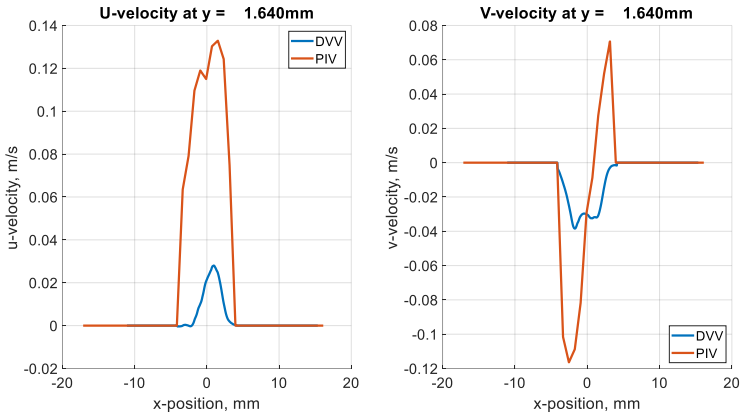
U-velocity at y = 1.640mm
u-velocity, m/s
x-position, mm
DVV
PIV
V-velocity at y = 1.640mm
v-velocity, m/s
x-position, mm
DVV
PIV

(b)

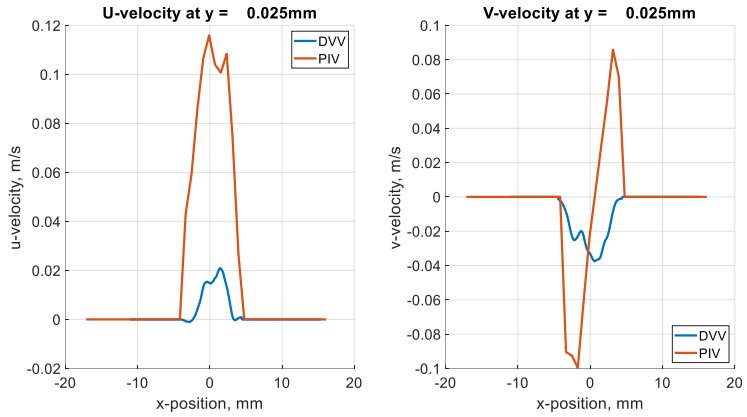

(c)

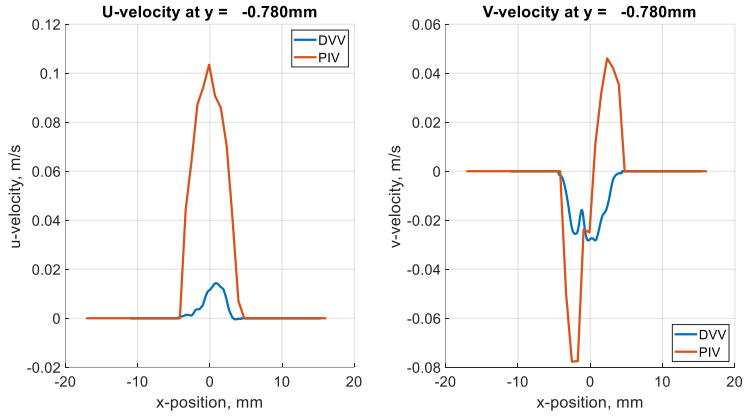

(d)

Figure 24: Velocity comparisons between PIV and Dye Visualization for t/T = 0.54 at (a) y = 2.45mm, (b) y = 1.68mm, (c) y = 0.025mm, and (d) y = -0.780mm

For phase t/T = 0.63, the vector fields for (a) DVV and (b) PIV are displayed in Figure 25 which reveal circulatory motion about the center of the aneurysm sac for PIV, but DVV illustrates more of a uniform motion with little to no circular motion. Notice the velocities for DVV near the bottom of the aneurysm sac are substantially low with movement acting normal to the surface.

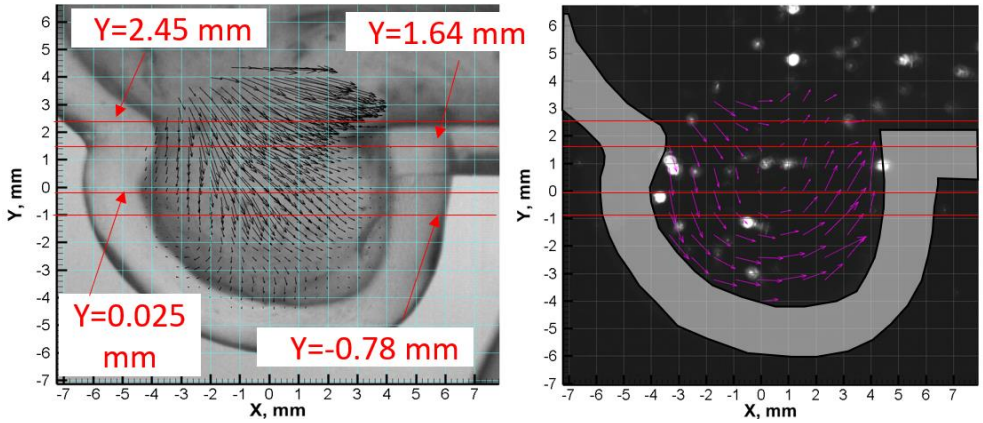

(a) (b)

Figure 25: Velocity field comparison at t/T = 0.63 of (a) DVV and (b) PIV for four y-locations

The results for the u-velocity and v-velocity are better relative to t/T = 0.54, but DVV continues to underestimate PIV results for y = 2.45mm. The maximum u-velocity is 56% of the maximum PIV velocity which were 0.038 m/s for DVV and 0.068 m/s for PIV. The v-velocity for DVV was half the magnitude of PIV, with the maximum velocities of -0.036 m/s and -0.071 m/s, respectively. However, the v-velocity from DVV fails to attain negative to positive transition near the center of the aneurysm, whereas PIV exhibits a transition at x = 0.1mm. At y = 1.640mm, the u-velocity magnitudes of the dye and PIV have a similar magnitude for the first peak, where the both u-velocities for DVV and PIV were 0.034 m/s but these measurements were offset by 1.4mm. Comparing the maximum u-velocity results in an underestimation of 19% from DVV. The dye measurements exceed the PIV magnitude by 0.02 m/s at x = 0mm, but most of the other locations display PIV values greater than the dye measurements. However, the dye v-velocity was 26% of the PIV velocity and does represent a similar profile. DVV's u-velocity at y = 0.025mm has a maximum velocity which is about 25% of the PIV's measurements. Comparison of the v-velocity measurements are disappointing as the dye measurements show -0.024 m/s and PIV has -0.122 m/s, which is approximately 19% of the PIV measurement. For y

= -0.780mm, the u-velocity and v-velocity comparisons are poor. The difference for u-velocity is about 0.045 m/s or about 82% error. Error for the v-velocity is 83% with a difference of 0.1 m/s.

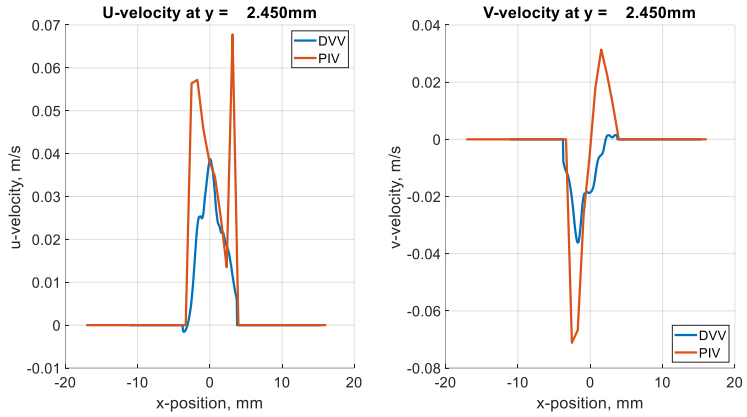

(a)

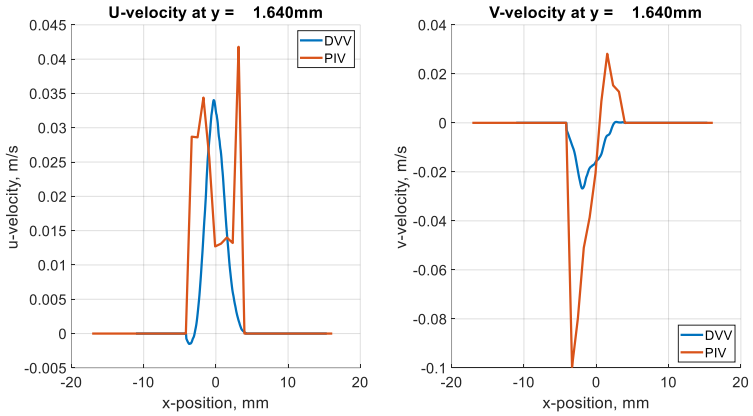

(b)

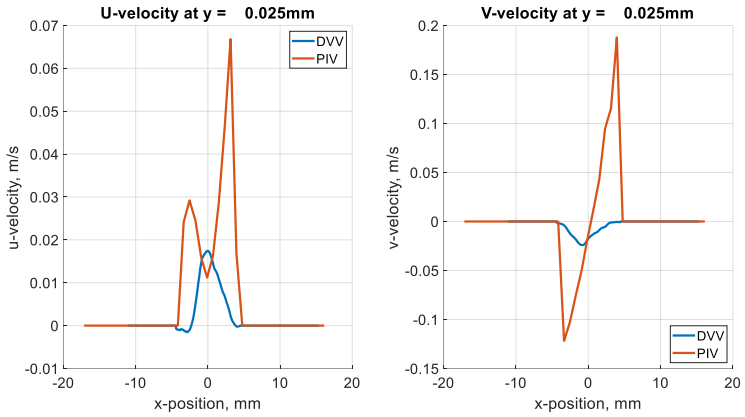

(c)

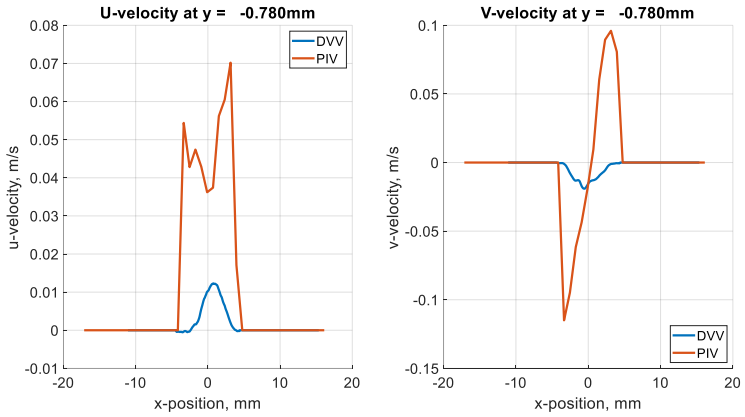

(d)

Figure 26: Velocity comparisons between PIV and Dye Visualization for t/T = 0.698 seconds at (a) y = 2.45mm, (b) y = 1.68mm, (c) y = 0.025mm, and (d) y = -0.780mm

4.5.4. Conclusion

The results from the dye visualization had large discrepancies with the PIV results. For instance, the u-velocity values were about half the value, on average, of the PIV results. This is seen for the time phase t/T = 0.54, however at t/T = 0.63 the velocities were comparable when the y-location was above the center of the aneurysm. When the y-location approaches the center of the aneurysm the accuracy declines rapidly. This suggests the 3D flow within the center of the

aneurysm introduces significant error into the dye measurements. Further observation of the image sets for each time period indicate there is more dye contrast incorporated in the images within the time frame of t/T = 0.63, which can be viewed in Figure 27.

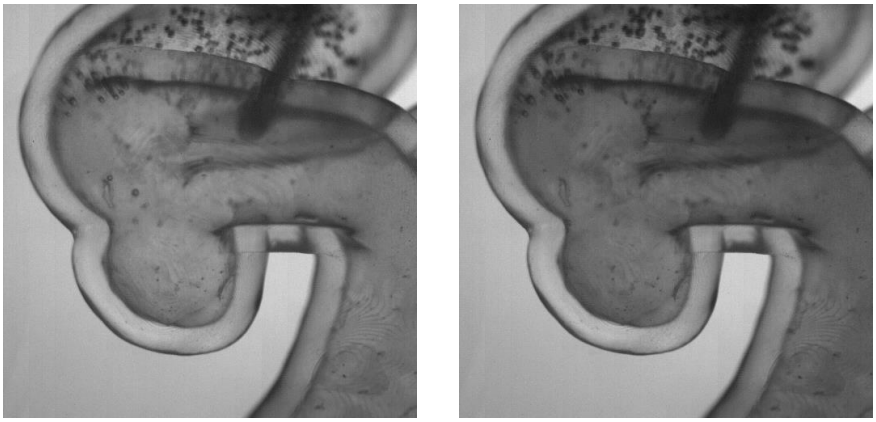

(a) (b)

Figure 27: Dye contrast comparison between the two phases (a) t/T = 0.54 and (b) t/T =

In comparing the v-velocity plots, the dye measurements consistently fail to record the change in direction when x > 0mm. This could be due to the shape of the aneurysm accompanied with the inlet trajectory. At the center of the aneurysm, which was where the PIV measurements were taken, the velocity profile could incorporate movement going down the left side of the aneurysm and up the right side of the aneurysm. However, if the plane was analyzed near the wall of the aneurysm, then the velocity profile could indicate a downward velocity on both the left and right side of the model (see Figure 28). The near wall velocities would be incorporated into the dye measurements, for both the near wall and far wall, thus the velocities at x > 0mm would have negative values.

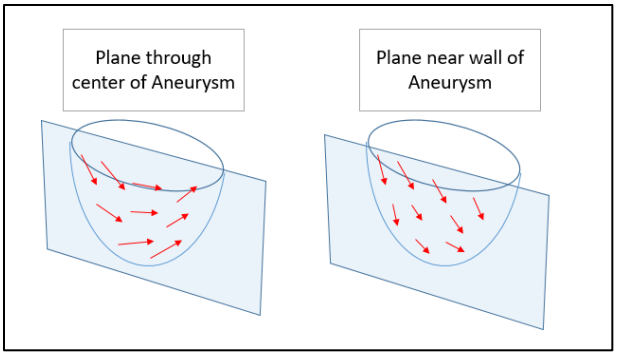

Figure 28: Possible velocity profiles

4.6. Vertical Water Flow with Dye Injection

The purpose of this experiment was to establish a simply controlled flow system which allowed various flow speeds to be analyzed using PIV, dye visualization, and CFD comparisons. Additionally, using a square tube significantly reduces the noise due to reflection, refraction, and blemishes on the wall. Though the square tube involves some stains on the wall which induce noise, the use of CFD simulation avoids this kind of unwanted noise and therefore isolates the error to the 3D volumetric effect. The objective was to compare CFD results between the experiment's velocity, obtained through PIV, and dye diffusion, via dye visualization. Choosing a vertical setup allowed air bubbles to escape through the top and remain unattached to the test section region. This issue occurred in the horizontal tube experiment and required meticulous actions to mitigate air bubbles during the experiment. Secondary objective was to use the CFD results to correct the OFM results for better accuracy in dye visualization.

4.6.1. Setup/Construction

Constructing the vertical flow apparatus consisted of seven sub-systems: 1) Top storage tanks, 2) contraction region, 3) test section, 4) flow regulator, 5) pump-system, 6) dye positioning system, and 7) support structure. The top storage tank was made out of ¼-inch thick acrylic sheets with

width-height-depth dimensions of 24” x 12” x 12.5”, respectively. Acrylic is transparent, durable, and machinable which is why it was selected for the top storage tank. Acrylic pieces were bonded together with Weld-on 3, and silicone caulk was used to waterproof the edges of the tank. The type of silicone used was GE all-purpose silicone caulk. Cure time for the silicone caulk required a day before any water leaking tests could be conducted. One piece of acrylic was placed in the middle of the tank to act as a divider between two sections of the tank. This dividing piece had a slot cut out of the top roughly 1-inch below the top of the tank to allow water to pour into the other side of the tank. To maintain steady conditions in the flow, the water level needed to remain constant. By creating the opening between the main tank and the overflow tank, the water level was able to maintain a constant height throughout the experiment. The main tank contains a cutout in the bottom for the contraction nozzle as well as four threaded holes for mounting the contraction nozzle. To provide additional material for the threaded holes, two pieces of 4” x 4” x 1/4” acrylic were bonded to the bottom of the tank. Without these additional sheets of acrylic, the threading in the bottom would not be sufficient enough to hold the contraction nozzle.

The contraction nozzle was a crucial design component for this experiment as it held the highest impact on the flow quality within the test section. Without the contraction piece the water would have induced turbulence when it traveled from the main tank to the test section. The shape of the contraction had to be specific to allow for a smooth transition and mitigate any disturbances entering the test section. Literature review was performed to design the contraction shape based on the work of Hernandez et al [62]. The acceleration of the flow as well as the non-uniformity attenuations were dependent on the contraction ratio. Larger contraction ratios provided higher quality flow within the test section. The optimum shape of the contraction mitigates adverse

pressure gradients as this type of pressure gradient may cause local boundary layer separation. This separation causes substantial increases in turbulence levels. Determining the contraction shape was based on a fitting polynomial of the following form. The numerical values were determined by imposing conditions at the larger region of the contraction, the smaller region of the contraction, and in the middle of the contraction. These points are visible in Figure 29.

$$y = 1.5 - \left(\frac{3}{512}\right)x^5 - \frac{15}{256}x^4 + \frac{5}{32}x^3 \tag{11}$$

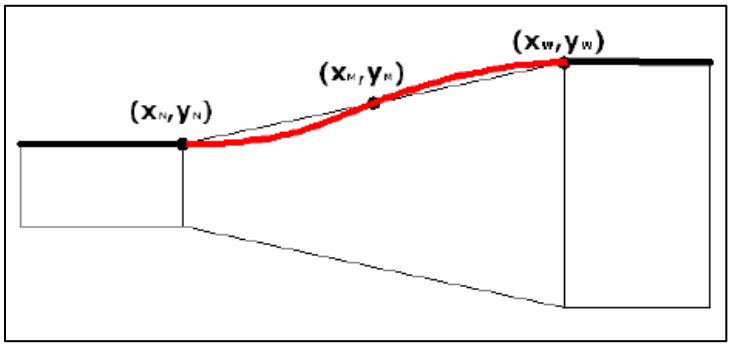

Figure 29: Diagram of the contraction design with the x- and y-coordinates for the narrow section, middle section, and the wider section. [62, Hernandez]

Since the contraction region required a smooth curvature, the model was created with 3D printing. The material used was Somos WaterShed XC 11122. This type of material had comparable properties of ABS and PBT, which results in a waterproof material. Another consideration in selecting 3D printing and the type of material was the surface roughness. Having a rough surface would cause flow disturbances and reduce the efficiency of the contraction. The 3D printing company was able to print the model with 0.002-inch layers which provided the model with a smooth surface. The final design of the contraction region is displayed in Figure 30.

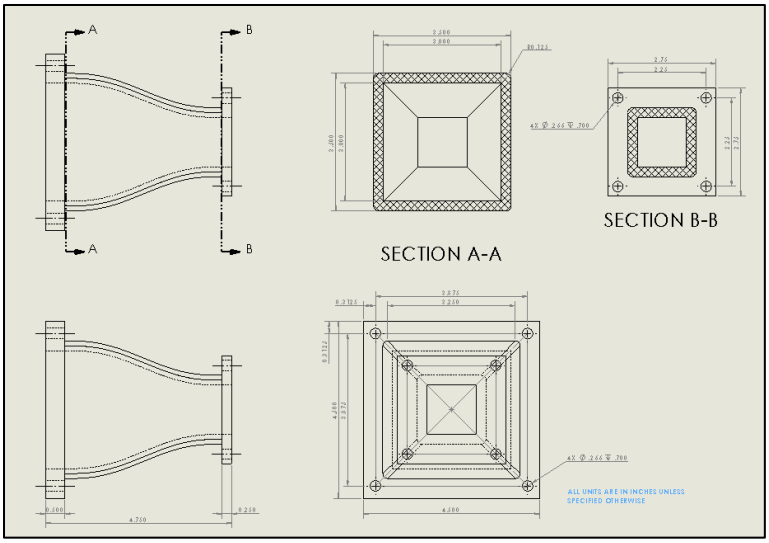

Figure 30: Engineering drawing of the final design of the contraction region.

In designing of the test section, the major concerns were with the visibility of the flow within the section as well as maintaining a smooth transition from the contraction nozzle. Based on these concerns the acrylic square tubing was selected. Acrylic has good transparency and is machinable. The inlet of the square tubing required a tapered region which means the part needed to be machined. Below is the final drawing of the test section with machining.

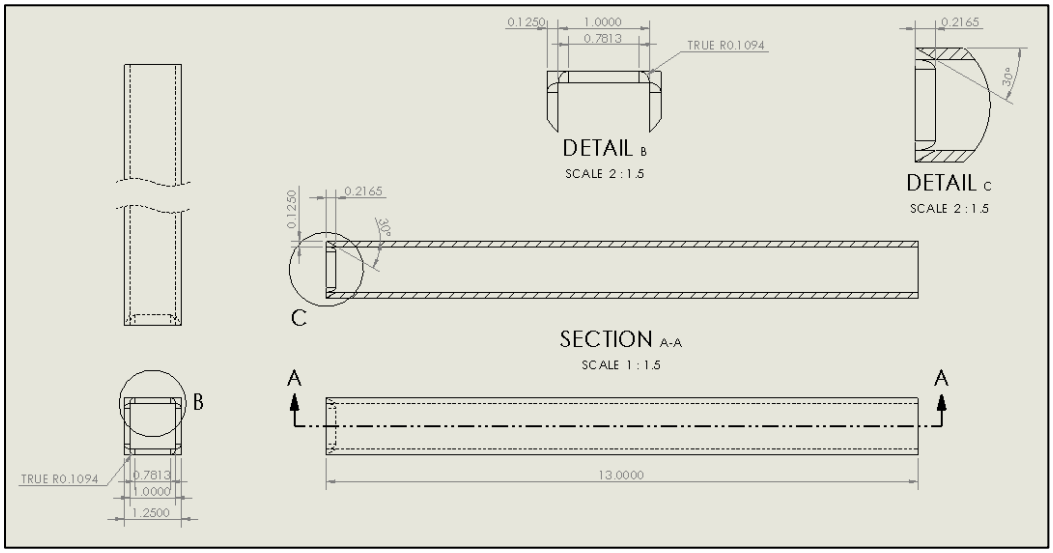

Figure 31: Engineering drawing of the test section made out of acrylic square tubing.

To control the velocity of the flow, a flow control valve was placed underneath the test section. The flow valve was a ¾" NPT balancing valve with flow meter from Caleffi. Flow rate could be adjusted with an adjustable wrench which changed the position of the internal ball valve. A pump was required to move water from the discharge tank up to the main tank. After performing standard head loss calculations for the pumping system, a pump was selected. The pump selected was an adjustable flow inline circulation pump with 1/8 horsepower and 120V AC system. There were three flow speeds to choose from if water within the main tank was running too low or too high. Tygon tubing was placed into the discharge tank and connected to the in-line pump with an adapter. Another set of tygon tubing was connected to the discharge port of the pump on one side and placed into the top of the main tank. Another critical component was the dye positioning system since the position of the dye inlet within the experiment had to be reflected in the CFD geometry. Centering the dye inlet required two linear guides mounted to one another in opposite directions. This allowed movement in the x- and y-direction. Maintaining a parallel angle with the flow and dye inlet cylinder was achieved by placing a tri-axial camera mount on the linear guides. Structural support for the dye positioning system was comprised of T-slot aluminum with quad-profile rails and rectangular structural brackets, for additional strength. Figure 32 shows the final construction of the positioning system and the structural support.

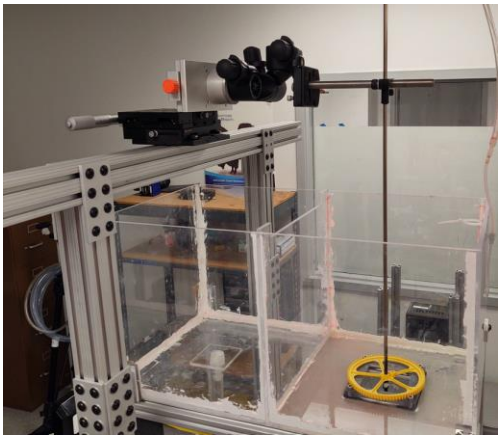

Figure 32: Dye inlet positioning device and structural support with two linear guides for translational movement and a tri-axial mount for angle adjustments.

The support structure of the storage tank included eight feet of 80/20 T-slot aluminum which were held together through the use of eight corner brackets. The brackets were mounted to the T-slot aluminum with four 1/4"-20 hex drive socket cap screws along with a washer and nut for each screw. The 80/20 T-slot aluminum was selected for their versatile framing configurations. The slots were continuous throughout the rails which provided for easy adjustments. For example, the height of the main tank and overflow tank needed to be raised to provide sufficient clearance for the main test section. Elevating the tank was simple through the use of the T-slot aluminum structure. Construction of the final design can be viewed below.

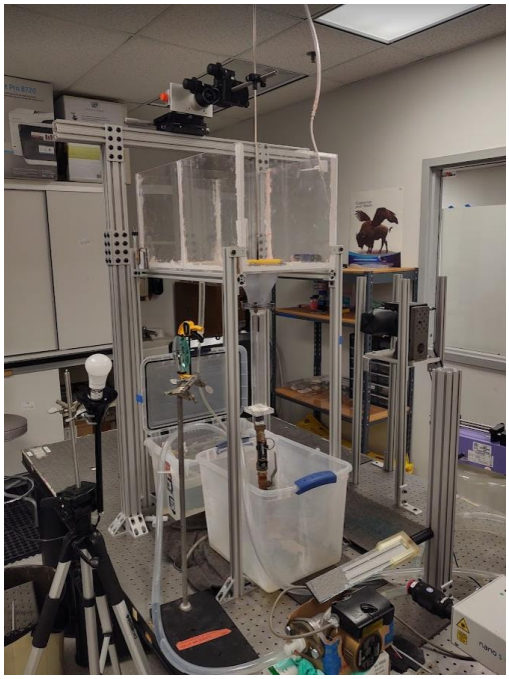

Figure 33: Completed construction of the vertical flow chamber.

4.6.2. Laminar Flow

Investigating laminar flow was crucial in understanding the error associated with dye visualization over a full spectrum of fluid motion, since flow patterns within arterial blood flow is primarily spiral laminar flow [63]. To establish laminar flow, the flow valve was adjusted until the flow speed resulted in a Reynolds number of $Re = 320$, which was an average flow rate of 0.016 m/s.

4.6.2.1. Dye Visualization Velocimetry

For setting up the dye visualization part of the experiment, a syringe pump (Harvard Apparatus 11 Plus) and tygon tubing was needed to distribute the dye into the test section. The syringe pump was set at 5.00 mL/min and the tygon tubing was inserted inside of the metal tube which was held by the dye positioning apparatus. The dye positioning apparatus

was used for two positions: 1) dye in the center and 2) dye against the center of a wall. A high-speed camera (FASTCAM Mini) was used with 3200 frames per second and resolution of 896 x 672 pixels. Total of 100 trials were conducted where five seconds of elapsed time were captured with the high-speed camera, which resulted in images containing dye starting to enter the region and the head of the dye exiting the camera view. LED color light bulb was used to illuminate the test section and transmit light rays through the dye and project the image onto the camera view plane. Multiple colors were tested, including white, and the optimal color was red since it produced the largest contrast with the blue dye and had a relatively low brightness. In between the light source and test section was a convex lens with a focal length of 200 mm. Reasoning for the convex lens was to rearrange the light rays in a parallel fashion, so the intensity of the light was more uniform throughout the entirety of the image. Having uniform intensity in the image was incredibly important for accurate results from the OFM technique. Images obtained from dye injected in the center are presented in Figure 34 and dye injected at the wall are shown in Figure 35.

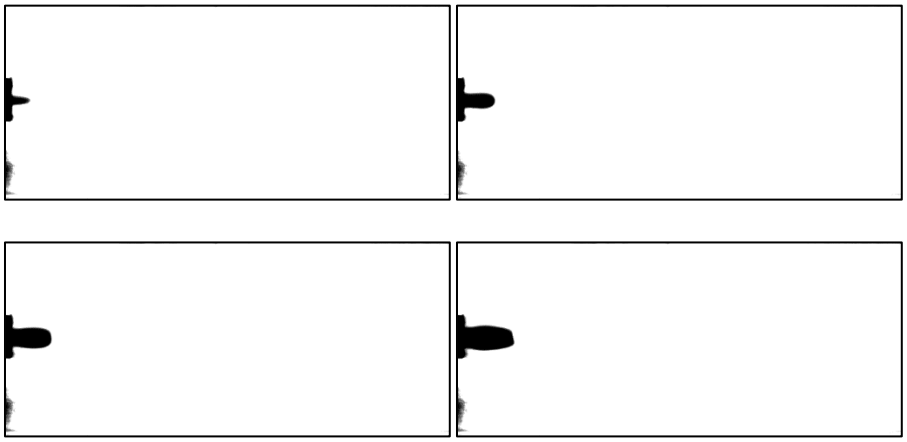

Figure 34: Images from one of the 100 trials conducted for the dye visualization experiment where dye was injected in the center.

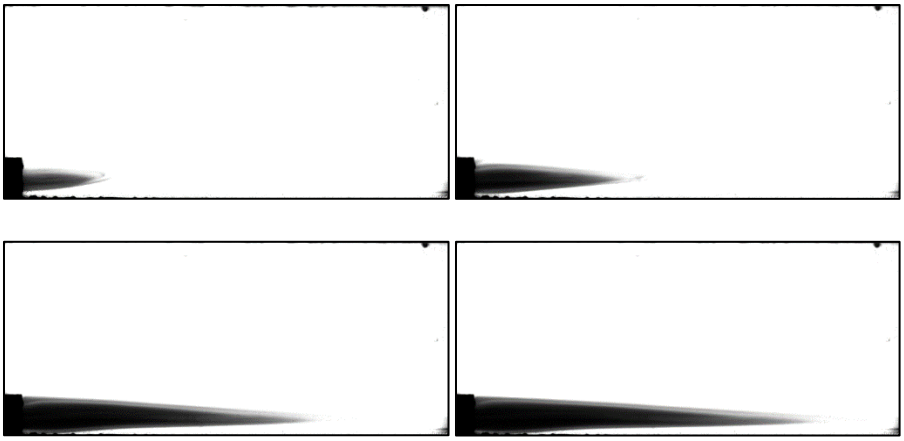

Figure 35: Images from one of the 100 trials conducted for the dye visualization experiment where dye was injected at the wall.

4.6.2.2. PIV

In conducting PIV for the vertical flow, a LaVision PIV system was used for both the center and near wall case. Laser used was a Nd: YAG medium with a wavelength of 532 nanometers and maximum output of 300 milli-joules. System used a programmable timing unit (PTU) from LaVision which synced the laser output and camera acquisition together for capturing the images. DaVis 8.0 software was used to control the pulse power intensity as well as time between images within a set. Frequency of the laser was set at 30 Hz and an exposure time of 15 microseconds was used. Since the flow was relatively slow, a single frame analysis was conducted on 1000 images, therefore 999 instantaneous velocity fields were calculated for each plane. Total of 5 planes were investigated. One at the center of the square tube, two were ±5 mm from the center, one +8 mm from the center, and one +10 mm from the center. The center plane would be used in comparison with the OFM results, and the other planes were used for determining the boundary conditions of the CFD simulation as well as centering the dye inlet tube. Fluorescent red polyethylene microspheres with a diameter ranging from 10-45 micrometers were used to seed the flow. From previous experience, the particles tended to float on top of the water which resulted in sparse particles

in the flow. To suspend the particles in the water, a tween solution was created which consisted of 2.5 grams of dish soap dissolved into 1800 milliliters of boiling water [58]. Approximately 5 milliliters of particles were mixed thoroughly into the tween solution before being poured into the top storage tank. Some of the mixture containing the particles were set aside to be injected into the flow by the syringe. Exciting the particles with the laser produces a fluorescent emission with a wavelength of 610 nm, which is why a high pass filter of 600 nm was applied to the camera for filtering laser illumination and reflection. A 14-bit charge-coupled device (CCD) camera (PCO, Pixelfly QE) with a resolution of 1392 × 1040 pixel (66 × 49 mm) was used for the PIV experiment. Below are images collected from the PIV setup for the center plane position and 5mm in front of the center plane.

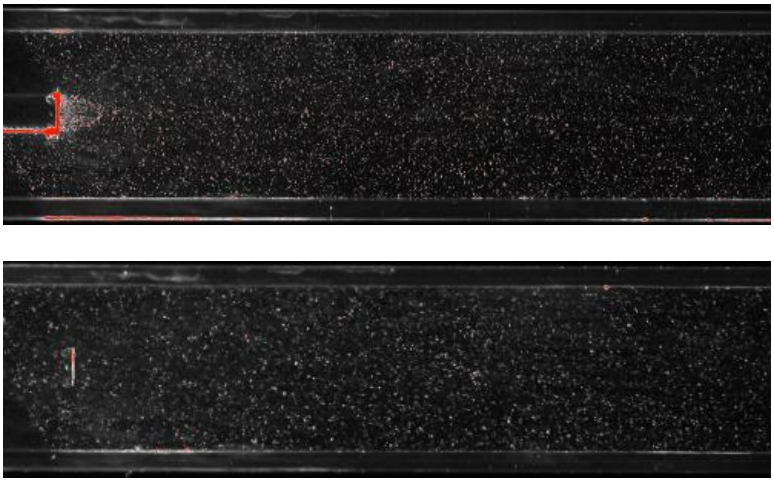

Figure 36: PIV sample image at the center plane (top) and 5mm in front of the center plane (bottom).

Post-processing was performed in DaVis where a multi-pass cross-correlation analysis was conducted. The correlation started with a 64x64 pixel interrogation region with 50% overlap, then a second pass was conducted with an 8x8 pixel window size with 50% overlap. Results of the 999 instantaneous velocity fields, from each plane, were averaged together using a C++ program.

4.6.2.3. Results

Before results of the velocity field from PIV could be acquired, the centering location of the dye inlet had to be verified. This required a comparison between two planes equidistant from the center plane, hence two planes were measured at ±5 mm from the center plane. Figure 37 displays the velocity contour obtained from +5 mm from the center plane and exhibits the four locations, indicated by the vector profiles, used for comparison with the -5 mm plane.

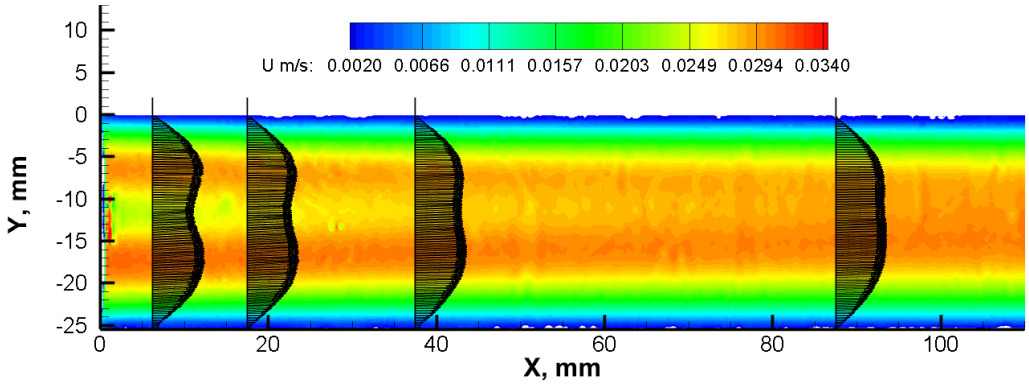

Figure 37: Velocity contour of the plane 5 mm behind the center plane with vectors extracted along four different lines.

Theoretically, planes +5 mm and -5 mm should have the same velocity profiles since the domain is symmetrical. To provide a comparison with the CFD results these two planes were compared to identify how much error was introduced from non-symmetric placement of the dye-inlet tube. The four velocity profiles used for comparison were located at X = 6 mm, 17.5 mm, 37.5 mm, and 87.5 mm downstream of the dye inlet.

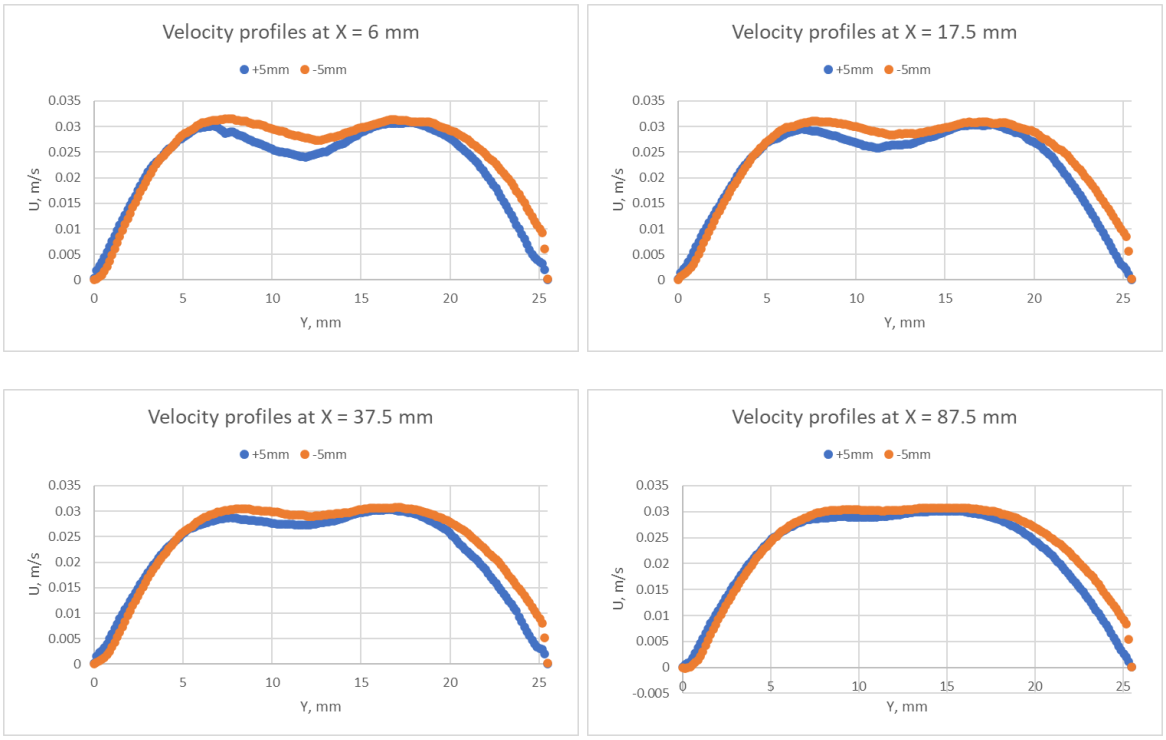

Figure 38: Velocity profiles at X = 6 mm, 17.5 mm, 37.5 mm, and 87.5 mm for comparison with the equidistant planes 5 mm from the center plane to validate dye inlet centering position.

The average percent difference was calculated based on values between 5 mm and 20 mm since this range incorporated the peak velocity and variation in the velocity profile. Near the dye inlet, X = 6 mm, the average error was 6.7% and an error of 5.4% was calculated at X = 17.5 mm. For profiles further downstream, X = 37.5 mm and 87.5 mm, the average error was 4.5% and 3.4%, respectively. Though the error near the dye inlet was slightly above 5%, the dye inlet position was considered centered since the error overall was around 5%.

With the dye inlet centered, the rest of the PIV planes could be processed and used for comparison with CFD, comparison with OFM, or determining boundary conditions for the CFD simulation. Four planes were of interest, including the +5 mm plane. The contours shown in Figure 39 are of the center plane, +5 mm plane, +8 mm plane, and +10 mm plane for the dye in the center.

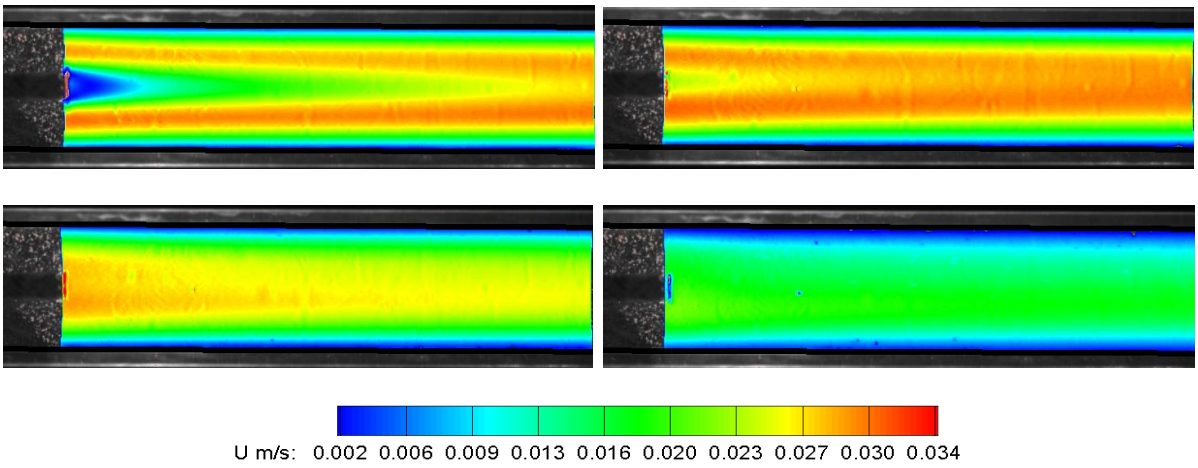

Figure 39: Velocity contours of the center plane (top-left), +5 mm plane (top-right), +8 mm plane (bottom-left), and +10 mm plane (bottom-right) for dye in the center.

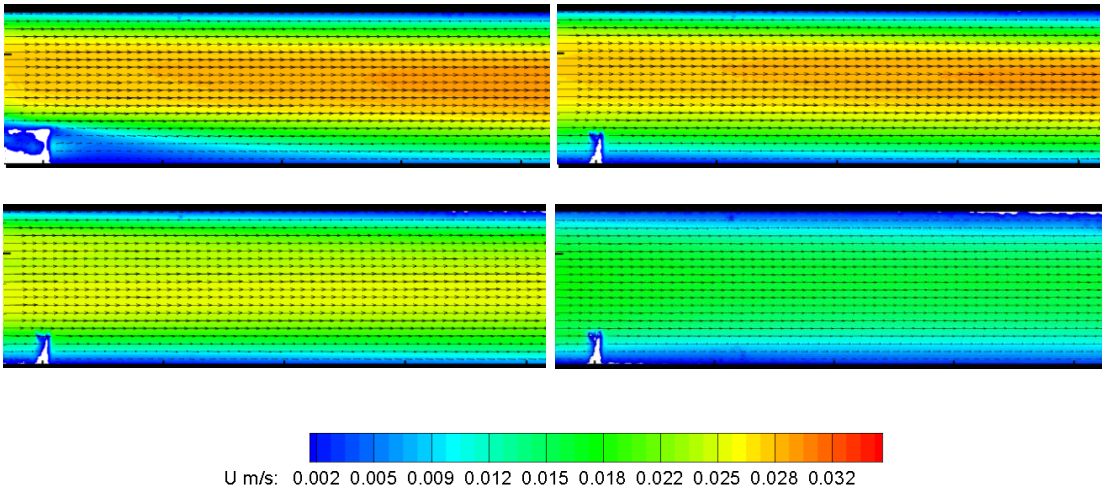

Figure 40: Velocity contours of the center plane (top-left), +5 mm plane (top-right), +8 mm plane (bottom-left), and +10 mm plane (bottom-right) for dye near the wall.

To see the accuracy of the dye visualization velocimetry method a comparison was made between the OFM results and the center plane velocity from PIV. Averaging the OFM results was completed by first averaging 20 vector fields calculated from 21 successive images within one trial at each of the six dye displacement positions, for dye in center case, and 7 dye displacement positions, for dye near the wall case. Then each of these average files were

averaged with their respective counterpart within each of the 100 trials. For example, six average files were calculated among all the trials for the center case and seven average files for the near wall case. The dye images in the center used for each of the dye displacements (16.5 mm, 20.7 mm, 37.3 mm, 41.5 mm, 45.6 mm, and 49.8 mm) were determined based on a MATLAB program which identified the location of the dye head for each of the trials. The same MATLAB program was used for the near wall case as well. From the contour plots displayed below, it is clear the OFM technique calculates vectors associated with large contrast gradients which occurs at the head of the dye. Velocity values from the OFM contours were extracted in the x-direction for direct comparison with the PIV results. Figure 42 shows the velocity distributions between PIV and OFM for dye in the center. When the dye displacement reached 16.5 mm, the average error was 6.2% while the average error at 20.7 mm was 14.5%. The error continued to increase from 16.0% to 26.6% when the dye had traveled 37.3 mm and 41.5 mm, respectively. For displacements of 45.6 mm and 49.8 mm, the average error was calculated from the region enclosed by the red brackets in Figure 42, since these regions correspond to where the head of the dye was located. The resulting errors for 45.6 mm and 49.8 mm were 9.4% and 5.3%, respectively.

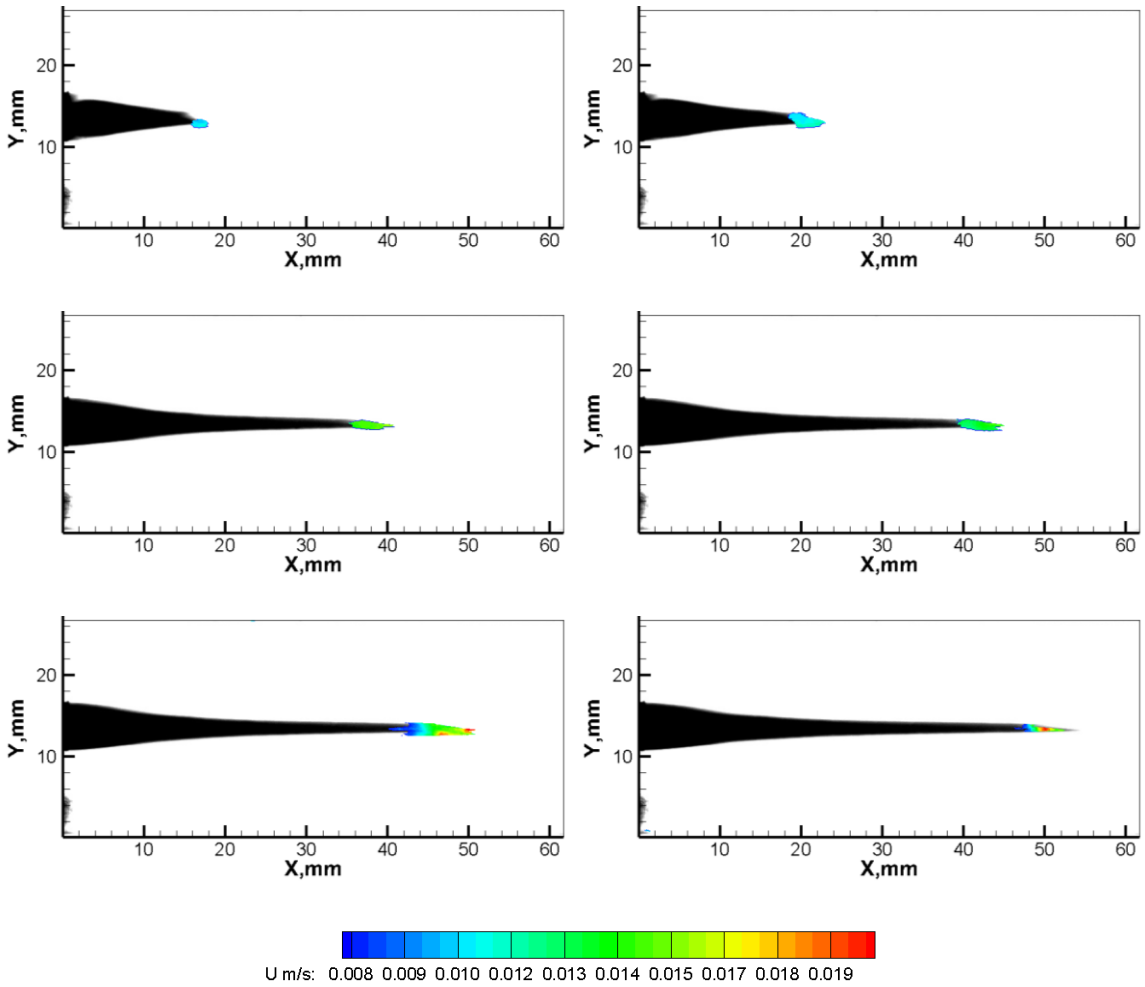

Figure 41: Dye visualization velocimetry contour for various dye head locations.

Figure 42: Velocity comparison between OFM technique and PIV technique for various dye displacement positions.

For the dye displacement at 16.5 mm, 20.7 mm, 37.3 mm, 45.6 mm, and 49.8 mm, the results are reasonable to the PIV results which supports the notion OFM being used to calculate the velocity at the center plane with a degree of error. However, the displacement at 41.5 mm has a large amount of error which could be caused from inferior intensity gradients associated with defects in the square tube at that point.

Contours of the dye injected near the wall are presented below along with a table associated with the error calculated between DVV and PIV for each position. The error was calculated based on the same methodology used for the dye in center case. The seven x-locations are identified as 8.77 mm, 13.17 mm, 17.67 mm, 22.10 mm, 27.6 mm, 32.80 mm, and 36.28 mm which are displayed in the figure below.

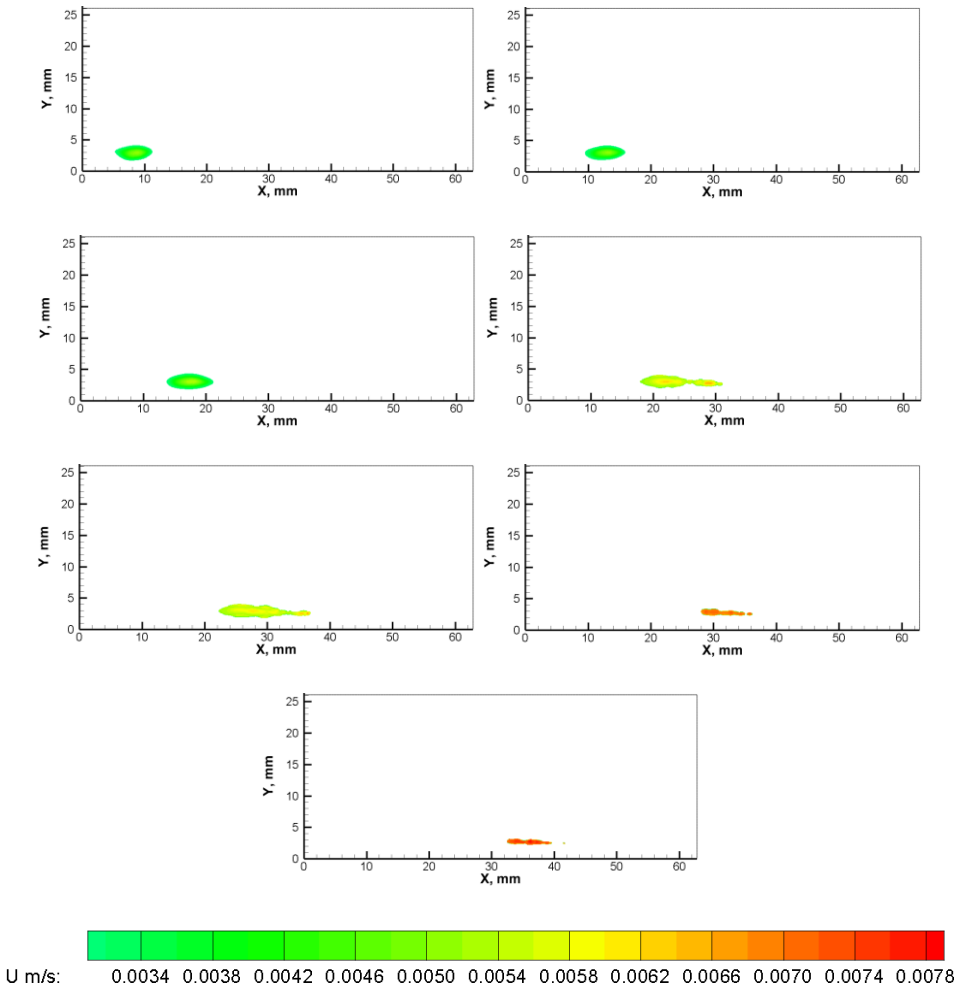

Figure 43: DVV U-contours for the dye near wall case.

The velocity contours illustrate wider dye heads near the dye inlet, but as the dye propagates downstream the dye head narrows which results in thinner contour regions where x > 30 mm. Comparisons between DVV and PIV were made for each of the locations and an error was calculated for the respective location. These results were tabulated in the table below.

Table 3: Error associated with DVV measurements near the wall in comparison with PIV measurements.

Dye Near Wall							
Y-Location, mm	8	13	18	22	28	32	37

Error	8.1%	18.4%	28.2%	20.3%	33.5%	32.5%	32.6%

Notice how the error continues to increase as the dye propagates further downstream, which has similar trends as the dye in the center. However, the error is larger for dye near the wall since the flow is slower which provides ample time for the dye to diffuse outward, thus the 3D volumetric effect becomes more pronounced. Dye near the wall has a maximum error of 33.5% whereas the dye near the center had a maximum error of 26.6%.

4.6.3. Turbulent Flow

Turbulent flow was studied to investigate the characteristics of dye diffusion as well as understand the error associated with DVV for faster flow speeds. Clinical studies have confirmed flow within large and giant intracranial saccular aneurysms, which are associated with high mortality and morbidity, contain turbulent flow [64]. To create turbulent flow in the vertical squared tube, the flow valve was opened to increase the average speed to 0.305 m/s which results in a Reynolds number of 6,103. Both DVV and PIV were conducted to understand and quantify the difference in velocity between the two methods.

4.6.3.1. Dye Visualization Velocimetry

Equipment used for the laminar setup was the same for the turbulent setup, however parameters for some of the equipment were modified to adjust for the faster flow rate. The syringe pump rate was increased to 10.00 mL/min otherwise the images would have poor dye contrast and gradients, which would negatively impact the accuracy of DVV. With respect to the high-speed camera, the frame rate was increased to 5000 fps which resulted in a resolution of 909 x 367 pixels. Frame rates slower than 5000 fps resulted in movements greater than 1.5 pixels between images which would decrease the accuracy of DVV. This frame rate allowed 1.789 seconds of recording time and the pixel scaling was measured as 7.366E-5 m/pixel. Due to the stochastic

nature of turbulent flow, a total of 400 trials were conducted to provide a larger sampling size during the averaging process. Example images from one of the trials are displayed below to illustrate some of the dye diffusion patterning.

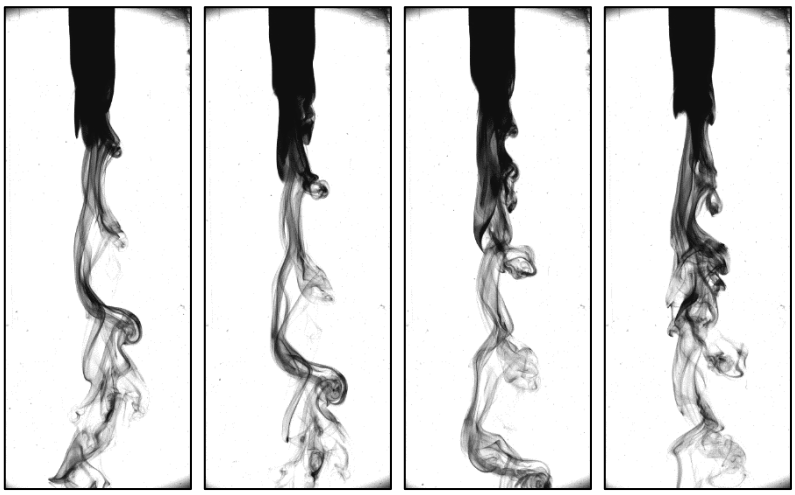

Figure 44: Experimental images obtained from dye visualization for t = 0.0 sec, 0.029 sec, 0.084 sec, and 0.126 sec (left to right) during turbulent flow study for one of the 400 trials.

4.6.3.1. PIV

The PIV system used for the laminar case was also used for the turbulent case, however some of the settings were modified to accommodate the higher flow speed. In the laminar case the images were taken sequentially by a single frame, but the turbulent case required double frame recording with double pulse laser emission. The frequency of the PIV setup was set at 24.86 Hz and a time between frames Δt = 200.3 μs. PIV was conducted on four different planes: 0mm (center), 5mm, 7mm, and 10mm offset from the center. Raw images from the (a) center and (b) 5mm planes are displayed below.

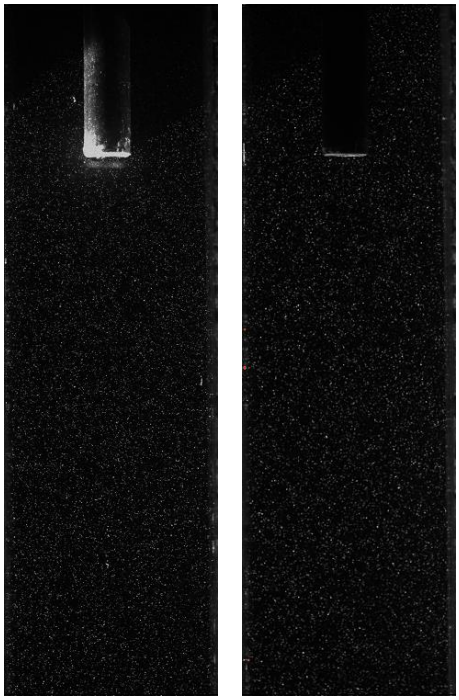

(a) (b)

Figure 45: Raw PIV images for the turbulent flow case located at the (a) center and (b) 5mm plane.

Post-processing was performed in DaVis where a multi-pass cross-correlation analysis was conducted. The correlation started with a 48x48 pixel interrogation region with 50% overlap, then a second pass was conducted with a 12x12 pixel window size with 75% overlap. Results of the 2000 instantaneous velocity fields, from each plane, were averaged together using an in-house C++ program.

4.6.3.1. Results

For assessing turbulent flow with DVV, 400 trials were conducted which resulted in over 170,000 image pairs during the averaging process. The v-velocity contour for (a) DVV is displayed in Figure 46, where flow regions slower than 0.001 m/s were omitted to visualize regions where dye was present. Note there is a region between the dye inlet and the start of the velocity contour which does not exhibit velocity values, this is a result of too much dye present

which results in low intensity gradients, therefore inaccurate measurements. Another observation is the presence of slower velocities near the edge of the contour, even further downstream of the inlet. This is a result of lower dye concentration as dye convects outward from the center, which results in lower intensity gradients and thus inaccurate measurements. The lower dye concentration, as well as the large dye concentration region below the dye inlet, can be viewed in the experimental images provided in Figure 44.

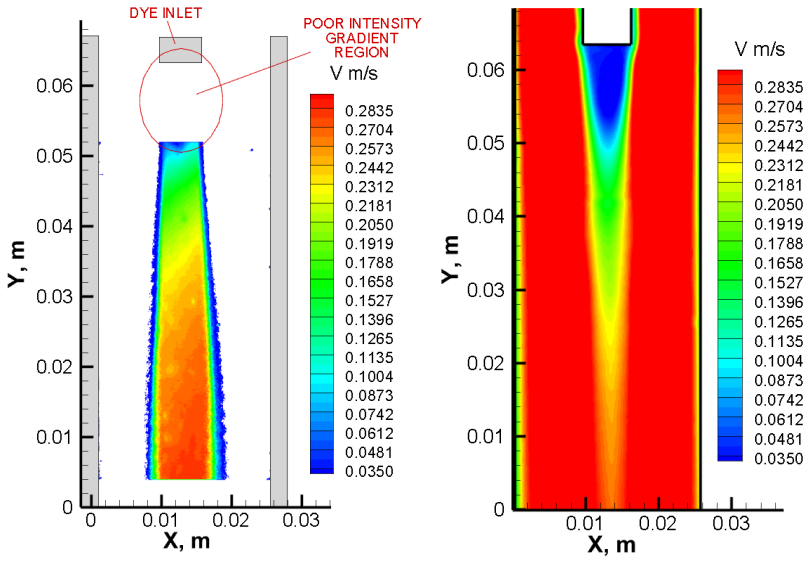

Figure 46: V-velocity contour of the averaged results from (a) DVV for 400 trials and (b) PIV for 2000 instants located at the center plane.

To quantify the accuracy of DVV measurements, 2000 instantaneous measurements using (b) PIV were averaged for the center plane, which can be viewed in Figure 46. From the V-contours, the DVV measurements are similar to the PIV results between y-locations of 0.038m to 0.048m. Velocities located lower than y = 0.038m the DVV results appear to have higher velocities than the PIV measurements. For direct comparisons between PIV and DVV, data was extracted along the center, x = 0.013m, and plotted in the figure below.

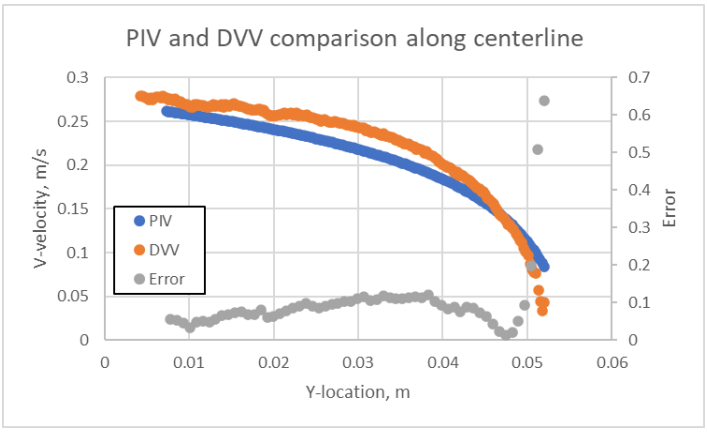

Figure 47: V-velocity comparison between DVV and PIV along with the error for measurements extracted along the center.

The direct comparison shown above reveals the v-velocities from DVV, further downstream of the inlet ($y < 0.045m$), overpredict the PIV measurements which seemed unusual considering previous DVV measurements tended to underestimate PIV. This development will be discussed further in the CFD analysis as the simulation provides additional insight as to why these measurements overpredict PIV. The error is highest near the dye inlet, 63.7%, around $y = 0.05m$ but decreases substantially to about 10% below $y = 0.042m$. Error from y-locations between 0.01m and 0.04m vary with the minimum error of 6.3% and the largest error of 12.0%. The center plane results from PIV were used in comparing DVV, however additional planes were also measured for use in validating the CFD model. The planes measured for CFD validation were located 5mm, 7mm, and 10mm from the center plane and are shown below.

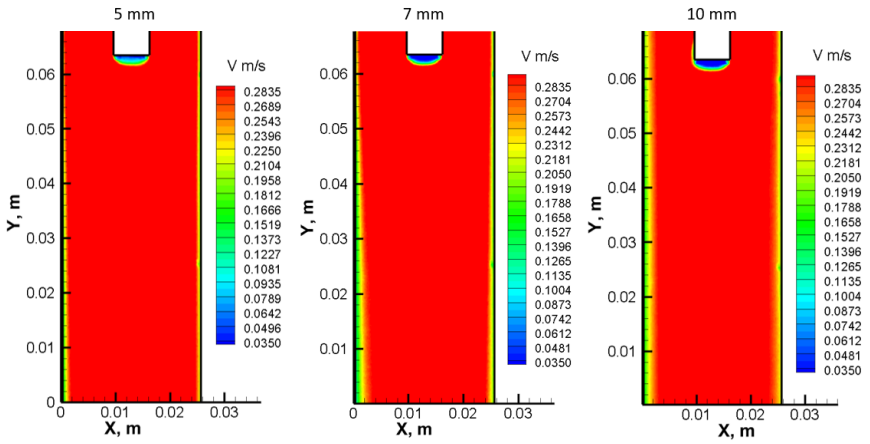

(a) (b) (c)

Figure 48: Average PIV v-velocity contours at planes (a) 5mm, (b) 7mm, and (c) 10mm offset from center.

4.6.4. Conclusion

DVV and PIV were conducted for two flow cases: 1) Laminar flow with a Reynolds number equal to 320 and 2) turbulent flow with Re = 6,103 to investigate the accuracy of DVV through the comparison of PIV measurements. The laminar case provided insightful information regarding the error between PIV and DVV at certain locations downstream of the dye inlet. Error increased downstream as a result of dye diffusing which created an average 3D volumetric effect, but when the dye began to accelerate downstream past 45.6mm the dye converged towards the middle thus reducing the 3D volumetric effect and consequently the error. However, when the dye was near the wall the error did not dissipate downstream due to the slower flow at the wall, thus allowing time for dye to diffuse more. For the turbulent case direct comparisons between DVV and PIV, which was conducted at the center plane, unveiled DVV overestimates PIV measurements further downstream of the inlet for y < 0.038m. This result differs from the laminar case and will be explained further in the numerical analysis section, since the CFD

results provide additional information PIV is not able to display. The average error, for the turbulent case, further downstream of the inlet between y = 0.01m and y = 0.04m was 9.6%.

4.7. Conclusion

Several experiments were conducted to investigate and quantify the accuracy of DVV in comparison to PIV for flows through a horizontal tube, an aneurysm, and vertical squared tube. The horizontal tube and aneurysm experiments involved pulsatile flow generated from a heart pump, which required phase-averaged PIV measurements. Two of the phases were compared for the horizontal flow, where both phases indicated DVV underestimated PIV measurements, especially near the wall. This led to the conclusion of a thick-wall effect which explains how the light transmits through two slow regions near the tube wall, and one high speed region in the center. Therefore, DVV inherits error from the compressing of 3D volumetric flow onto a 2D image. Pulsatile flow through a horizontal tube is relatively simple flow and investigating more complex flows were needed to understand the accuracy of DVV, thus an experiment involving an aneurysm model was conducted. The results were provided for two separate phases, where both phases revealed underestimation from DVV regarding u- and v-velocity quantities. The magnitudes of both the u- and v-components for DVV were consistently half, or worse, of the PIV magnitudes. Furthermore, the streamlines of DVV were noticeably different than PIV, since DVV failed to capture the v-velocity transition from negative to positive as flow traveled down the aneurysm sac wall and back up the other side wall. This elicited sever inaccuracy of DVV within complex flow structures where 3D volume effects are prominent and the need for a correction method to obtain accurate flow measurements. To develop a method for correcting DVV measurements, a new experiment was designed and constructed to avoid pitfalls faced in the previous experiments such as lack of dye, entrapped air bubbles, and easy field of view. The

vertical squared tube provided constant flow rate for varying speeds and consistent dye injection positioning. Two flow rates were examined for either laminar flow or turbulent flow. Dye was positioned either in the center or against the center of the wall for laminar flow and the turbulent case consisted of dye injected in the center of the tube. From the experimental results, the centering of the dye inlet position was confirmed with an error slightly above 5% when comparing two planes equidistant from the center plane. Velocity profiles were extracted from five different planes to assist CFD boundary conditions and velocity comparison with DVV. Averaged results from DVV were compared with PIV for several locations downstream of the dye inlet. For dye injected in the center with laminar flow, the error of DVV increased downstream until the dye was accelerated and converged into the center. This resulted in a decrease in error due to the flow merging the dye in the center and therefore reducing the 3D effect. This was not observed when dye was injected near the wall since the flow was slower at the wall and provided ample time for the dye to diffuse outward thus causing a larger 3D effect and consequently larger error. When the flow speed was increased to induce turbulent flow, the error of DVV reduced and resulted in overestimation as opposed to underestimation for most of the location downstream of the dye inlet. The reasoning for DVV overestimating PIV at the center plane will be explained in the numerical analysis section as the CFD results provide a better understanding of this phenomenon. Overall, DVV tends to underestimate PIV when flow speeds are low which allows dye to diffuse outward and enhance the 3D effect, but when dye converges near the center plane the error reduces.

5. Numerical Analysis / CFD on the Vertical Tube Flow with Dye Injection

Computational Fluid Dynamics (CFD) is a powerful technique which analyzes systems containing heat transfer, fluid flow, and related phenomenon through the use of computer-based simulation. CFD has a broad range of applications such as turbomachinery, aeronautics, chemical processes, biomedical, and more. The ultimate goal of CFD development is to provide accurate solutions and offer capabilities comparable to other computer-aided engineering tools. Reason for the relatively slower development is due to the complexity of the underlying physics, which inhibits a sufficiently complete description of the fluid flow all while sustaining cost efficiency. The growing popularity of CFD is partially a result of the cost to perform similar experiments. For each configuration and additional data point, the cost of the experiment increases since it requires additional personal hours, but with CFD there is an abundant amount of results with little added expense.

5.1. Governing Equations

In computational fluid dynamics, the governing equations of fluid flows are represented by the conservation laws of physics which are mathematical statements [14]. These laws describe the conservation of mass, the rate of change of momentum with regards to forces acting on the fluid, and the rate of change of energy with regards to additional heat and work in the fluid. Simply stated, the main laws are continuity, momentum, and energy. However, there are additional laws

which can be used in CFD such as the species equation which describes the interaction between multiple species within a mixture. Each of these equations are explained in more detail below, but one fundamental assumption is the fluid is considered as a continuum. Therefore, the analysis of the fluid is at macroscopic scales and does not include the effects of molecular interactions and motion. Hence, the results of CFD are represented by macroscopic properties such as density, pressure, velocity, and temperature. Each of these properties are functions of space and time. First is the continuity equation as it represents the rate at which mass enters the system, leaves the system, and the accumulation within the system.

$$\frac{\partial \rho}{\partial t} + \nabla \cdot (\rho \boldsymbol{V}) = 0 \tag{12}$$

Here the density of the fluid is represented by ρ and the time is denoted by t. The velocity, $\boldsymbol{V}$, represents a vector quantity typically represented by the cartesian coordinate components $\boldsymbol{V} = \langle u, v, w \rangle$. Accounting for the movement of the fluid is the momentum equation. The equation below represents the conservation of momentum in the cartesian coordinate system.

$$\frac{\partial (\rho \boldsymbol{V})}{\partial t} + \nabla \cdot \rho \boldsymbol{V}\boldsymbol{V} = \nabla \cdot \boldsymbol{\Pi}_{ij} + \rho \boldsymbol{g} \tag{13}$$

Additional terms are introduced such as the pressure p, the stress tensor $\boldsymbol{\Pi}_{ij}$, and gravity $\boldsymbol{g} = \langle g_x, g_y, g_z \rangle$. The first term on the right-hand side of the equation represents the surface forces per unit volume, which are a result of the external stresses on the fluid element. Under the assumption of Newtonian flow, the stress tensor can be written in terms of the velocity and pressure terms. For brevity, the stress tensor is expressed in compact tensor notation.

$$\boldsymbol{\Pi}_{ij} = \mu \left(\frac{\partial u_i}{\partial x_j} + \frac{\partial u_j}{\partial i} \right) + \delta_{ij} \mu' \frac{\partial u_k}{\partial x_k} - p \delta_{ij} \tag{14}$$

Here the Kronecker delta function is represented by δ_{ij}, where $\delta_{ij} = 1$ if $i = j$ but $\delta_{ij} = 0$ when $i \neq j$. There is the typical dynamic viscosity coefficient μ and a second viscosity coefficient μ' which are related to the coefficient of bulk viscosity κ.

$$\kappa = \frac{2}{3}\mu + \mu' \tag{15}$$

Unless the simulation is interested in the attenuation of acoustic waves or the structure of shock waves, the coefficient of bulk viscosity is set to zero which results in $\mu' = -\frac{2}{3}\mu$ [59]. This simplifies (13) and substituting this simplification into (12) results in the following expression.

$$\frac{\partial(\rho \boldsymbol{V})}{\partial t} + \nabla \cdot \rho \boldsymbol{V}\boldsymbol{V} = \frac{\partial}{\partial x_i}\left[\mu\left(\frac{\partial u_i}{\partial x_j} + \frac{\partial u_j}{\partial i}\right) - \frac{2}{3}\delta_{ij}\mu\frac{\partial u_k}{\partial x_k}\right] - \nabla p + \rho \boldsymbol{g} \tag{16}$$

Since this research involves water as the fluid and zero heat transfer, it is appropriate to simplify the momentum equation by assuming incompressible flow with a constant coefficient of viscosity.

$$\rho\frac{D\boldsymbol{V}}{Dt} = \mu\nabla^2\boldsymbol{V} - \nabla p + \rho \boldsymbol{g} \tag{17}$$

Where D/Dt represents the material derivative and can be expanded as $\frac{D()}{Dt} = \frac{\partial()}{\partial t} + \boldsymbol{V} \cdot \nabla()$. As stated, the simulations at hand did not involve any sort of heat transfer therefore the energy equation was not needed. However, an equation was needed to calculate the dye concentration throughout time and space which leads to the species equation being used.

$$\frac{\partial \rho \varphi_i}{\partial t} + \nabla \cdot (\rho \boldsymbol{V} \varphi_i) = \nabla \cdot (\Gamma_i \nabla \varphi_i) \tag{18}$$

First term represents the rate of change of the concentration within the system and the second term handles the movement of the concentration with respect to convection. Third term accounts for the diffusion of the concentration with regards to concentration gradients. The concentration is denoted by φ_i where the subscript i is used to indicate the equation can be applied to situations containing multiple species. The rate at which the concentration disperses in the diffusion term is symbolized by Γ_i. With these governing equations, the laminar simulations are capable of finding a solution, but a numerical method is needed to solve the equations.

5.2. Projective Images Generation

When light passes through a fluid domain containing dye, the dye attenuates a fraction of the light energy. This attenuation can be modeled with the Beer-Lambert law, which is shown below.

$$\frac{dI_t}{dz} = -I_t(z)\mu(z) \tag{19}$$

The intensity of the transmitted light is represented by I_t, the distance on the pathway is denoted by z, and the attenuation coefficient is symbolized by μ. Variations in the attenuation coefficient are a result of the varying dye concentrations where the larger concentration values (i.e. $\phi = 1$) result in higher coefficient values. Considering the CFD domain as cube-like finite volumes, the Beer-Lambert law can be applied to successive finite volumes to determine the amount of light energy which passes through each volume element (assumed uniform distribution of concentration within the element), as illustrated below.

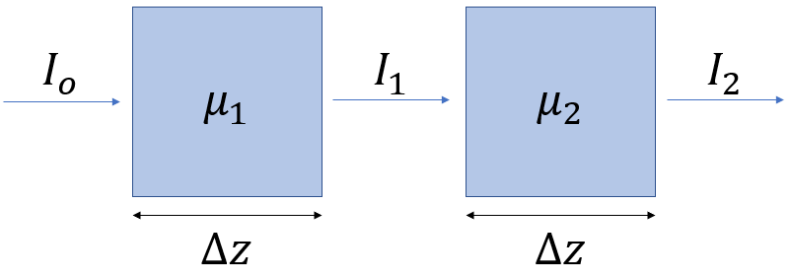

Figure 49: Light attenuation through successive finite volumes with varying dye concentrations, therefore varying attenuation coefficients.

Modeling this attenuation can be derived through integrating the Beer-Lambert law and solving for the light energy out of the volume. Consider the first volume, where an initial light energy, I_o, interacts with a volume element of a width Δz and an attenuation coefficient μ_1. The resulting light energy passing through the volume is indicated by I_1 and is determined by the following derivation.

$$\int_{I_o}^{I} \frac{dI}{I} = \int_{0}^{\Delta z} -\mu dz \tag{20}$$

$$I_1 = I_o \exp(-\mu \Delta z) \tag{21}$$

Notice this expression can be repeated for the next successive volume to determine the resulting light energy leaving the next volume. Another assumption regards the attenuation coefficient with the dye concentration within the cubic volume, where the two are assumed proportional to one another (i.e. $\mu \propto \phi$). However, the dye concentration is non-dimensional ranging from zero to one, therefore an amplification factor, γ, was used to represent a unit conversion to meters^{-1}. The value of the amplification factor was determined by comparing the generated projective image to the experimental image and matching the pixel intensity at the dye inlet, where the experimental image had pixel values of zero. Thus, the attenuation coefficient could be replaced with an amplification factor and dye concentration $\mu = \gamma\phi$. To implement equation (21) with the

CFD results, lines parallel to the z-axis were used to extract dye concentration along x- and y-coordinate points. The spacing between x and y coordinates was determined based on the pixel ratio recorded from the experiments.

5.3. Model Overviews

Three CFD models were created within SC/Tetra 2021, which included a laminar flow with dye in the center, a laminar flow with dye near the wall, and a turbulent flow with dye in the center. First model was the laminar case with dye injected in the center. This simulation geometry could be modeled with two symmetry planes thus requiring only a quarter of the model. Overall dimensions of the geometry were 50.8mm x 12.7mm x 12.7mm and a dye inlet diameter of 5.54mm. To insert PIV velocity profiles at the inlet, thirteen rectangular regions were created at the top of the domain. Additionally, twenty-two radial locations were created to control the width of the dye at the dye inlet. These regions can be viewed in Figure 51 along with the other regions of the model in Figure 50. Two of the four surfaces comprising the sides of the rectangle were identified as walls and the other two were classified as symmetry regions. The two symmetry regions allowed the simulation to model ¼ of the actual domain from the experiment. Lastly, the bottom surface of the model was declared as the outlet.

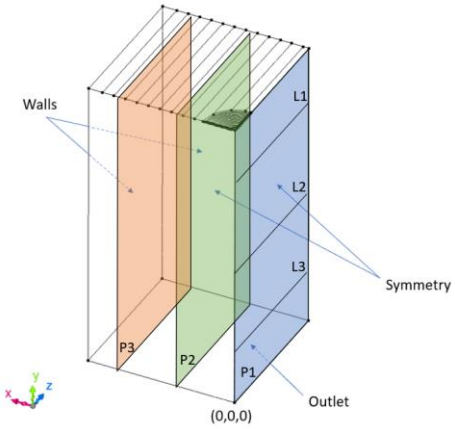

Figure 50: Geometric domain of the laminar CFD simulation for dye injected in the center with the wall, symmetry, and outlet regions identified.

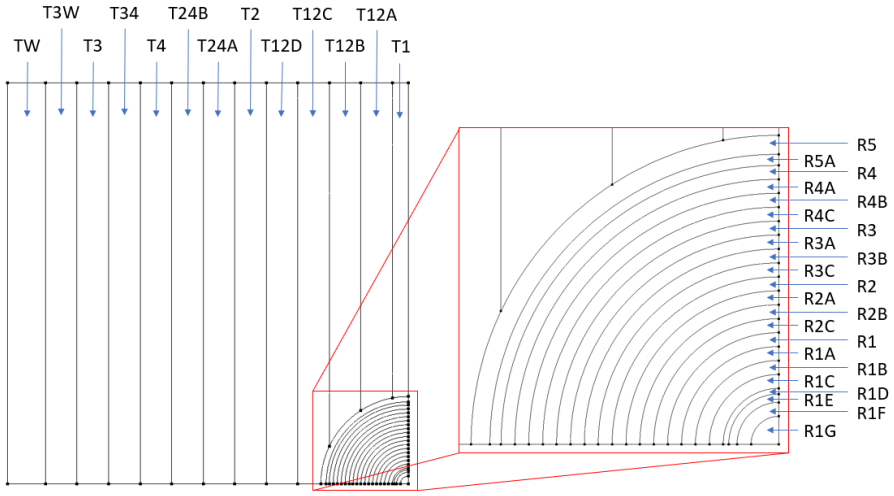

Figure 51: Detailed outline of the inlet regions for the water (T#) and dye (R#) associated with the laminar case with dye injected in the center.

The domain solely consisted of water, initially, with the density and viscosity of water set as 998.2 kg/m^3 and 1.016×10^{-3} Pa-s, respectively. Density of the dye was assumed equal to water and the diffusion coefficient was set at 1.0×10^{-9} m^2/s. Choice of the diffusion coefficient was based on another group who used a diffusion coefficient of 5.0×10^{-9} m^2/s, in the comparison

between CFD and experimental, because typical dye diffusion coefficient values range between 10^{-10} and 10^{-9} m^2/s [65].

For the laminar case with dye injected near the wall, the geometry was represented as a half model because the geometry was only symmetric about one plane. The dimensions of the model were 12.7mm deep, 25.4mm wide, and 50.8mm in length with a dye inlet diameter of 5.54mm. Quantities for the water and dye properties were the same as the values used in the dye injected in the center. Figure 52 provides the geometry and surface region names for the laminar case with dye injected near the wall.

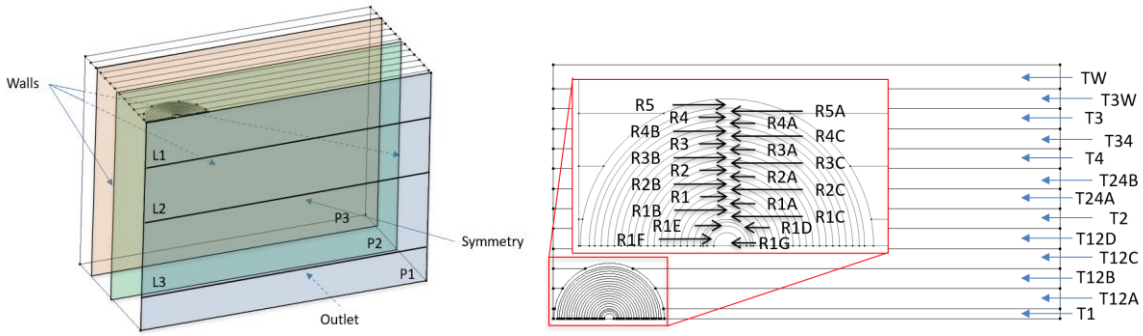

(a) (b)

Figure 52: (a) Geometry and surface region names for the laminar simulation with dye injected near the wall and (b) region names for the water and dye inlets.

There are three wall regions, one symmetry surface, and one outlet surface represented in Figure 52 (a). The highlighted planes denoted by P1, P2, and P3, are planes located at varying x-coordinates with three z-coordinate lines denoted as L1, L2, and L3, which will serve as comparisons for the mesh independence study and validation. Figure 52 (b) denotes the inlet regions for water (T#) and the dye inlet regions represented by R#. Several radial dye locations were used to control the width of the dye concentration through time.

Modeling for the turbulence case required the full domain due to the stochastic nature of instantaneous turbulent results which were necessary for dye projective images. The overall dimensions were 25.4mm x 25.4mm x 99.5mm and the dye tube had an outer diameter of 5.40mm and an inlet diameter of 3.40mm. The model incorporates four walls, an outlet, one inlet for the water, one inlet for the dye, and tube walls (Figure 53).

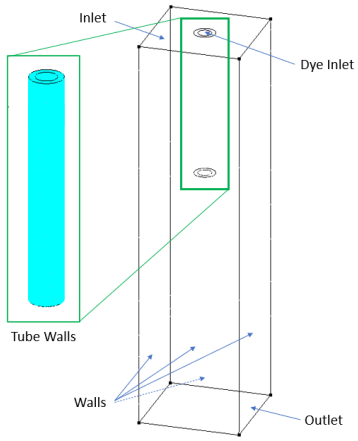

Figure 53: Geometry and region names for the turbulence model.

Notice there is a region between the inner and outer diameter of the dye tube which does not contain fluid because this region represents the thickness of the tube. This model also includes geometry upstream of the dye injection region, where the dye begins to diffuse in the water, to allow the dye flow to develop within the tube. This upstream region has a length of 37mm.

5.4. Boundary and Analysis Conditions

Boundary conditions for the laminar simulations can be broken down into three general categories: inlet, outlet, and walls. Four of the boundary faces were designated with wall conditions, but two of them had the no-slip condition and the other two had a free slip condition. The no-slip condition was applied to the surfaces identified as “Walls” whereas the free slip condition was applied to the regions identified as “Symmetry”, as shown in Figure 50 and Figure

52 for center and near wall models, respectively. No-slip condition ensures the velocity directly on the wall is equal to zero whereas the free slip region acts as a virtual wall and sets the velocity gradient at the wall equal to zero. The outlet boundary conditions were set as static pressure with a value of 0 Pa. In incompressible flows, pressure appears in the governing momentum equation solely as a pressure gradient. Therefore, the pressure difference is the only significance to the simulation. Thus, the pressure may become unstable if a fixed value is not established in the domain. It is general practice to indicate a fixed static pressure on the outlet boundary condition. Naturally, a value of 0 was provided since this pressure represents the reference pressure point. The inlet boundary condition accounts for the water inlet as well as the dye inlet. PIV measurements were used in establishing the inlet profiles from T1 to TW where user-defined functions were created for each of those regions. Since only four planes were measured with PIV, for both the center and near wall case, and the model domain contained thirteen, the regions outside of those four planes were determined through interpolation. Example of the user-defined velocity profile for the center injection at T1 is shown in the figure below. Note the coordinates are in terms of the z-direction which results in the velocity profile varying along the length of the rectangular regions shown in Figure 51.

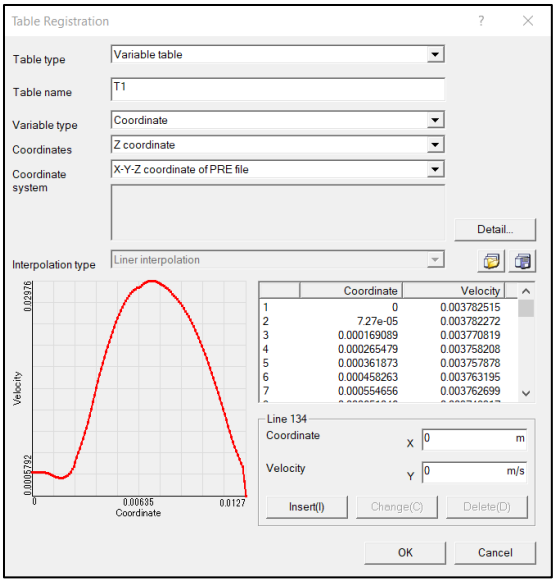

Figure 54: User-defined function for the velocity profile at T1 region for the laminar case of dye injected in the center.

For the dye inlet regions, a velocity for each radial section was held constant while the concentration of dye was varied with time. In the images obtained from the experiment, the diameter of the dye protruding from the inlet varied with time, therefore, to replicate this in the simulation a user-defined function was created for multiple radial locations. Below are examples of the transient user-defined functions for the center injection for dye concentration with respect to time in the regions R1F and R2A.

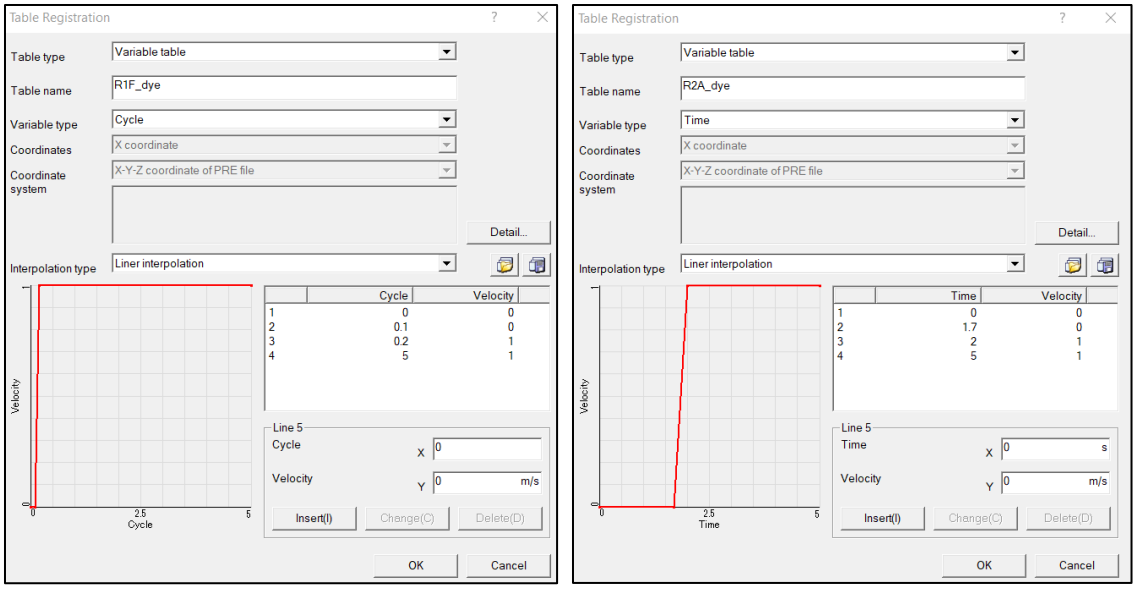

Figure 55: User defined functions for the dye concentration with respect to time for the regions R1F and R2A for the laminar case of dye injected in the center.

To setup the user-defined functions for the dye distribution, the diameter of the dye near the inlet was measured from multiple images acquired in the experimental portion of the research. Complete descriptions of the inlet velocity and concentration distributions for laminar flow with dye in the center are provided in Appendix A and for dye near the wall these descriptions are provided in Appendix B. The analysis was setup for a laminar flow where two simulations were conducted: 1) steady analysis and 2) transient analysis. The steady analysis was used to validate the velocity results with PIV and serve as the initial condition for the transient analysis. Transient analysis was used in validating the dye dispersion. For the transient analysis, the simulation had an initial time step of 0.0002 seconds, courant number was set at 0.8, and concluded at 4.5 seconds. Convergence criteria was set at 10^{-4} for the average threshold residuals of pressure, velocity, and concentration. In solving the governing equations, the convective terms were discretized with the MUSCL scheme, and the diffusive terms were solved with accuracy weighted. Reasoning for using MUSCL to solve the momentum and species convective terms are

a result of the dye simulation comparison of various convective schemes which will be discussed later. In solving the pressure-linked equations, the SIMPLEC method was used because of its convergence rate being 1.2 – 1.3 times faster than SIMPLE while maintaining the same cost per iteration as SIMPLE [66].

In conducting the turbulence simulation, the boundary conditions were set similar to the laminar models with regards to the wall conditions and the outlet condition. No-slip condition walls were applied to the square tube walls as well as the dye walls and the outlet was set as a static pressure of 0 Pascals. For the dye inlet, a constant velocity of 0.0125 m/s and constant dye concentration of 1.0 were used. Mass diffusivity of the dye was set to zero because when calculating the Peclet number, Pe, the quantity was $Pe \gg 1$ which means the diffusion phenomenon is dominated by convection, therefore insignificant. The Peclet number was calculated as $Pe = 7.7\text{E}6$. Constant velocity of 0.305 m/s was used for the water inlet with a dye concentration set to zero. Two analyses were conducted, similar to the laminar cases, where the first was a steady state simulation used for comparisons with PIV and the second was a transient state for simulating the dye propagation and diffusion. The steady state case used RANS with a standard k-ε turbulence model and the transient case used DES with the standard k-ε turbulence model. The use of RANS for the transient case would have resulted in unrealistic dye distributions due to the averaging nature of RANS, therefore DES was used to provide more realistic simulations. The steady state simulation used a convergence criterion of 1E-4 for the average residual associated with all variables except V-velocity which used an average residual of 5E-5. Analysis conditions for the transient simulation used an initial time step of 1E-5 seconds and a Courant number of 0.9.

5.5. Mesh Independence Study

Throughout the years of researchers investigating various phenomena in CFD simulations, there is one practice which is critical for accurate simulations and that is mesh independence. This standard practice provides a method for ensuring results do not dependent on the mesh size but rather a direct effect of the boundary and analysis conditions. Furthermore, this allows researchers to determine the optimal mesh size for computational cost without losing accuracy of the simulation. Mesh independence was conducted with four different mesh sizes where velocity profiles were compared at three positions on three different planes. Therefore, a total of nine profiles were compared with each of the meshes. The three profiles on each plane were extracted 5 mm, 15 mm, and 35 mm downstream of the inlet. These profiles were extracted from planes located at 0 mm, 5 mm, and 10 mm from the symmetry boundary. Below are the four different meshes with Mesh 7c being the coarsest mesh with about 150,000 elements and Mesh 10c being the finest mesh with over 21 million elements.

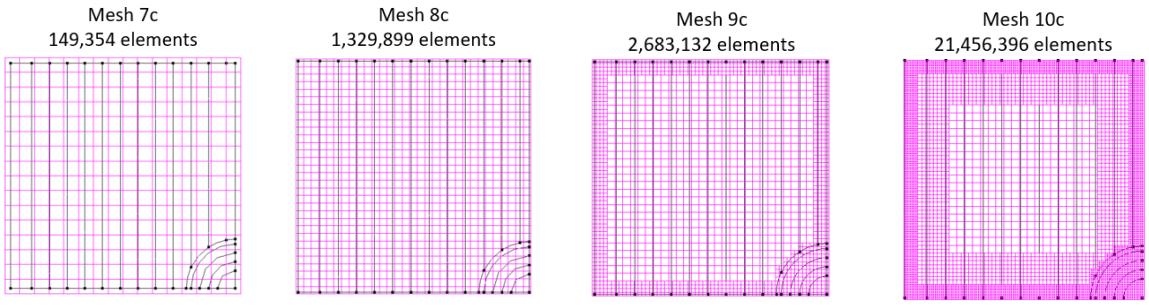

Figure 56: Various mesh sizes used to test mesh independence.

Percent differences were calculated for each of the meshes in comparison to Mesh 10c, to see if any of the coarser meshes performed similarly to the finest mesh. Table 4 summarizes the percent differences at each extracted profile in comparison with Mesh 10c.

Table 4: Percent difference of the y-component velocity at various line extractions between Mesh 10c and the remaining coarse meshes.

	Plane at 0 mm			Plane at 5 mm			Plane at 10 mm		
	5 mm	15 mm	35 mm	5 mm	15 mm	35 mm	5 mm	15 mm	35 mm
Mesh 7c	5.7%	4.6%	5.7%	2.3%	1.4%	1.7%	7.9%	5.4%	4.0%
Mesh 8c	1.6%	1.0%	1.4%	0.3%	0.2%	0.2%	0.7%	0.5%	0.4%
Mesh 9c	0.5%	0.4%	1.0%	0.5%	0.3%	0.3%	1.8%	1.3%	1.2%

The error associated with Mesh 7c has a maximum value of 7.9% while Mesh 8c has a maximum error of 1.6%, which is below the 5% threshold. Mesh 9c also has a maximum error less than 5%, however Mesh 8c is a coarser mesh which saves memory and computational costs, hence Mesh 8c will be used for further simulations.

Additional simulations were conducted to determine which convective scheme produced the least amount of numerical diffusion with regards to dye concentration. For these simulations a cylindrical model with a height of one inch and diameter of one inch was used. This allowed for relatively quick simulations to determine the meshing size as well as the optimal convective scheme. To solely observe numerical diffusion caused by the convective scheme, the diffusion coefficient in the species equation was set equal to zero. The analysis conditions of the steady-state simulation involved downward velocity at a rate of 0.04 m/s at the inlet (top), static pressure of zero at the outlet (bottom), no-slip condition on the cylinder side wall, and dye was injected into the domain at a rate of 0.01 m/s with a concentration of unity (top). In the first mesh, the finest octant level had a size of 6.945×10^{-5} meters, which was in the middle of the domain where the dye inlet was located, and a total of 23 million elements (Figure 57).

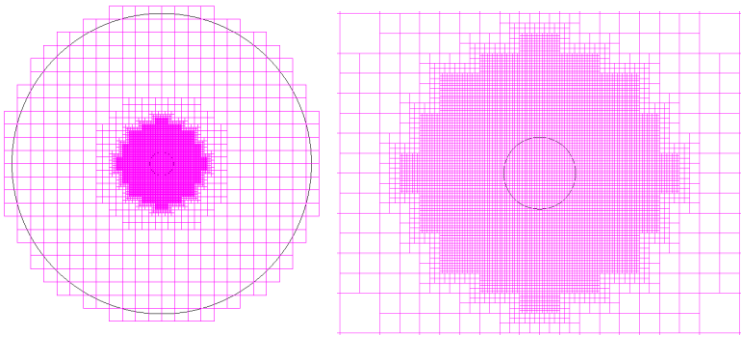

Figure 57: Octant level distribution for Mesh 1 (left) and an enlarged view of Mesh 1 located at the dye inlet region (right).

Three convective schemes were used for this comparison which included the upwind, SMART, and MUSCL. Upwind method is first order while the SMART and MUSCL schemes are considered second order accurate. Below are contour plots of the dye concentration for each scheme located at the center of the domain.

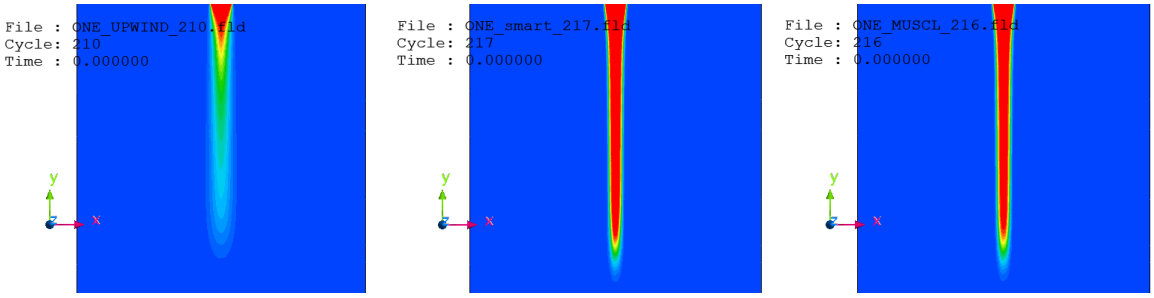

Figure 58: Dye concentration contour plots for the Upwind (left), SMART (center), and MUSCL (right) convective schemes with diffusion coefficient set to zero.

From a qualitative observation, the upwind scheme introduces a large amount of numerical diffusion compared to SMART and MUSCL. This is expected since upwind is first order, therefore it requires finer mesh to accomplish more accurate simulations. In comparing MUSCL and SMART, the two schemes appear to produce similar results. Both schemes were not able to achieve full propagation of the dye through the entire domain for this mesh. To provide a

quantitative comparison, dye concentration values extracted along the center of the domain were plotted for each of the schemes.

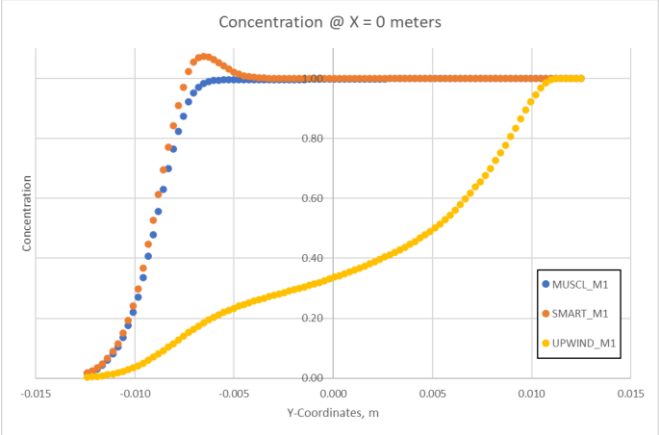

Figure 59: Dye concentration values from upwind, SMART, and MUSCL, which were extracted along the centerline.

Figure 59 demonstrates the rapid decrease in concentration by the upwind scheme as the dye propagates downstream from 0.0127 meters to -0.0127 meters. More importantly, this comparison provides insight into the SMART and MUSCL schemes with regard to how they react to steep gradients. Both schemes exhibit a similar profile from -0.0127 meters to about -0.008 meters, but around -0.007 meters the SMART scheme reveals some numerical oscillations which results in a concentration value above unity. This result does not make physical sense seeing that a concentration of unity is the maximum. For MUSCL, the scheme is able to handle the steep gradient well and preserve the discontinuity without exceeding unity. For this reasoning, the MUSCL scheme was selected for analyzing the convective terms in the species equation. Since neither MUSCL nor SMART were capable of propagating the dye throughout the entire domain, a second mesh was constructed where the finest octant size was 3.473×10^{-5} meters with a total of 22 million elements. This mesh focused on the region directly next to the dye inlet to save on computational costs (Figure 60).

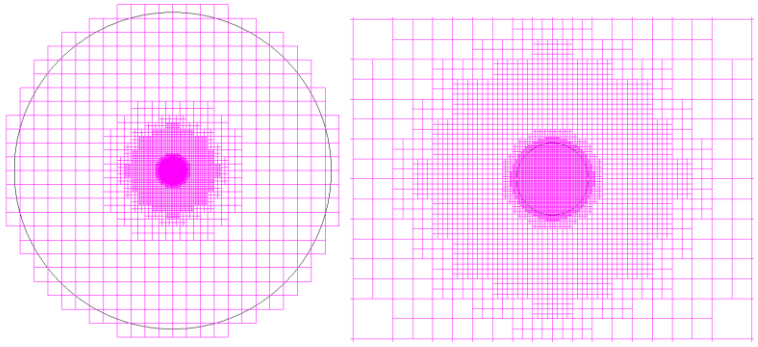

Figure 60: Octant level distribution for Mesh 2 (left) and an enlarged view of Mesh 2 located at the dye inlet region (right).

Another simulation was conducted with Mesh 2 but only with the MUSCL scheme to verify the mesh was fine enough for full propagation of the dye concentration. In Figure 61, the contour of the dye concentration for Mesh 2 is displayed alongside the variation in concentration along the centerline of the domain.

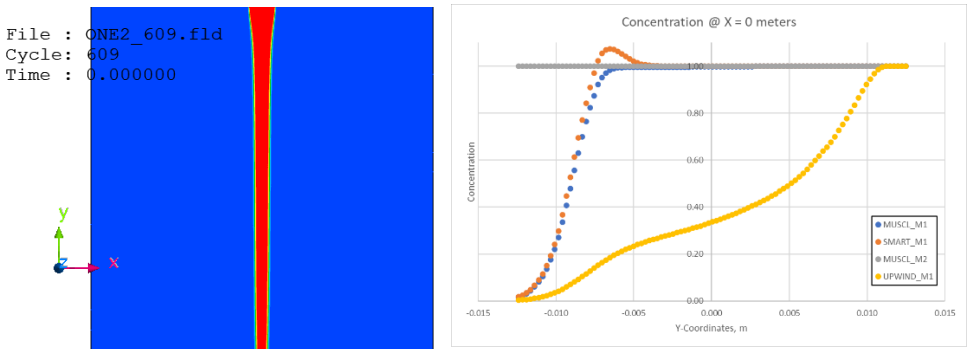

Figure 61: Contour plot of the dye concentration for the MUSCL scheme in Mesh 2 (left) and the concentration profile among the Mesh 1 schemes (right).

The contour plot illustrates the dye concentration is able to travel through the entire domain with Mesh 2 and the concentration profile verifies the concentration never exceeds unity and is constant throughout the y-coordinates. This provides evidence the mesh requires an octant level of 3.473×10^{-5} meters or finer to mitigate numerical diffusion from the convective terms.

Using the results from the velocity mesh independence study and the convective scheme study, a new mesh was created which incorporated octant levels used in both studies. The octant level near the walls and the middle of the domain are represented by Mesh 8c while the octant level near the dye inlet is represented by Mesh 2. This mesh contained a total of 16.9 million elements with three prism layers of insertion at the physical walls.

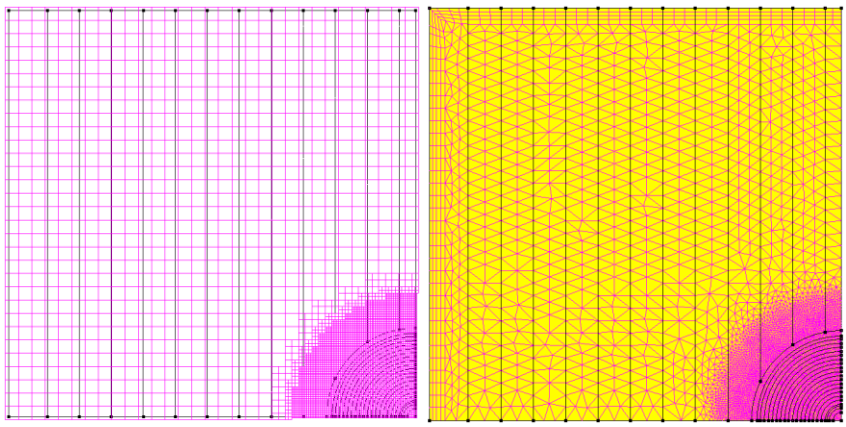

Figure 62: Final octant distribution (left) and final generated mesh with prism layer insertion (right) for the laminar case with dye injected in the center.

Mesh independence study for the laminar case with dye injected near the wall was also conducted, which involved three different unstructured meshes generated with Cradle SC/Tetra 2021. Further details regarding the meshes are found in Table 5, which shows comparisons of the coarser meshes (1 & 2) with the finest mesh (3). The regions of interest are identified with a plane (P1, P2, or P3) and a line along that plane (L1, L2, or L3) as depicted in Figure 52. P1 was located at the center plane, P2 was 5mm from P1, and P3 was 10mm from P1. Each of these planes had three lines extracted from them where L1 was 5mm downstream of the inlet, L2 was 15mm, and L3 was 35mm.

Table 5: Mesh independence study for the laminar case with dye injected near the wall.

Half Model - Dye Near Wall											
Mesh	Min. Elem	Total Elements	P1L1 Error	P1L2 Error	P1L3 Error	P2L1 Error	P2L2 Error	P2L3 Error	P3L1 Error	P3L2 Error	P3L3 Error
1	1.06E-4	10,132,326	7.4%	3.5%	6.2%	8.7%	6.8%	4.1%	3.8%	7.6%	7.9%
2	6.95E-5	17,420,830	0.5%	0.5%	1.0%	0.3%	0.3%	0.4%	1.6%	1.4%	0.8%
3	6.95E-5	20,710,389	N/A	N/A	N/A	N/A	N/A	N/A	N/A	N/A	N/A

These results identify Mesh 1 as too coarse of a mesh since the error associated with P1L1, P1L3, P2L1, P2L2, P3L2, and P3L3 all have error greater than 5% with the maximum difference, 8.7%, occurring at P2L1. Mesh 2 was able to sustain error lower than 2% for all regions of interest with the highest error being 1.6% located at P3L1, thus mesh 2 was selected for further analysis.

The turbulence model had three different meshes generated for conducting mesh independence, however these meshes incorporated structured as well as unstructured mesh since numerical diffusion is more prevalent when flow direction is not parallel with the cell walls [67]. Therefore, structured mesh was implemented near the dye inlet as well as downstream of the inlet to mitigate numerical diffusion from affecting the dye concentration. The figure below illustrates the surface elements looking from the top view (left) and the interior elements when the domain is sliced in the middle (right).

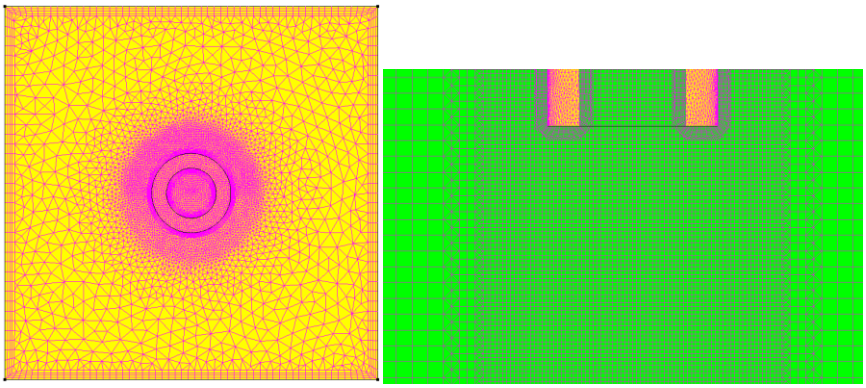

(a)

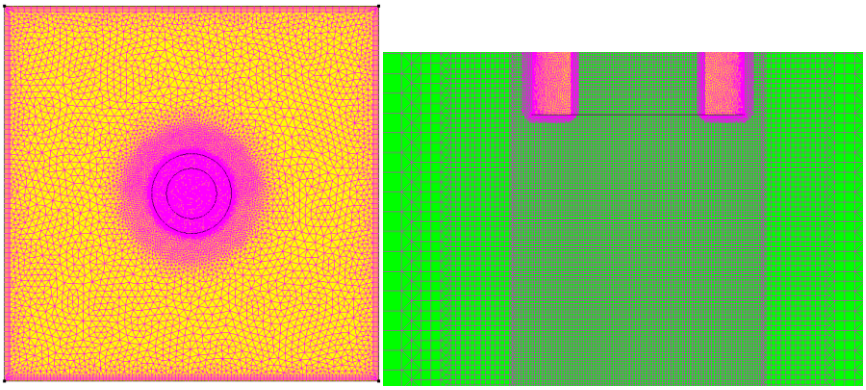

(b)

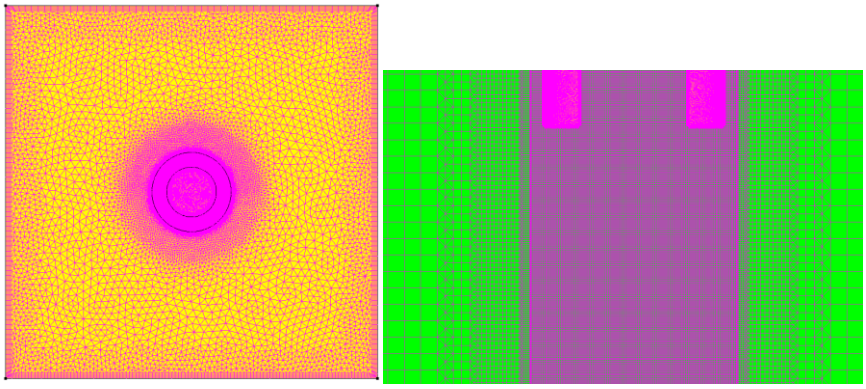

Figure 63: Turbulent mesh element comparison from the top view (left) and interior elements sliced in the center (right) between (a) mesh 1, (b) mesh 2, and (c) mesh 3.

Notice the mesh refinement focused primarily on the center where the dye inlet was located, since this region involved sudden change in geometry as well as an interaction between slower dye velocity and higher water velocity. Each of these meshes were compared with respect to v-velocities located at the center plane (z = 0.127m) at three x-coordinate locations downstream of the dye inlet (-16mm, 5mm, and 25mm) featured in Figure 64.

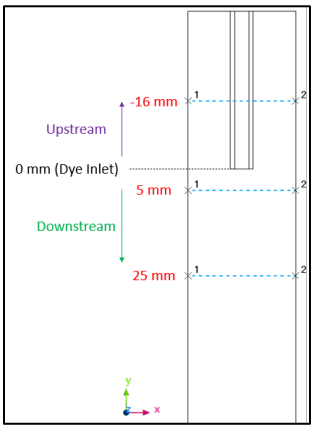

Figure 64: Regions identified for mesh comparisons for the turbulent case.

Average error was calculated for each of these regions and tabulated in the table below, and additional information regarding the mesh including the total elements are listed.

Table 6: Turbulence model mesh independence study with mesh information and average error.

Turbulence Model - Dye in Center						
Mesh	Min.	Total	Prism	-16mm	5mm	25mm
1	1.25E-4	7,881,799	9	2.5%	1.8%	0.9%
2	6.25E-5	30,950,642	12	0.2%	1.5%	0.3%
3	3.13E-5	54,129,125	22	N/A	N/A	N/A

Initially, mesh 1 appears to have insignificant differences since each of the average values are below 5%. However, when the velocity contours are investigated further the differences become more apparent especially near the squared tube wall and directly downstream of the dye inlet.

Velocity contours and velocity profiles at -16mm and 5mm are displayed in Figure 65 and Figure 66, respectively.

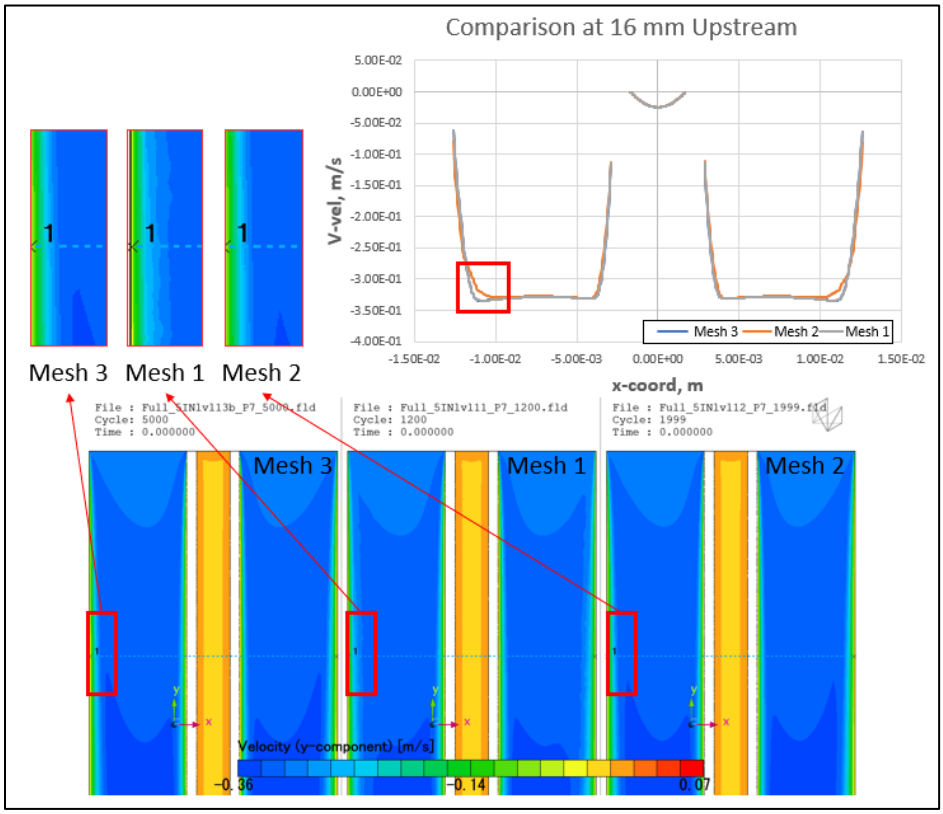

Figure 65: Detailed comparison of the v-velocity among the different turbulent meshes at 16mm upstream of the dye inlet.

The v-velocity profile at 16mm upstream reveals noticeable differences near the squared tube wall as shown in the line plot. This can be viewed qualitatively in the contour plot where the region near the wall has been enlarged to view the differences. Additionally, the contour plot uncovers more differences slightly downstream of -16mm between mesh 1 and mesh 3, where mesh 2 and mesh 3 have similar contours. Further comparison around 5mm downstream of the dye inlet, indicate contour differences between mesh 1 and mesh 3, which are enclosed in the red

circles shown in the figure below. The line plot does not capture this region therefore the average error from the table appears minimal for mesh 1.

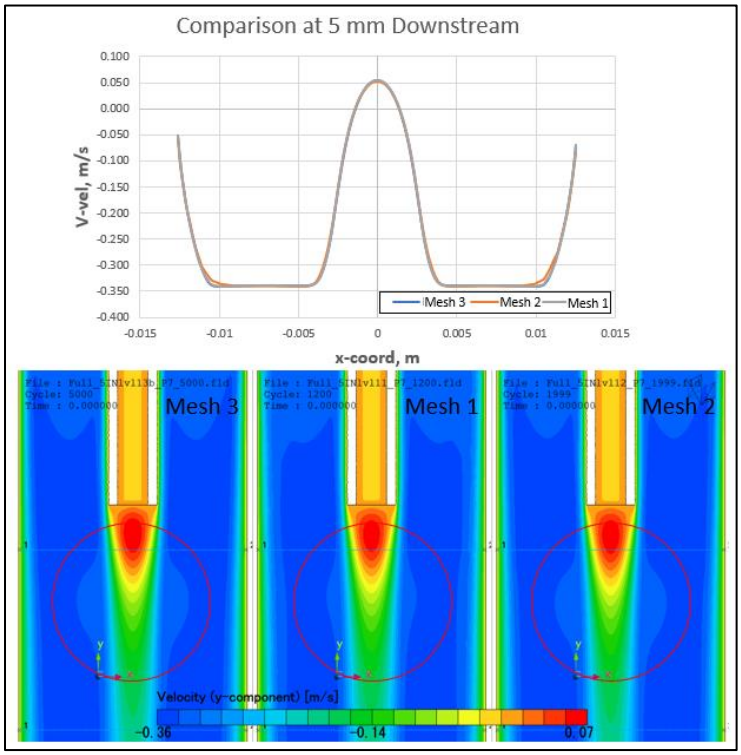

Figure 66: Detailed comparison of the v-velocity among the different turbulent meshes at 5mm downstream of the dye inlet.

By investigating the three meshes further, the coarse mesh 1 would not represent a mesh independence from the solution therefore mesh 2 was selected for further analysis as it maintains mesh independence with fewer elements than mesh 3.

5.6. Validation with Experimental Results in Laminar Flows

In confirming accuracy of the CFD results, experimental results such as the velocity, dye head location, and dye pattern were compared. Laminar PIV measurements were directly compared with the laminar CFD results at the center plane (0 mm), the plane 5 mm from the center, and 10 mm from the center. These planes are shown and denoted as P1, P2, and P3, respectively in Figure 50 and Figure 52. For each plane, three lines (perpendicular to the bulk fluid motion) at

locations of 5 mm (L1), 15 mm (L2), and 35 mm (L3) downstream of the inlet were extracted for the dye in the center and dye near the wall. Below are laminar PIV and CFD comparisons for the dye injected in the center of the domain for P1, P2, and P3.

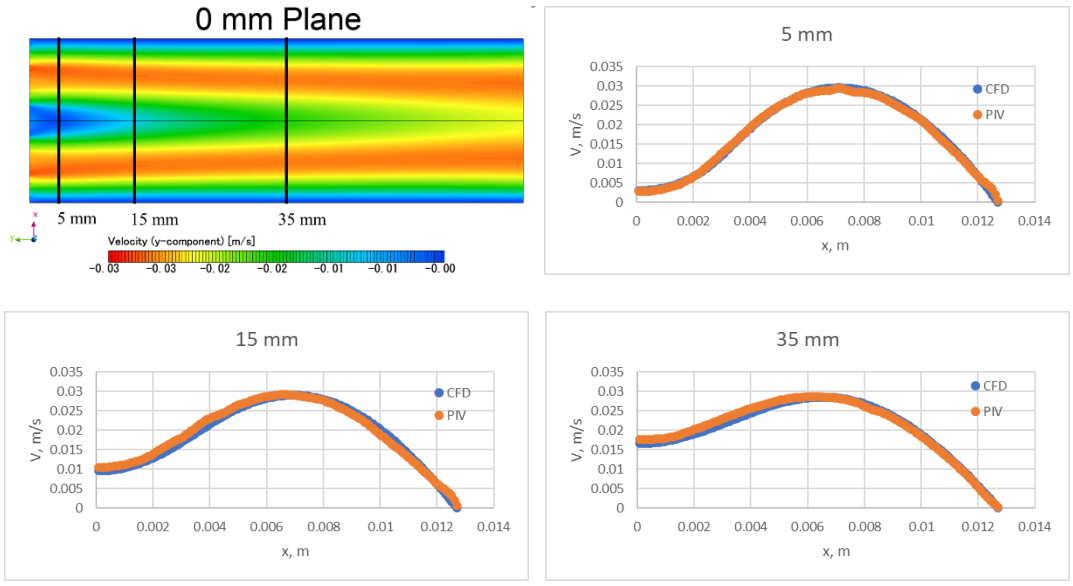

Figure 67: Laminar flow: CFD contour plot of y-component velocity (top-left) and velocity comparisons between CFD and PIV for 0 mm plane at 5 mm (top-right), 15 mm (bottom-left), and 35 mm (bottom-right) for dye in the center.

The average error for the 5 mm, 15 mm, and 35 mm locations were 3.3%, 4.8%, and 3.5%, respectively. Each of the locations yielded an average error less than 5% therefore the center plane was confirmed. Next plane was located 5 mm from the center plane with the velocity extracted from the same locations downstream.

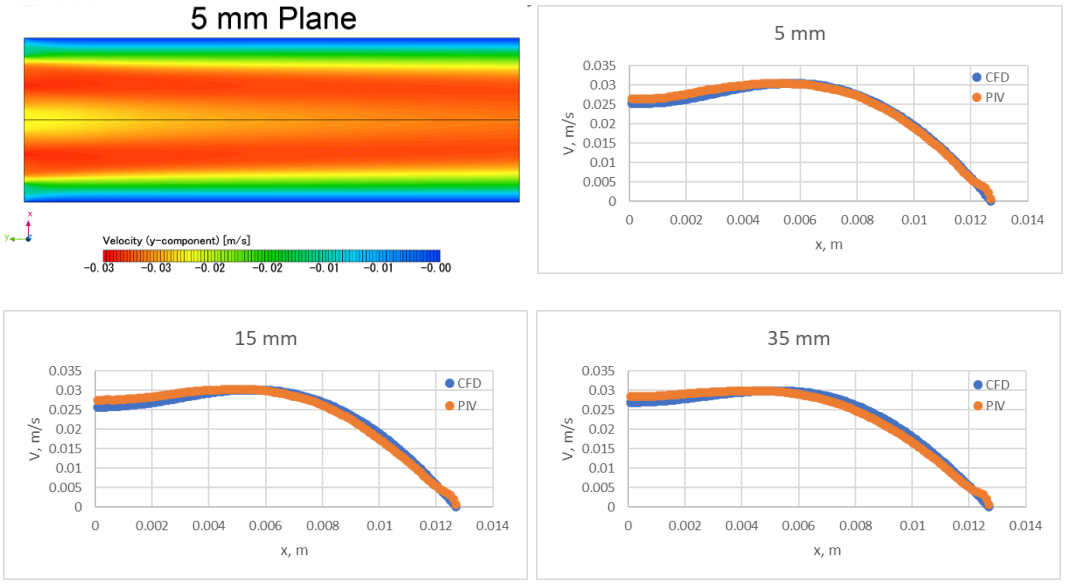

Figure 68: Laminar flow: CFD contour plot of y-component velocity (top-left) and velocity comparisons between CFD and PIV for 5 mm plane at 5 mm (top-right), 15 mm (bottom-left), and 35 mm (bottom-right) for dye in the center.

Average error for the 5 mm, 15 mm, and 35 mm locations were 3.8%, 4.7%, and 4.8%, respectively. Each of the errors were below 5%, thus the 5 mm plane was verified. Last plane was located 10 mm away from the center plane and the locations being evaluated were the same for the previous planes.

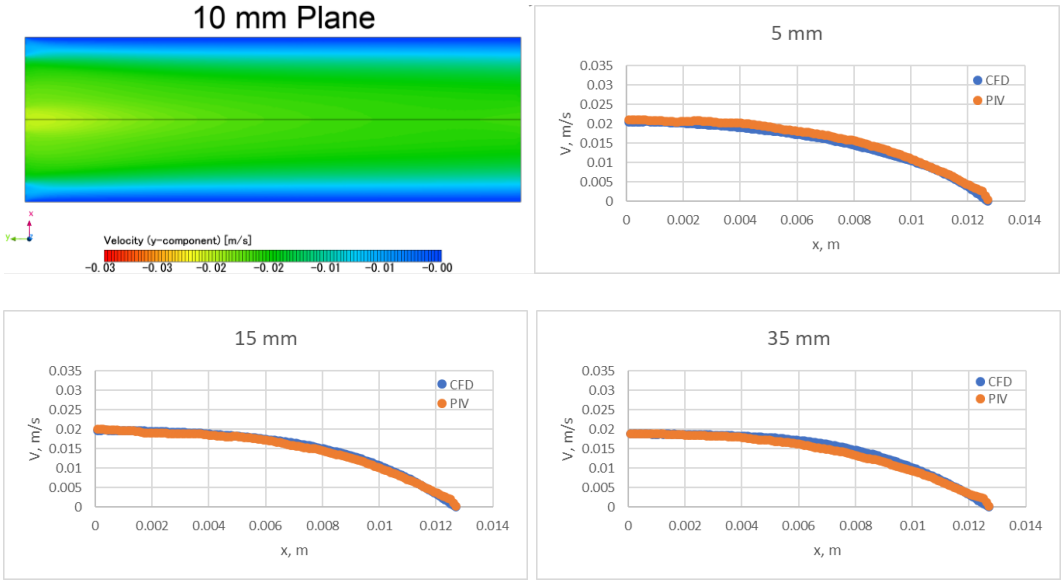

Figure 69: Laminar flow: CFD contour plot of y-component velocity (top-left) and velocity comparisons between CFD and PIV for 10 mm plane at 5 mm (top-right), 15 mm (bottom-left), and 35 mm (bottom-right) for dye in the center.

From a qualitative comparison, the CFD results show a similar pattern in the velocity profiles as the laminar PIV results. When calculating the percent error for each location, the average error at 5 mm and 35 mm were both 4.9%. For the 15 mm location, the average error was 3.5%. Therefore, all of the locations for each plane contained an average error less than 5%, which provides a strong argument in validating the velocity results of the CFD simulation.

Comparisons between the laminar PIV and CFD were also made for the dye near the wall to validate the CFD model. These comparisons are displayed in the figures below for planes P1, P2, and P3.

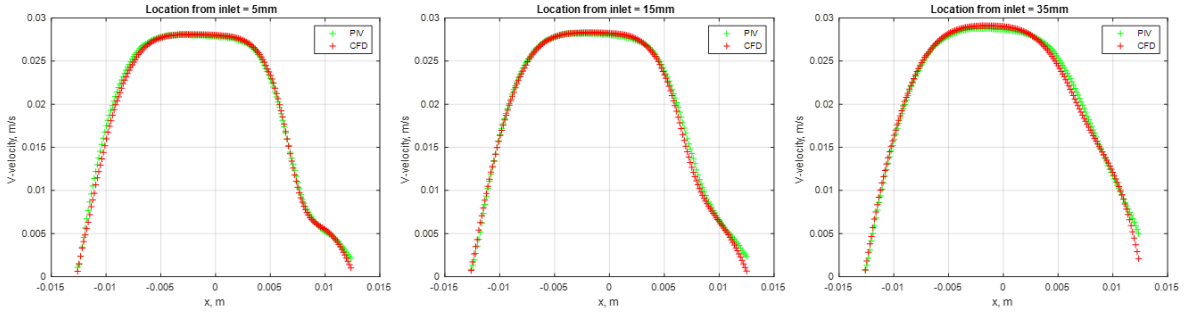

(a)

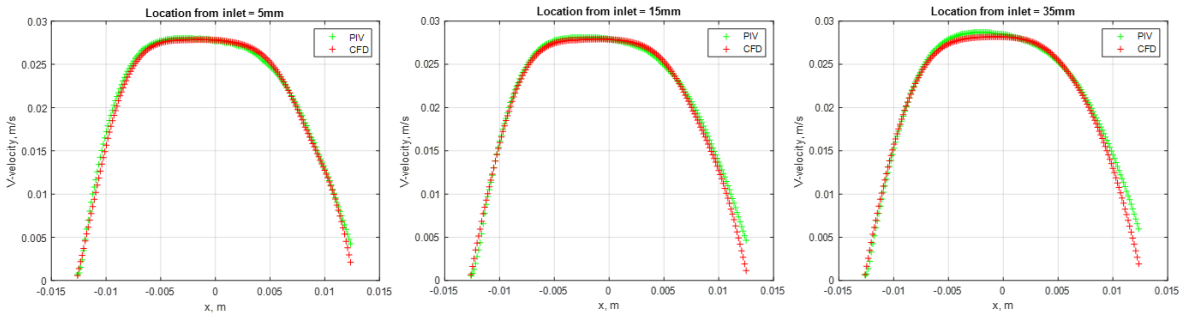

(b)

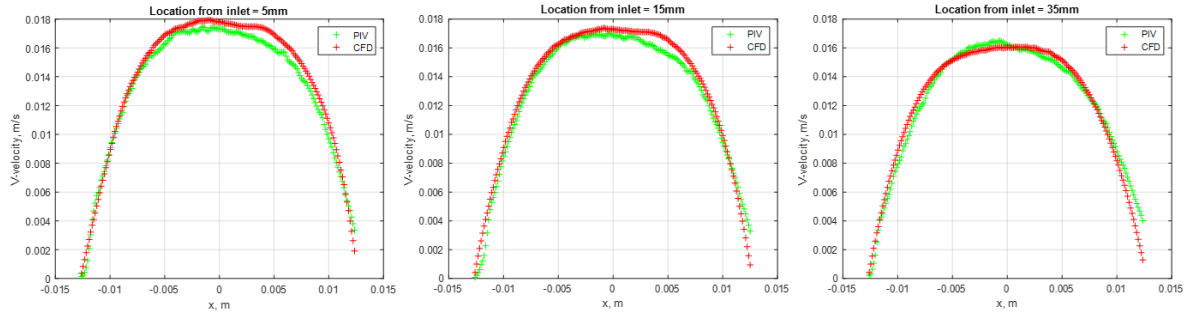

(c)

Figure 70: Laminar flow: PIV and CFD comparisons for the dye near the wall for planes (a) P1 - center, (b) P2 - 5mm, and (c) P3 - 10mm.

The error associated with plane P1 – center is 2.7%, 2.5%, and 2.2% with respect to lines 5mm, 15mm, and 35mm from the inlet. These average errors are below 5% and the velocity profiles match well with PIV especially between 0.005 and 0.01m, which are located near the dye inlet region. P2 – 5mm comparisons match well with PIV as well with average errors of 2.4% for 5mm, 2.6% for 15mm, and 3.1% for 35mm from the inlet. When the flow is closer to the wall, the laminar PIV measurements have more fluctuation to them as seen in the velocity profiles in Figure 70 (c) between x = -0.005m and 0.005m. The average error at 5mm from the inlet is 4.9%, which is just under 5% but there are some noticeable differences near the x = 0.004m. For

15mm from the inlet, the average error is 4.6% with differences occurring near x = 0.004m again. However, the velocity profile at 35mm shares more similarities with PIV but does underestimate values near x = -0.003m thus leading to an average error of 4.7%.

To compare the dye head location of the experimental images to the CFD results, the CFD concentration values were extracted in 3D-resolution and then a projective image was created by simulating light passing through the domain. This process was explained in detail in the generated projective image section. Once the images were generated, a program in MATLAB was then created to read in image files from the experiment to identify the dye head location based on a critical pixel intensity value. This intensity value was also used in determining where the dye head location was in the CFD results. The following graph compares the CFD results to the experimental results.

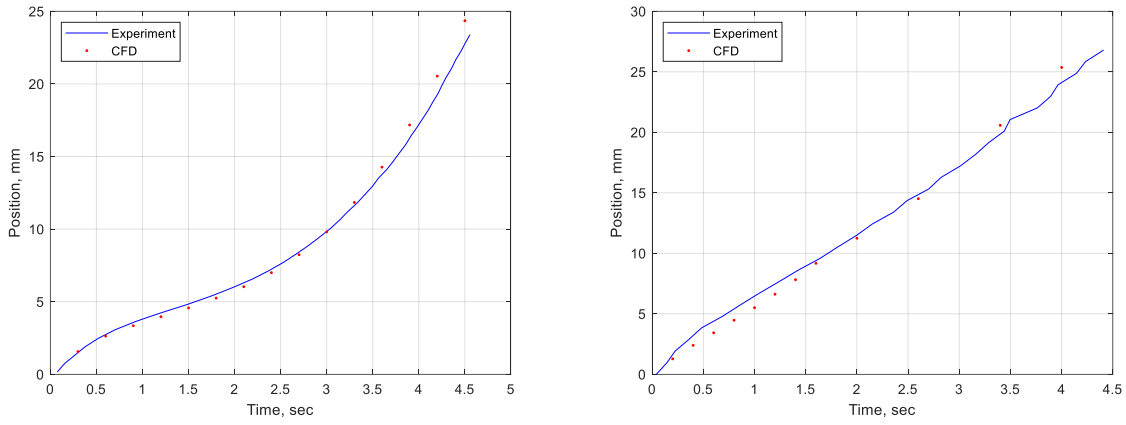

(a) (b)

Figure 71: Laminar flow: comparison between the experimental results and CFD results for the dye head location in the (a) center and (b) near the wall.

The error associated with each time point was calculated and tabulated in Table 7. The absolute difference is presented underneath the percent difference for reference especially near the smaller position values.

Table 7: Absolute error of the dye head displacement between experimental and CFD results for dye in the center.

Time, s	0.3	0.6	0.9	1.2	1.5	1.8	2.1	2.4	2.7	3.0	3.3	3.9
Absolute Error, mm	0.1	0.15	0.23	0.27	0.27	0.28	0.25	0.24	0.16	0.01	0.24	0.9

The absolute error indicates the CFD results represent the experimental data well with the highest error being 1.62mm which occurred at 4.5 seconds. However, the absolute error does not exceed 1mm up to 3.9 seconds of the simulation. In the table below the absolute error associated with the dye injected near the wall is displayed.

Table 8: Absolute error of the dye head displacement between experimental and CFD results for dye near the wall.

Time, s	0.2	0.4	0.6	0.8	1.0	1.2	1.4	1.6	2	2.6	3.4	4
Absolute Error, mm	0.1	0.15	0.23	0.27	0.27	0.28	0.25	0.24	0.16	0.01	0.24	0.46

The error for the dye near the wall simulation consistently models the dye head location within 1mm of the experimental values. The largest error occurs at 4 seconds with 0.46mm of difference which results in a percent error of 1.8%. Overall, the dye head displacement results between CFD and the experiment match well with one another. Last item to compare was the dye distribution pattern which requires a comparison between the experimental image with the generated CFD projected image. In Figure 72, side-by-side comparisons between the

experimental image, positioned on the left side, and the projected image created by the CFD results, positioned on the right, are presented.

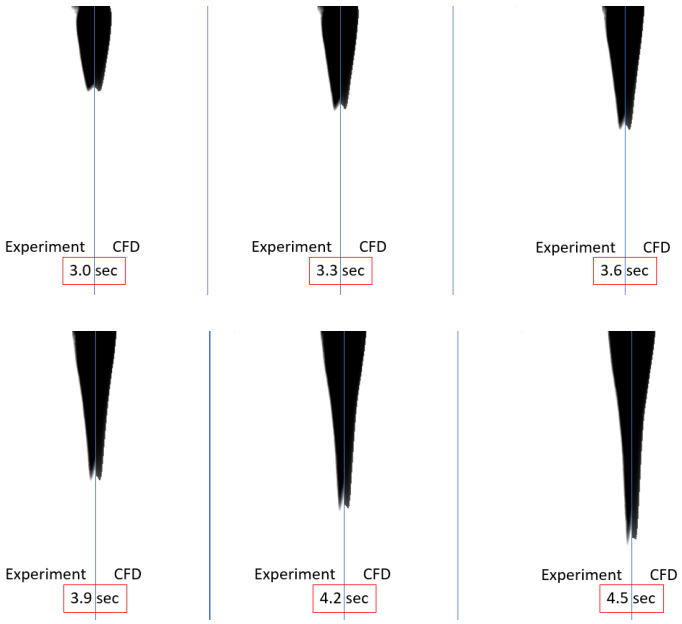

Figure 72: Laminar flow: side-by-side image comparison between experimental and CFD results for various points in time with dye in the center.

By viewing the images side-by-side, the diameter of the dye inlet produced by CFD is comparable to the diameter of the experiment and the overall dye pattern is nearly identical from 0.3 seconds to 2.4 seconds. After 2.4 seconds the dye pattern from the CFD tends to travel downstream slightly faster, but this is expected based on the results summarized in Table 7. Around 3.9 seconds the distribution of the dye in the middle of the plane for the CFD results exhibits more of a uniform pattern as opposed to a tapered pattern as illustrated by the experimental image.

Dye patterning comparisons between experimental and CFD for the dye near the wall were qualitatively compared in the figure below for times between 0.4 seconds and 3.4 seconds. At 0.4 seconds, the dye propagation is small, and the head locations are similar to one another. By 1.4 seconds, the dye has propagated further with some slight differences between CFD and experimental, such as the CFD dye starting to travel towards the center more than the

experimental image. As time progresses, the dye head location of CFD tends to lag behind the experimental until 3.4 seconds. Within the 2.6 second time frame, the CFD dye begins to straighten out as opposed to drifting toward the center, which follows a similar pattern to the experimental images. Overall, the comparisons between CFD and experimental images are in good agreement with one another.

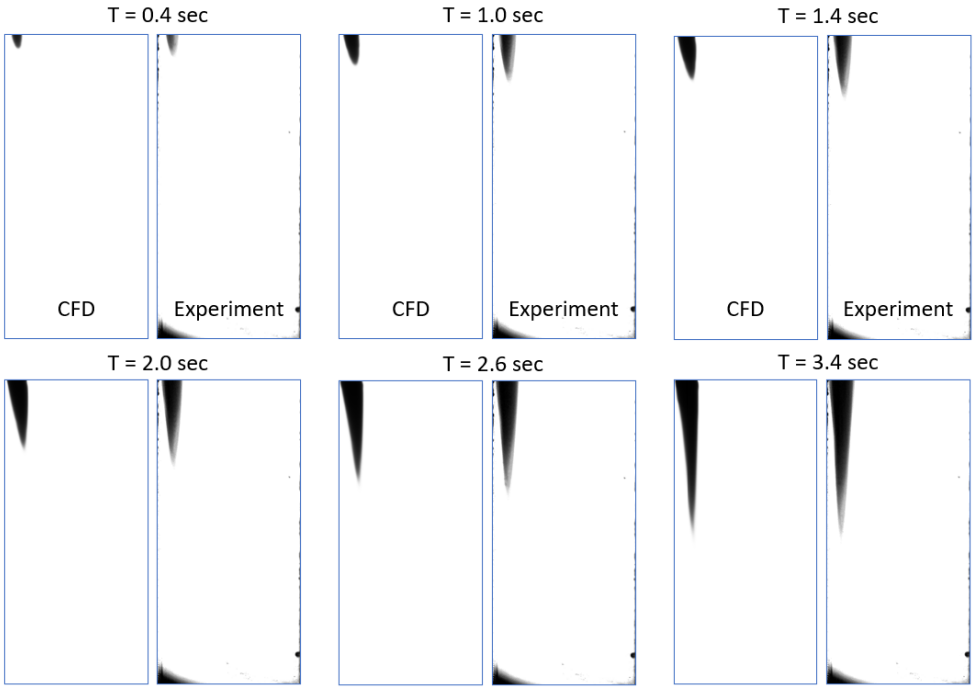

Figure 73: Laminar flow: side-by-side image comparison between experimental and CFD results for various points in time with dye near the wall.

5.1. Validation with Experimental Results in Turbulent Flows

Validating the turbulent CFD model incorporated the comparison of v-velocity profiles along various lines extracted from multiple planes (center, 5mm, and 10mm) from the steady state simulation. First comparison was made at the center plane, or 0mm plane, along y-locations downstream of the dye injection point with respect to the turbulent PIV results.

Downstream distance, mm	Difference, %
5	8.0
10	6.0
15	3.2
20	3.4
25	3.9
30	3.0
35	3.0
40	3.7

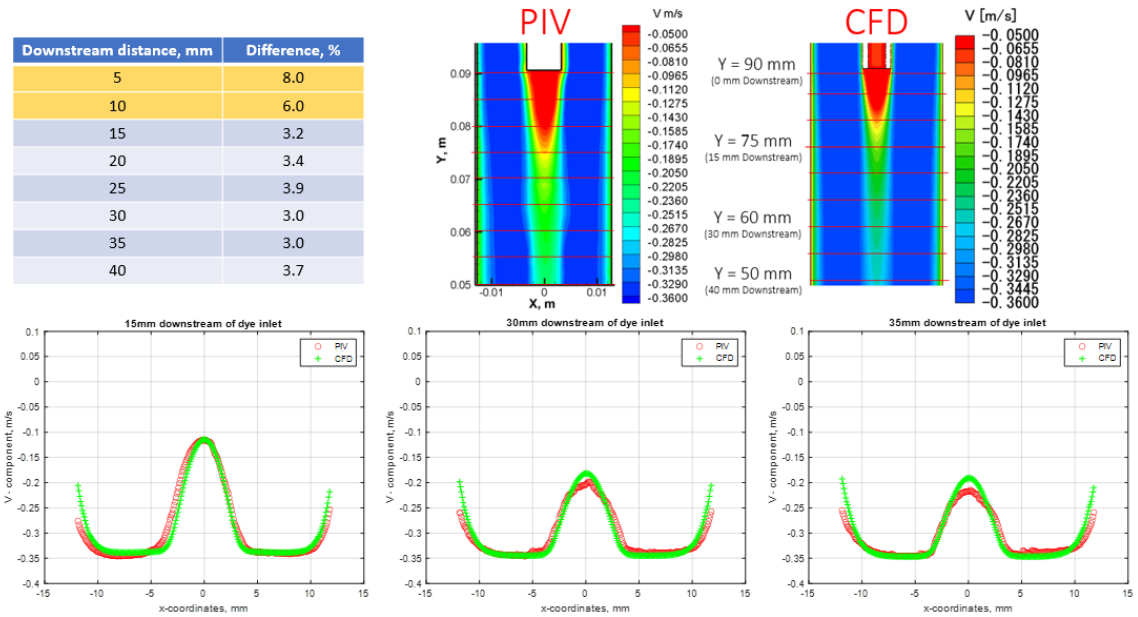

Figure 74: Turbulent flow: PIV and CFD comparisons of v-velocity at center plane for various y-locations.

Notice the difference at 5mm and 10mm are both above 5%, and the reason is because the turbulent PIV results at this point were not accurate due to the lower speed region in comparison with the high flow region outside of the center. The velocity profiles at 15mm and 30mm downstream of the dye inlet show good resemblance with the turbulent PIV data, however at x = 0mm the difference is noticeable for 30mm downstream. For 35mm downstream, the center point continues to display differences between PIV and CFD, however the average difference is 3.0%. Comparisons at the 5mm plane are shown below which consist of velocity contours as well as velocity profiles extracted from y-locations downstream of the dye injection.

Downstream distance, mm	Difference, %
5	3.6
10	3.5
15	2.7
20	2.0
25	2.3
30	2.9
35	3.4
40	3.9

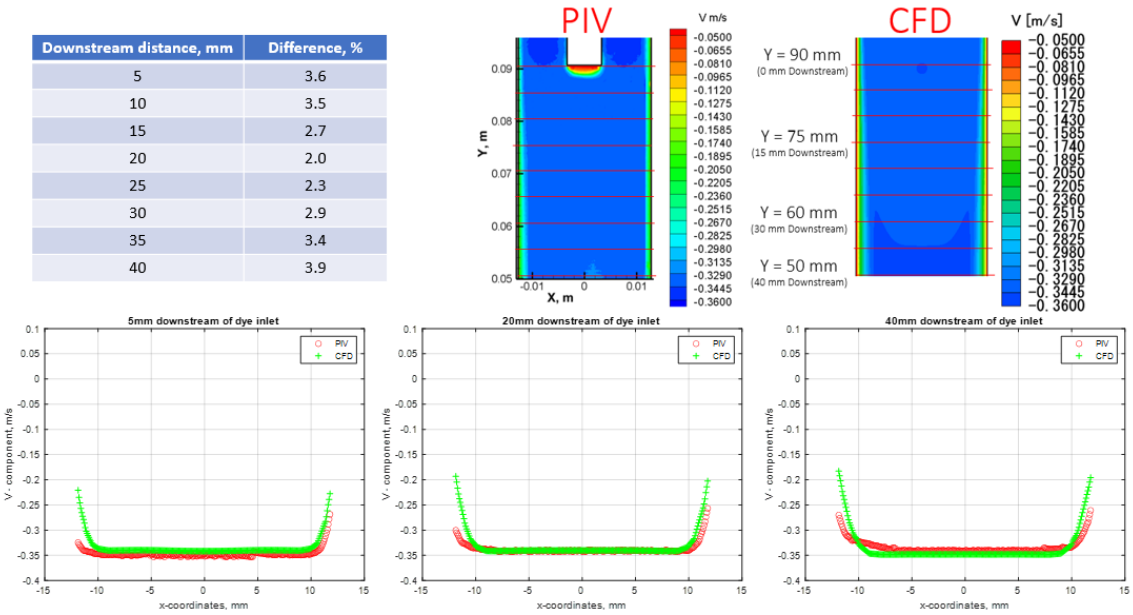

Figure 75: Turbulent flow: PIV and CFD comparisons of v-velocity at 5mm plane for various y-locations.

The velocity contours illustrate similar patterning between 5mm and 25mm downstream, but at 30mm the CFD simulation displays larger velocities near the wall and becomes uniform at 35mm. Looking at the velocity profile comparisons at 5mm downstream, the CFD measurements underestimate with respect to turbulent PIV measurements near the middle of the domain. Near the wall, the CFD profile trends toward zero whereas the turbulent PIV velocities do not which is common due to the spatial resolution of PIV. The CFD results compare the best with PIV at 20mm downstream with an average difference of 2.0%, however the average difference increases to 3.9% at 40mm downstream. The increase in contrast is a result of the CFD quantities near the middle of the domain slightly overestimating the turbulent PIV measurements. Lastly, the plane located 10mm from the plane was compared with the turbulent PIV measurements and the results are shown below in Figure 76.

Downstream distance, mm	Difference, %
5	3.9
10	3.4
15	2.8
20	2.5
25	2.2
30	2.0
35	2.0
40	2.1

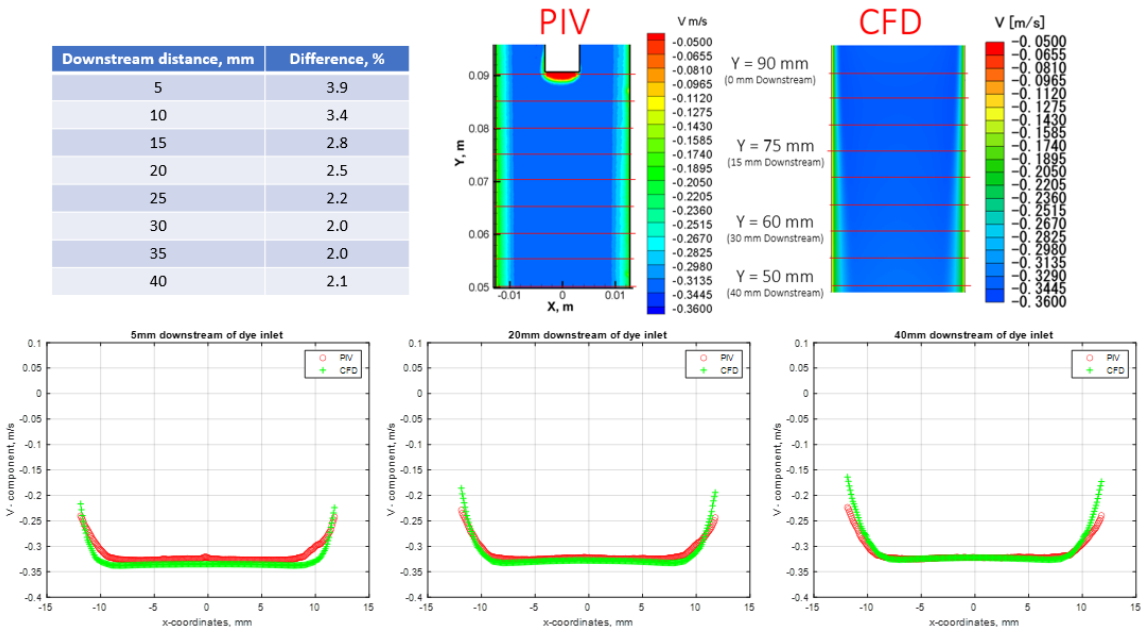

Figure 76: Turbulent flow: PIV and CFD comparisons of v-velocity at 10mm plane for various y-locations.

Comparing the contours, the boundary layer thickness is similar between PIV and CFD which is confirmed in the velocity profiles at 20mm and 40mm downstream. Note, the largest average difference is 3.9% at 5mm, which can be seen in the 5mm downstream velocity profiles. The CFD results are, in general, faster than the turbulent PIV results especially near x = 10mm for this y-location. However, at 20mm and 40mm downstream the difference improves to 2.5% and 2.1%, respectively. Between the three planes analyzed, the overall difference among all of the y-locations was less than 5%, which provides confidence in the CFD model moving forward.

In the laminar validation, the dye head location was compared between experimental and numerical, however this form of comparison for turbulence would prove to be challenging due to the random nature of turbulence. Thus, the vortex shedding frequency was quantified from instantaneous turbulent PIV results and CFD results by averaging the u-velocity along the y-coordinate 25mm downstream of the dye inlet for various points in time. This obtains an average u-velocity with time, which allows a fast-Fourier transform (FFT) to be conducted to determine

the vortex shedding frequency. CFD values were extracted every 0.005 seconds or 200 samples per second which means the Nyquist frequency is equivalent to 100 Hz. The number of samples per second for PIV was set at 24.86, which results in a Nyquist frequency of 12.43 Hz, therefore the PIV sampling rate is the limiting factor in determining the vortex shedding frequency. In the figure below, the average u-velocity is plotted with respect to time (left) and the corresponding frequency of the shedding, based on FFT, is presented (right) for instantaneous (a) PIV and (b) CFD.

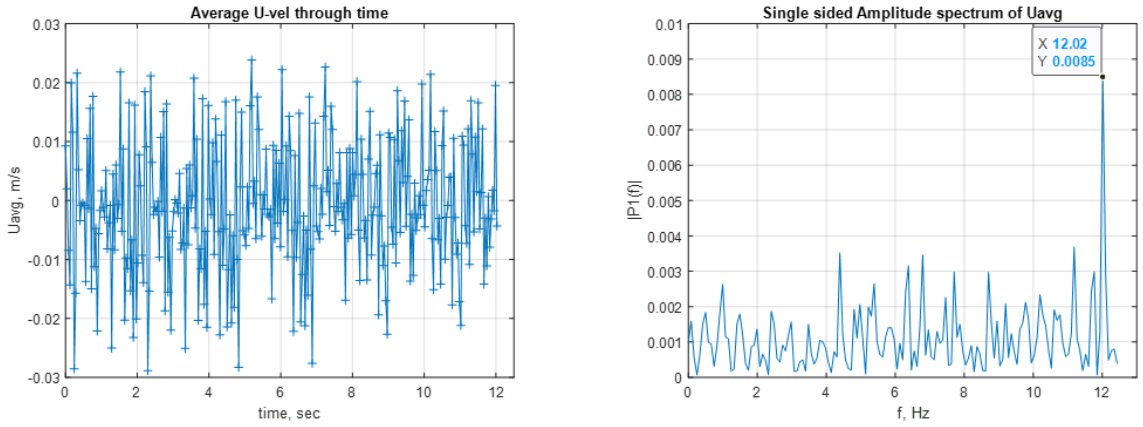

(a)

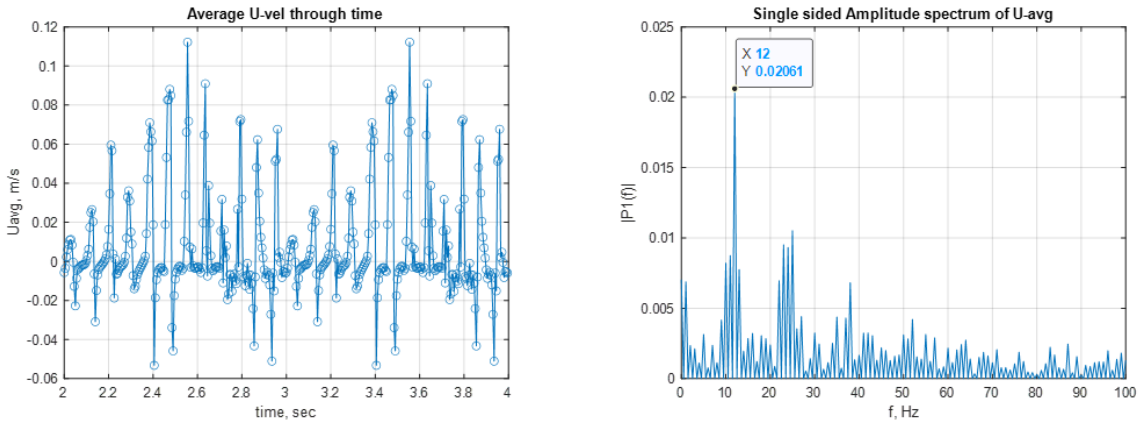

(b)

Figure 77: Average u-velocity along the y-coordinate 25mm downstream of the dye inlet with respect to time (left) and the corresponding frequency plot (right) for the instantaneous (a) PIV and (b) CFD results.

Based on the frequency plots, the vortex shedding frequency according to turbulent PIV was 12.02 Hz and according to CFD was 12.00 Hz. This difference can be explained by an uncertainty analysis which involves the calculated frequency f_s being divided by the number of samples used during the averaging process N_s, hence $\delta f = f_s/N_s$. The number of samples used from PIV was 300 and the number of samples from CFD was 400, therefore $\delta_{PIV} = 0.04$ Hz and $\delta_{CFD} = 0.03$ Hz which means the difference between CFD and PIV is within the uncertainty limits. This frequency results in a Strouhal number of $St = 1.001$ for $Re = 6100$. Other research conducted by Yadav and Agrawal [80], involved qualitative dye comparisons of various pulsation rates for a submerged water jet which investigated Strouhal numbers of 0.16 – 1.75, however the flow conditions encompassed Reynolds numbers between 540 – 1540.

With the model validated, there are some results from CFD which shed some light on why the DVV results were able to overestimate the PIV results at the center plane. Streamline and iso-

surface plots coupled with average vorticity contours indicate the flow motion circulates around the center region and fluctuates away from the center plane, this can be viewed in Figure 78 below.

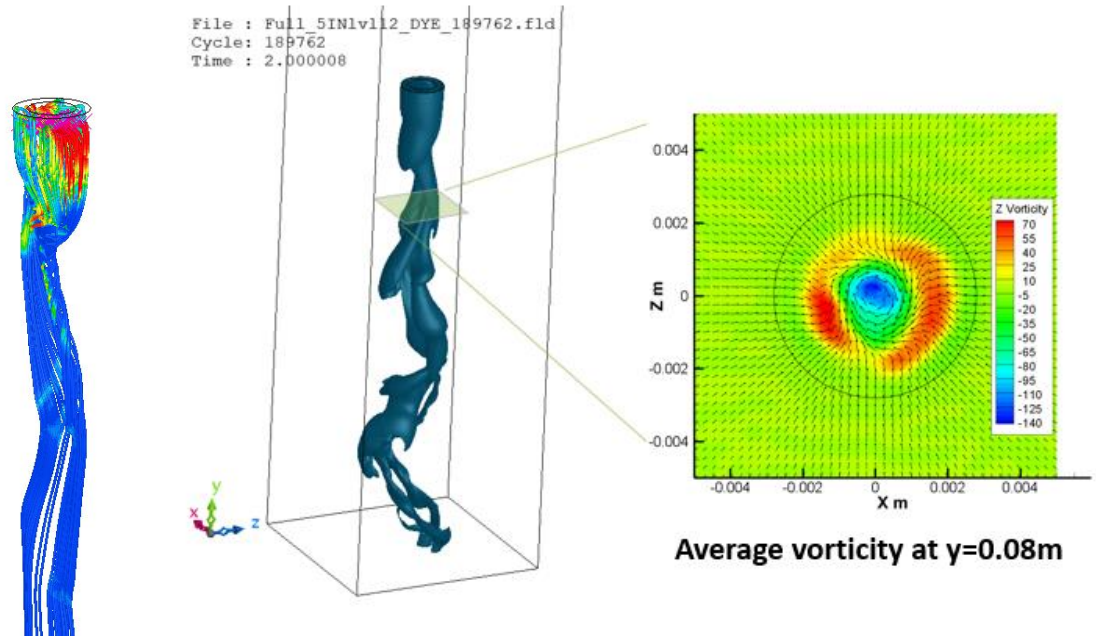

Figure 78: Observation of dye streamlines and iso-surface coupled with the average vorticity located at y = 0.08 meters.

On the left of Figure 78, the streamlines near the dye inlet are displayed, which demonstrates how the fluid movement circulates up toward the dye inlet and then a central swirling begins to occur further downstream. This dye motion is important because the dye propagates away from the center plane which is where the slower velocity resides. Therefore, if the dye moves outside the central region, then it occupies the higher velocities which increases the overall average during the 3D volumetric effect. This phenomenon is the reason for why the DVV results overestimate the PIV results further downstream. Projective image generated from CFD is compared with a single experimental image and phase-averaged experimental image, in the figure below, to provide some validation in this phenomenon occurring within the experiment.

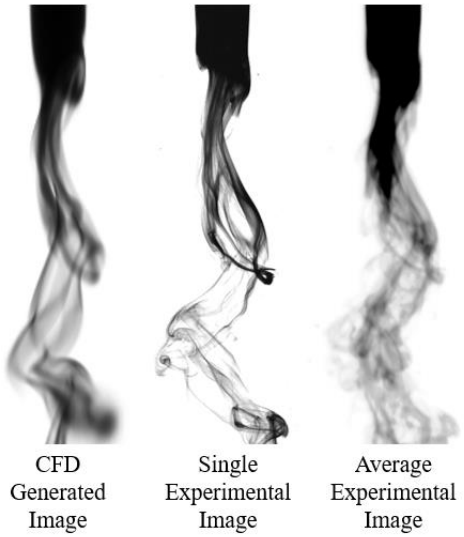

Figure 79: Generated projective image from CFD simulation (left) compared with single experimental image (center) and a phase-averaged experimental image (right) to relate the dye moving out of the center plane.

Comparing the single experimental image to the CFD generated image, there are good resemblances near the dye inlet and further downstream. Slightly downstream of the inlet, there is an initial wave of dye which protrudes to the right, which is shown in all three images. Further downstream, the dye propagates back toward the left with a similar pattern between the other images. The average experimental image provides additional dye concentrations which the single image may not possess, which allows a better comparison with the CFD image since the stochastic nature of the flow may lead the dye to diffuse in other regions. Notice how the experimental image contains dye which seems to rotate about the center as it travels downstream of the inlet, similar to the dye patterning within the CFD image. These images provide evidence of the dye moving out of the slow region which explains the overestimation caused by DVV.

5.2. Analogous Angiographic image generation

Quantifying the error associated with DVV in comparison to PIV not only aids with understanding the limitations of DVV, but also explains the implications of applying DVV to

other applications such as angiographic images where the hemodynamics are critical in pathology. For determining the exact error associated with DVV applied to angiographic images, a method for generating analogous angiographic images was developed. This method uses CFD results to simulate light transmitting through the domain with dye concentrations attenuating portions of the light. This is analogous to angiographic imaging because when x-rays are emitted into the patient, portions of the x-ray energy are attenuated into muscle, bone, soft tissue, iodine contrast, etc. Since medical professionals are typically concerned with blood flow, these images undergo a process called digital subtraction angiography, which uses an initial image to subtract from the current image. This process focuses on the iodine contrast, which is injected in the second image, to visualize the blood flow and reduce unwanted objects such as soft tissue and bone, for instance. Thus, the water in this study does not contribute to light attenuation similarly to the soft tissue and bone in DSA images and to represent the iodine contrast this research used blue dye. The light rays transmitting through the test section serves as an analogy to the x-ray energy which, similar to the light rays, are absorbed by the iodine contrast, or blue dye, which results in lower pixel intensities in that region of the image. Simulating the process of attenuating light ray energy through the CFD domain was accomplished with the Beer Lamber Law which was expressed in equation (21).**Error! Reference source not found.**

5.3. Data preparation for machine learning

To conduct machine learning there needs to be a source of training data to teach the algorithm. This particular research used supervised learning which supplied input data along with the correct output data, or ground truth values. The input data consisted of seven variables which were x- and y-coordinates, u- and v-velocities obtained from OFM, pixel intensity, and x and y intensity gradients. U- and v-velocity ground truth values were extracted from the center plane of

the CFD simulations since the velocities from OFM were based on images generated from CFD dye concentration results. Training data was produced for the laminar case with dye injected in the center and for the turbulent case with dye in the center. For the laminar case, a total of 106 images were generated which led to 53 data files. Since OFM calculates a velocity vector for each individual pixel, even when dye is not present, a selection process was developed which only used data points associated with pixel intensity values less than 180. This criterion was determined based on observations between the calculated vectors and corresponding pixel location within the images. With the criterion applied, the number of data points used in training the laminar model was 423,093, however this did not include all of the data points available. Some of the data points were omitted from the training set to provide a set of data for testing the model. Points with the same x- and y-coordinates were randomly selected for the test set and the training set, for instance, if one pixel location was represented by ten data points, then one of the data points was selected at random to represent the test set. Introducing this random selection aids in minimizing the risk of overfitting the model, which is problematic when applying the model to data outside of the training set. For training the turbulent case, a total of 520 image pairs were used which resulted in over 5,000,000 data points. The last step in preparing the data involves standardizing each variable of the data set, which results in a mean value of zero and a standard deviation of one. This is crucial for the learning process when the variables have different units of measure, because variables with larger values will affect the analysis more than variables with smaller values which results in bias toward the variables with larger values. For example, the pixel intensity ranges from 0 to 256 whereas the u-velocity ranges between -0.0012m/s and 0.00169m/s, thus the pixel intensity would have a stronger influence on the

analysis than the u-velocity. Therefore, standardizing the data provides equitability for the variables and an analysis representative of the data.

5.4. Conclusion

In the process of providing comparative CFD results with experimental results, three separate flow cases were measured and analyzed: 1) laminar flow with dye injected in the center, 2) laminar flow with dye injected near the wall, and 3) turbulent flow with dye injected in the center. Mesh independence was conducted for all three cases to determine the optimal mesh size for computational efficiency with regards to velocity. Multiple convective schemes were compared to study the effects of numerical diffusion in solving for dye concentration and identifying the required octant size to mitigate numerical diffusion for the MUSCL scheme. CFD simulations were conducted for v-velocity comparisons with PIV results and all regions investigated had an average error of less than 5%, thus validating the velocity portion of the simulation. Dye head location was tracked for the laminar cases through the simulation and compared with the experiment. Comparisons at various time points yielded an absolute error less than 1mm for all times up to 3.9 seconds, but after 4.0 seconds the CFD results over predicted the head location by more than 1mm for the laminar case with dye injected in the center. Projective images were compared with experimental images and displayed similar patterns in the diameter/width of the dye as well as propagation downstream. Due to the complexity of turbulent flow, the vortex shedding frequency was examined and compared with the instantaneous PIV results. This led to a difference in frequency of 0.02 Hz which was within the uncertainty of both PIV and CFD. These comparisons provide sufficient evidence in validating the CFD simulation with regard to the dye contrast and overall flow field.

6. Velocity Correction with Machine Learning

In comparing DVV with PIV, it is clear error exists when using DVV for multiple flow conditions and geometries. To improve the accuracy of DVV a correction method driven by machine learning was used. Using machine learning, as opposed to typical engineering approaches, offers cost and time efficiency by leveraging the ability to test and modify variables through an optimization technique. Machine learning is applicable when large data sets are accessible or can be generated, the inputs and outputs are well-defined, and the task allows for some error without the need for a provable solution [68].

6.1. Machine Learning Algorithm

The machine learning algorithm used was a multi-layer perceptron (MLP) algorithm which uses an input layer, one or more hidden layers, and an output layer. This algorithm provides non-linear mapping between inputs and outputs, which allows complex problems to be modeled and furthermore MLP does not make assumptions regarding the data distribution [69]. Another reason why MLP was used as opposed to other deep learning models, was based on the findings of Padhee et al. which did not find statistical significance among the deep learning models [70]. However, computational expense of MLP, as compared to the other deep learning models, was less and therefore MLP was used [70]. In general, MLP is comprised of interconnected nodes, or neurons, which undergo an activation function in which a summation of input variables multiplied by their respective weight parameter (w_i) determine if the neuron sends out a signal to the next hidden layer or output. This process can be visualized in the figure

below which consists of two hidden layers with four neurons in each layer. Input layer consists of three variables and the output layer involves two variables.

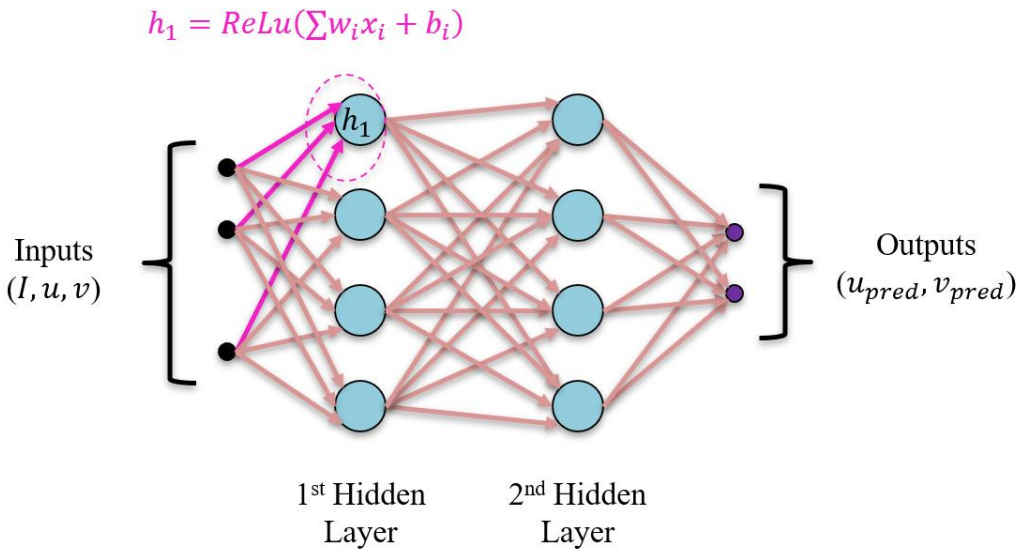

Figure 80: MLP network consisting of an input layer with three variables, two hidden layers each with four neurons, and two output variables.

This type of architecture categorizes MLP as a feedforward algorithm since the computations of the previous layer are sent to the next layer as input and this process is repeated onto the next hidden layers or output layer. However, this process represents one iteration and does not involve the optimization of the weighted values, therefore backpropagation is applied to determine the next set of weighted values by calculating the gradients. After a certain amount of iterations, the process will stop when the gradients of each weighting parameter have converged. Another critical component of a machine learning algorithm is regularization, which serves as a penalty term to either combat against overfitting or underfitting based on the value used. When the regularization parameter, α, is increased the weights are subject to smaller values which decreases the model's non-linear ability and therefore mitigates the risk of overfitting. If α is decreased, then the non-linear characteristics of the model are enhanced which is a result of

larger weight values. L2 regularization was used in MLP which is the Euclidean Norm of the weight matrices which can be written into an optimization problem for a model denoted as $\mathcal{M}$ [71].

$$\mathcal{M} = \underset{w_{ij}}{\arg\min}\left(\sum \frac{\alpha}{2}\sum_{i}\sum_{j} w_{ij}^{2} + \mathcal{L}_{R^2}\right) \tag{22}$$

Here the weight values are signified by w_{ij} and the loss function associated with R^2 is denoted as $\mathcal{L}_{R^2}$. The subscripts i and j indicate which hidden layer and the neuron within that hidden layer, respectively.

6.1.1. Machine Learning Model

Two different MLP algorithms were used; one of them was for the laminar case and the other was used for the turbulent case. In the laminar case the final model consisted of one hidden layer with six neurons, rectified linear unit (ReLU) for the activation function, and 0.01 was used for the regularization value. The turbulent case used three hidden layers with ten neurons in each, ReLU was used for the activation function, and 0.01 for the regularization term. These parameters were determined based on hyperparameter optimization which determines a score relative to a combination of parameters. The score is based on dividing the training data into N number of sets which are used in K-fold cross-validation, where N-1 sets are used for training and one set is used to validate the model. This is completed N-times so each set can be represented as the validation set, therefore N scores are determined, and an average score is calculated which is used in determining which combination of parameters best models the data. This process is displayed below in a visual manner.

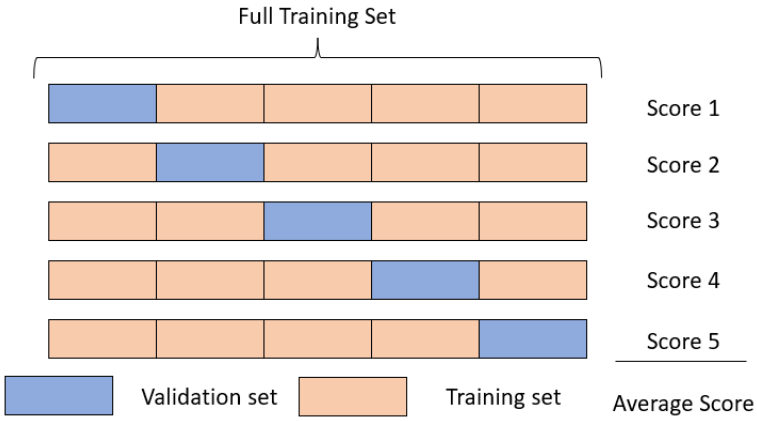

Figure 81: Depiction of cross validation process in determining average score for a particular set of model parameters.

The K-fold cross-validation process above explains how a large training set is divided among five smaller sets, where one of the sets is selected for validating the model which was trained by the other four sets. The model is given a score based on a scoring method such as mean squared error, R^2, or mean absolute error [72]. The model is then trained again but one of the previous sets used for training is now used as the validation set, and the previous validation set is used in training. K-fold Cross-validation helps identify generalized models, since a model could score relatively high for one validation set but score poorly on the other validation sets. This provides a better understanding of the quality of the model and how it may perform to unseen data. Notice this process is applied to one model, so during hyperparameter optimization, each combination of parameters undergoes k-fold cross-validation to provide a comparison with regards to the mean score. For example, the list of parameters used for determining the laminar model, displayed in Table 9, involved 36 unique combinations which were evaluated with k-fold cross-validation and ranked based on their mean score.

Table 9: Parameters used in hyperparameter optimization process for determining the laminar model.

Parameter	Option 1	Option 2	Option 3	Option 4	Option 5	Option 6

Hidden Layer neurons	2	3	4	5	6	7
Activation	ReLU	Tanh	---	---	---	---
Regularization	0.001	0.01	0.1	---	---	---

The scoring method used was R^2 which identified a hidden layer with 6 neurons, ReLU activation, and 0.01 regularization provided optimal results compared to the rest of the combinations with $R^2 = 0.702$. For the turbulent case, the number of hidden layers was increased to three because the highest R^2 value for one hidden layer was 0.496 and increasing to four hidden layers resulted in scores similar to three hidden layers. Table 10 displays the parameters used in the turbulent model optimization process, where the hidden layer neurons are listed in braces ({}) to denote numbers separated by a comma represent an additional hidden layer. For example, {1, 2, 3} would represent three hidden layers with first layer containing one neuron, second layer containing two neurons, and third layer containing three neurons.

Table 10: Parameters used in hyperparameter optimization process for determining the turbulent model.

Parameter	Option 1	Option 2	Option 3	Option 4	Option 5
Hidden Layer neurons	{4,4,4}	{6,6,6}	{8,8,8}	{10,10,10}	{12,12,12}
Activation	ReLU	Tanh	---	---	---
Regularization	0.001	0.01	0.1	---	---

R^2 was used for scoring and the highest mean score was 0.496 which was associated with a model using three hidden layers with ten neurons in each, ReLU as the activation function, and 0.01 was the regularization term.

6.1.2. Results and discussion

For the laminar case, one raw data set from DVV, which was not used in the training process, was used as input for the laminar model and values for u- and v-velocities were predicted. The predicted v-velocities were then compared with DVV and CFD to observe any improvements in accuracy over DVV with respect to CFD. The test case from DVV involved the following image which was generated with CFD results.

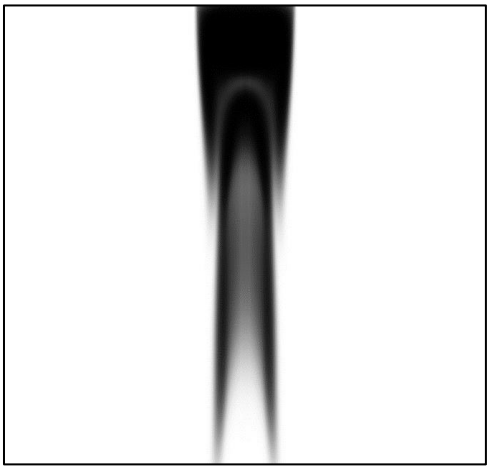

Figure 82: Dye image generated from CFD which was evaluated with DVV to provide input for the laminar MLP model.

Contour plots of v-velocity were qualitatively compared between DVV, CFD, and MLP, which are displayed in the figure below, to show the regions in which MLP corrected DVV.

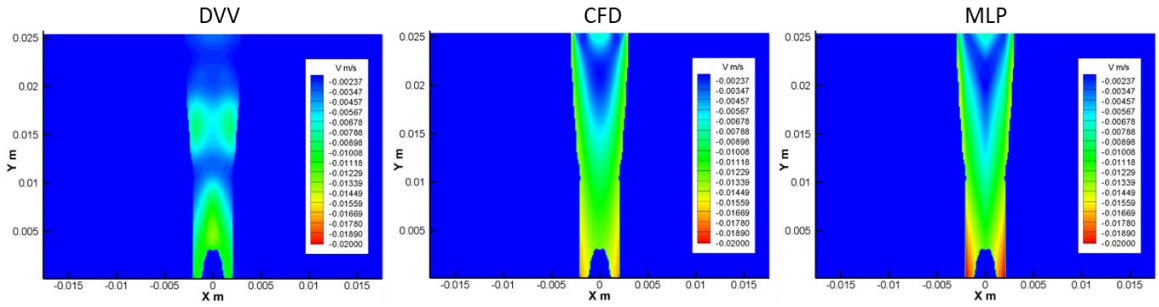

(a) (b) (c)

Figure 83: V-velocity contour comparison between (a) DVV, (b) CFD, and (c) MLP.

Notice how DVV struggles with velocities near the inlet region and near y = 0.01 m, but MLP is able to recover some of these velocities. However, MLP seems to overestimate the velocity near y = 0.001 m in comparison with CFD and the contour plot shows a different shape between CFD and MLP near the dye inlet region. CFD has more of a "U" type shape as opposed to a "V" shape displayed by MLP. This deficiency from MLP could be a result of the poor estimation provided by DVV near the dye inlet region due to low intensity gradients. V-velocities were extracted across y-locations for each of the results and plotted for comparison as seen in Figure 84.

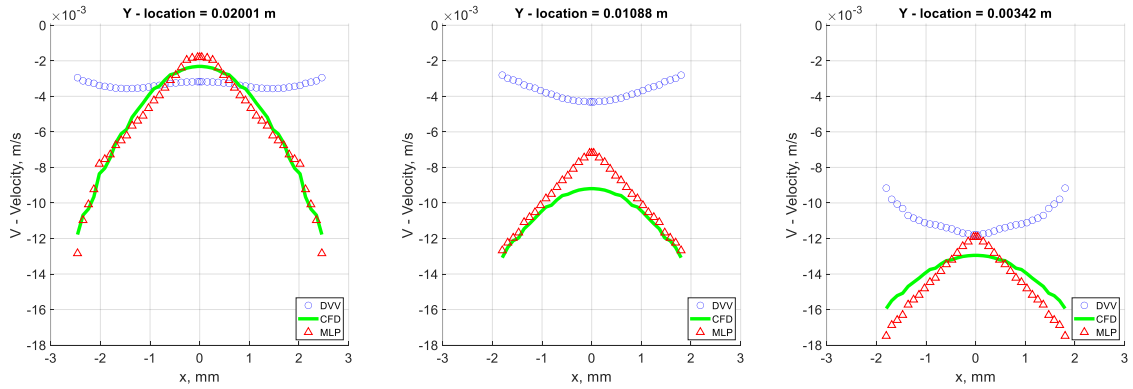

(a) (b) (c)

Figure 84: V-velocity comparisons between DVV, CFD, and MLP across y-locations of (a) 0.02001 m, (b) 0.01088 m, and (c) 0.00342 m.

The velocity profiles at y = 0.02001 meters show an improvement from DVV to MLP in comparison to CFD, where DVV is more uniform whereas CFD and MLP have more of a parabolic shape. The largest absolute error for DVV occurs near x = 2.5 mm with almost 9 mm/s difference, however MLP has a difference of about 1 mm/s. Further downstream at y = 0.01088 meters, the largest error for MLP occurs at x = 0 mm which has a difference of 2 mm/s while DVV has a difference of 5 mm/s. Though, the worst location for DVV is located near x = 1.8 mm which has a difference of almost 10 mm/s, but MLP has minimal difference with CFD. At y = 0.00342 meters, the DVV results perform the best at x = 0 mm with a difference of 1 mm/s, however near the edges of the dye the difference increases to 8 mm/s. MLP provides velocities within 2 mm/s of CFD throughout the x-locations, with the largest difference occurring near the dye edges as well. To determine if MLP provides an improvement in accuracy compared to DVV, the average error across multiple y-locations were plotted for both DVV and MLP with respect to the ground truth of CFD.

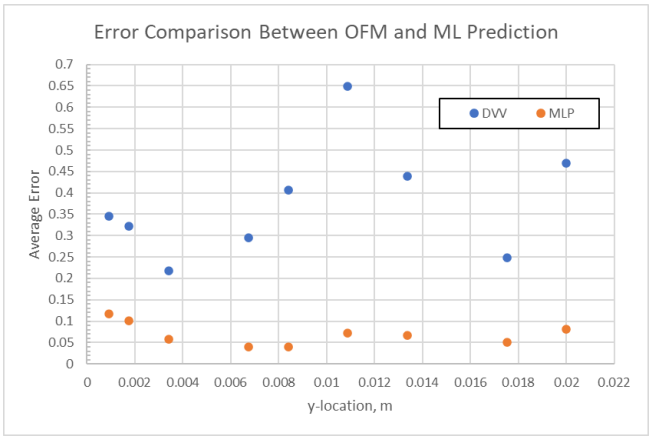

Figure 85: Average error comparison across various y-locations between DVV and MLP for the laminar flow case.

The average error for DVV had a minimum value of 21.8% at y = 0.0034 meters and a maximum error of 64.9% at y = 0.0108 meters. However, the maximum error for MLP was 11.6% at y =

0.0009 meters which is 22.9% better than the DVV error. Overall, the MLP model improves the accuracy of DVV by 30.7% with an average error of 6.9%.

For the turbulent case, the MLP model was applied to several time points to observe the accuracy of MLP throughout various phases of the flow. Time points investigated were t = 1.000s, 2.000s, and 3.000s. For t = 1.000 seconds the V-velocity contours were compared to illustrate the differences between CFD and MLP as well as how MLP corrects DVV. Near y = 0.030 m, DVV exhibits more of a uniform velocity whereas CFD and MLP have larger velocity gradients. Further downstream near y = 0.018 m, there is a velocity difference between CFD and DVV at x = 0.012 m, where CFD has a slightly higher velocity of -0.3500 m/s whereas DVV has a velocity of -0.02250. In general, the velocity contour of DVV, near y = 0.005 m, has a slower velocity compared to CFD and MLP.

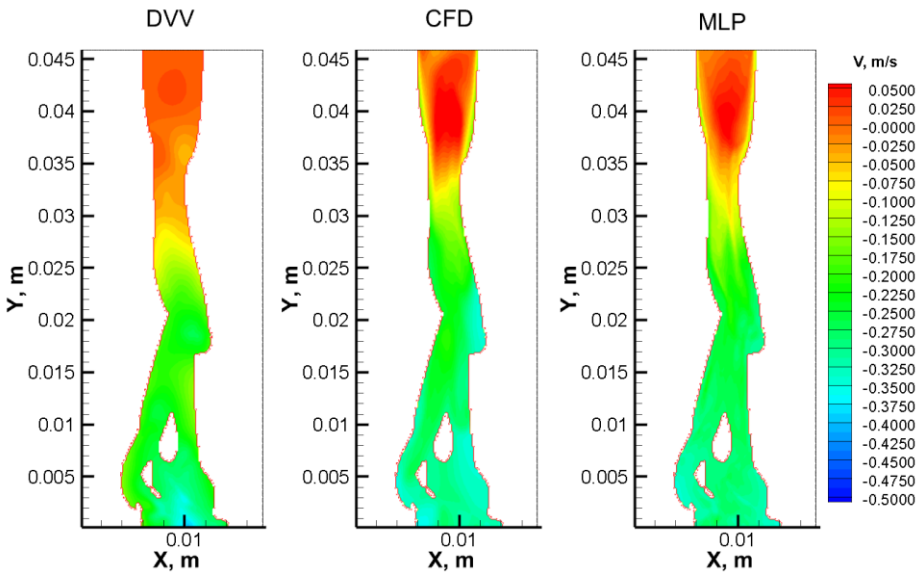

Figure 86: V-velocity contours of DVV (left), CFD (middle), and MLP (right) for t = 1.000 seconds.

For quantitative comparisons, the velocity profiles of DVV, CVD, and MLP along various y-locations were analyzed to illustrate the corrections made by MLP.

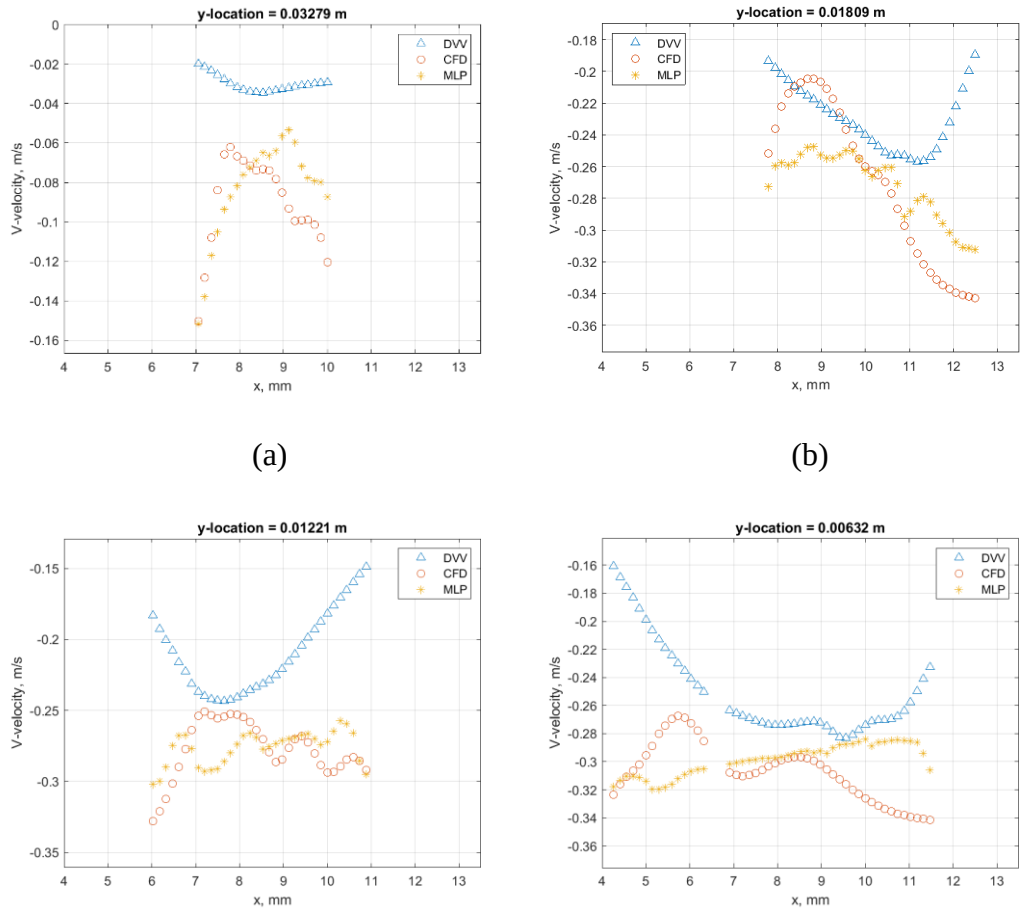

Figure 87: V-velocity profiles at 1.0 seconds along y-locations (a) 0.03279 m, (b) 0.01809 m, (c) 0.01221 m, and (d) 0.00632 m for DVV, CFD, and MLP.

At y = 0.03279 m the DVV profile is fairly uniform at -0.03 m/s whereas the CFD and DVV profiles are more parabolic. The MLP correction is comparable to CFD prior to 9 mm, but beyond 9 mm MLP differs as much as 0.04 m/s. DVV begins to exhibit more of a parabolic shape at y = 0.01809 m and is comparable with CFD for x < 11 mm, however CFD has more of a sinusoidal shape which causes DVV to have larger differences for x > 11 mm. MLP does not compare well with CFD between 8 and 9.5 mm with the largest difference being 0.05 m/s, but provides better correction x > 9.5 mm. Further downstream at y = 0.01221 m, DVV suffers in

accuracy near the edges of the dye, but MLP exhibits good correction with a difference of 0.03 m/s as compared to DVV with a difference of almost 0.14 m/s. MLP improves the accuracy in most x-locations, however DVV does outperform MLP between 7 and 8 mm. Near the outlet at y = 0.00632 m, the difference between MLP and CFD is largest near 11 mm with a value of 0.055 m/s which is 0.025 m/s better than DVV at that location. Average v-velocity error was calculated for DVV and MLP in comparison to CFD along various y-locations to identify regions where MLP improves the accuracy, Figure 88.

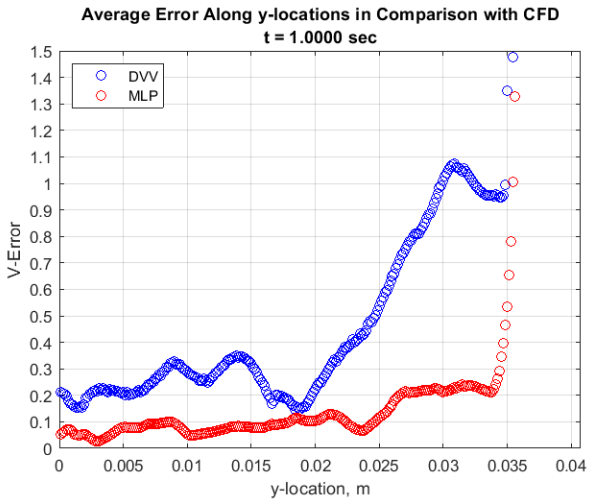

Figure 88: Average v-velocity error in comparison with CFD for DVV and MLP along various y-locations for simulation time 1.0000 seconds.

First observation from the plot above shows MLP improves the accuracy of DVV for all locations, but most dramatic improvement in error reduces from 100% to 20% at 0.03 m which is located near the dye injection. Downstream of 0.025 m, the MLP error fluctuates around 10% which is 15% better than the DVV error for that region.

V-contour plots at 2.0000 seconds are presented in Figure 89, where the contours near the dye inlet are similar to the observations made for 1.0000 second which stated the DVV velocities appear more uniform than CFD and MLP. The region between 0.02 m and 0.025 m have similar

contours among the three results, but near 0.01 m the CFD velocities are faster than DVV, in general, and faster near the dye edges than MLP. DVV exhibits a large velocity of -0.5 m/s at the outlet region whereas CFD and MLP indicate a velocity of -0.35 m/s.

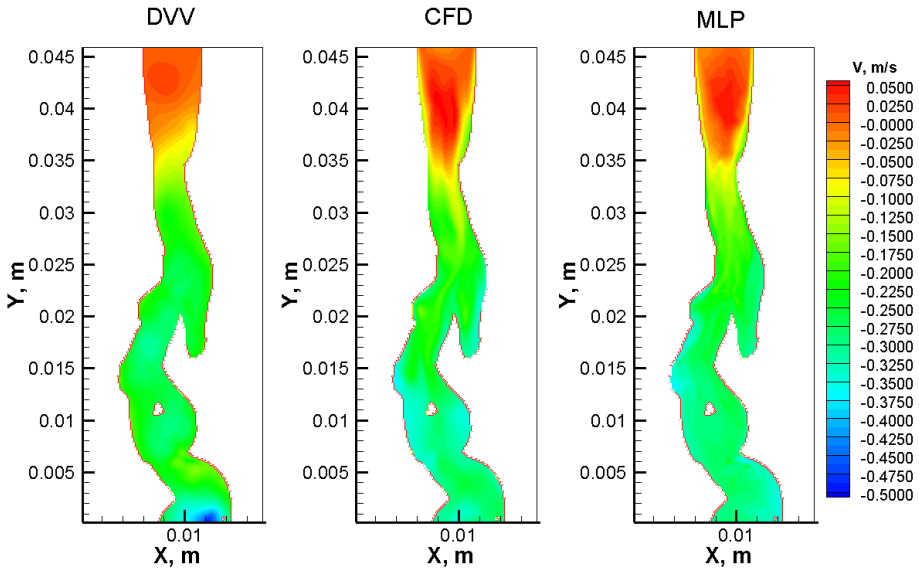

Figure 89: V-velocity contours of DVV (left), CFD (middle), and MLP (right) for t = 2.000 seconds.

Velocity profiles for y-locations 0.03868, 0.03279, 0.02103, and 0.00927 meters are displayed in the figure below.

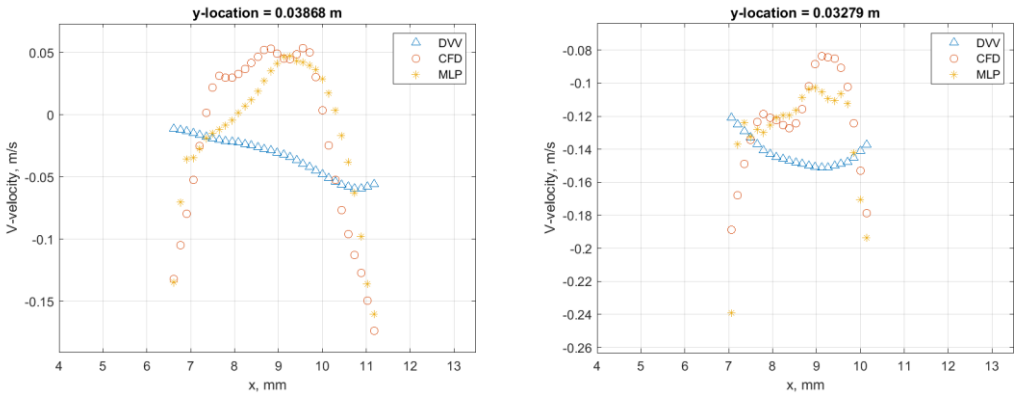

(a) (b)

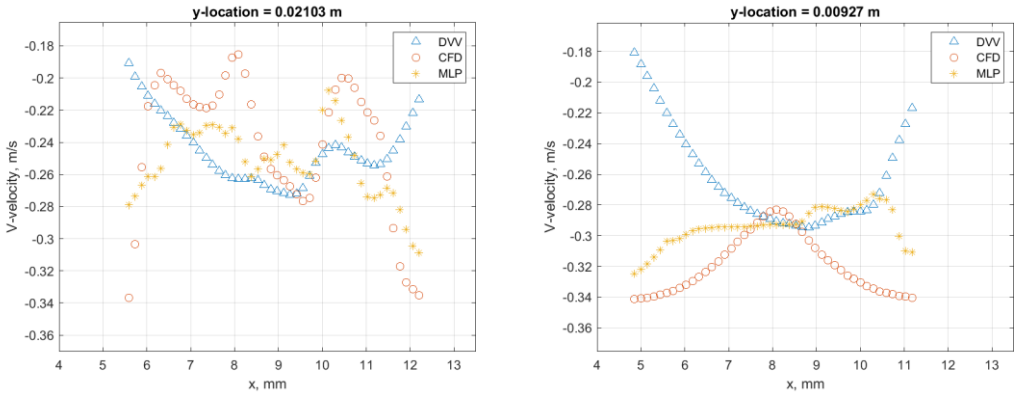

(c) (d)

Figure 90: V-velocity profiles at 2.0 seconds along y-locations (a) 0.03868 m, (b) 0.03279 m, (c) 0.02103 m, and (d) 0.00927 m for DVV, CFD, and MLP.

Near the dye inlet, y = 0.03868 m, the DVV velocity profile demonstrates a uniform profile of about -0.03 m/s, but CFD and MLP have a parabolic shape. MLP has comparable velocities with CFD but suffers between 7.5 and 8.5 mm with a difference of about 0.03 m/s. At y = 0.03279 m, the DVV measurements overestimate CFD by as much as 0.07 m/s near 9.0 mm, but MLP has a difference of 0.02 m/s. The velocity profile from MLP exhibits a similar pattern to CFD at this location as well. Further downstream at y = 0.02103 m, the velocities for DVV between x = 6.5 mm and 11 mm overestimate the CFD values, which was a similar trend observed in the experimental DVV results. Note the velocity profile for DVV suffers the most near the dye edges, but MLP is able to correct these values and obtain more accurate measurements. Near the outlet at y = 0.00927 m, the velocity profiles for all of the measurements are different from one another, where the CFD profile displays concave up from below x = 7 mm and above 9.5 mm then concave down between 7 mm and 9.5mm. Velocity profile of DVV is concave up through its entirety, with large discrepancies, about 0.12 m/s, with CFD near the dye edges of 5 mm and 11 mm. MLP shows more of a uniform profile with concave down trends near the dye edges,

which minimizes the difference with CFD to about 0.02 m/s. To view the improvement of MLP with regards to raw DVV measurements, average v-velocity error was plotted against the y-location throughout the domain in Figure 91.

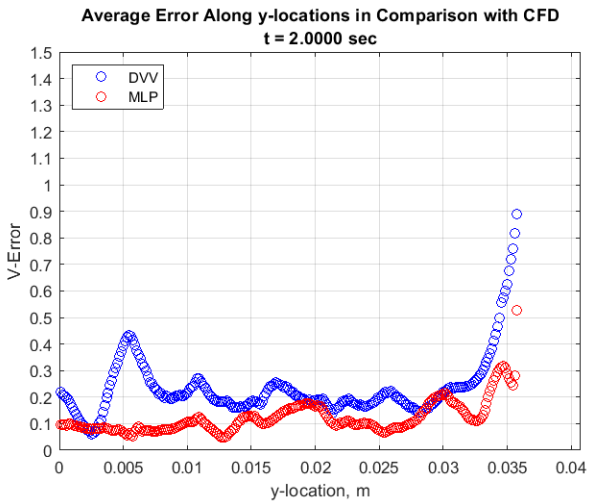

Figure 91: Average v-velocity error in comparison with CFD for DVV and MLP along various y-locations for simulation time 2.0000 seconds.

In comparison to the error plotted for t = 1.0000 seconds, the raw DVV measurements at t = 2.0000 seconds provide better accuracy with an average of about 20%. Comparing DVV to MLP, the error decreases for most of the y-locations with the exception of y = 0.0025 m. On average, the error from MLP is about 12% with the largest error downstream of 0.03 m was 20% located at 0.02 m. The error is greatest closer to the dye inlet, y > 0.035, but the measurements further downstream reduce in error from 30% to 10%, for MLP.

For CFD simulation time of 3.0 seconds the v-contour plots were generated and compared in the figure below. Note the MLP contour displays similar patterns to CFD near y = 0.028 m, where the slower velocity around -0.075 m/s forms down toward the left portion of the dye edge. Near

the outlet, y = 0.002 m, the CFD velocity increases to -0.375 m/s where the MLP velocity remains around -0.300 m/s.

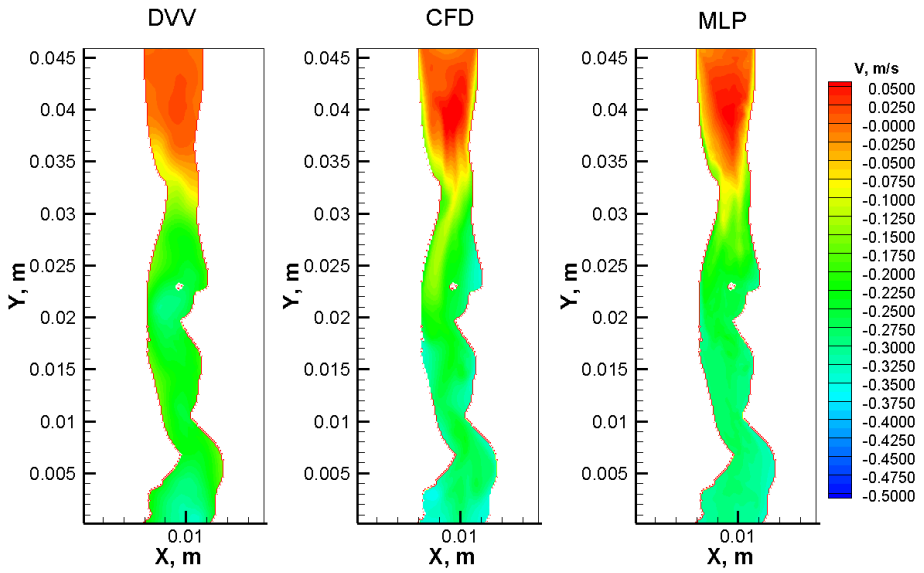

Figure 92: V-velocity contours of DVV (left), CFD (middle), and MLP (right) for t = 3.000 seconds.

The differences in v-velocity between the three measurements are highlighted in the velocity profiles below, which compares profiles at y-locations of 0.03574 m, 0.02397 m, 0.01809m, and 0.00632 m.

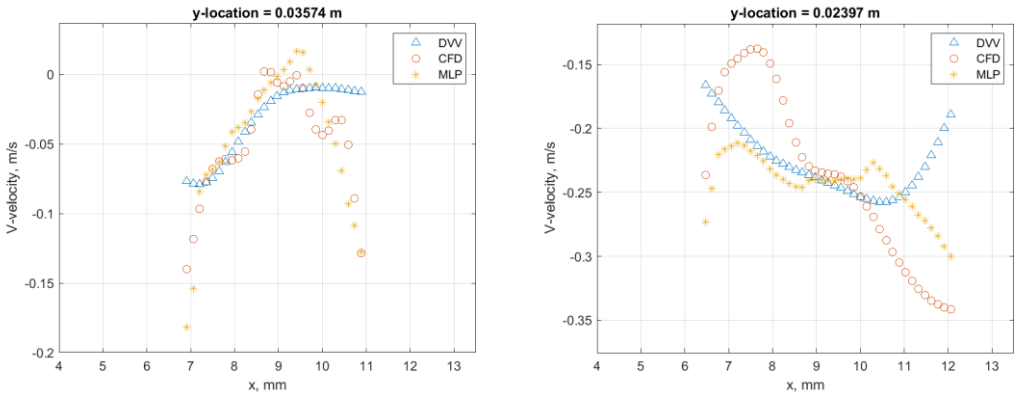

(a) (b)

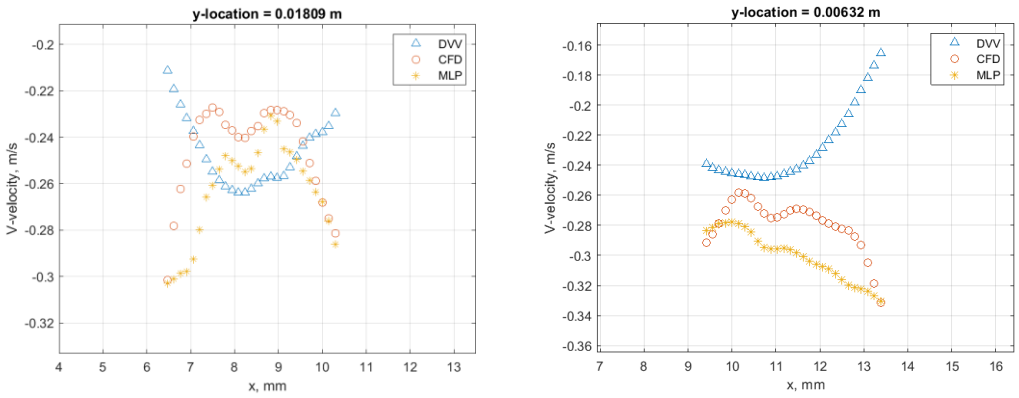

(c) (d)

Figure 93: V-velocity profiles at 3.0 seconds along y-locations (a) 0.03574 m, (b) 0.02397 m, (c) 0.01809 m, and (d) 0.00632 m for DVV, CFD, and MLP.

At y = 0.03574 m, all three measurements have good agreement with one another for x < 9 mm, but DVV underestimates for x > 9 mm with the largest difference being 0.12 m/s. MLP predicts better velocities than DVV, however MLP does overestimate at x = 10.8 mm by 0.02 m/s. Downstream at y = 0.02397 m, MLP has poor accuracy between x = 6.8 mm and x = 8.5 mm compared with DVV, but MLP outperforms DVV near the edges of the dye. Further downstream at y = 0.01809 m, MLP has a similar profile to CFD with more of a concave down trend and has a maximum difference of 0.02 m/s at x = 6.6 mm. However, the profile for DVV has more of a concave up profile with the largest error of 0.09 m/s occurring near the dye edge at x = 6.5 mm. At y = 0.00632 m, the velocity profile of MLP and CFD are similar with slight concave down and average v-velocity of -0.3 m/s and -0.28 m/s, respectively. DVV has large discrepancies for x > 11.5 mm where the largest difference of 0.16 m/s located at the dye edge. Average V-velocity errors along the y-locations are plotted for MLP and DVV in comparison with CFD for the simulation time of 3.0 seconds.

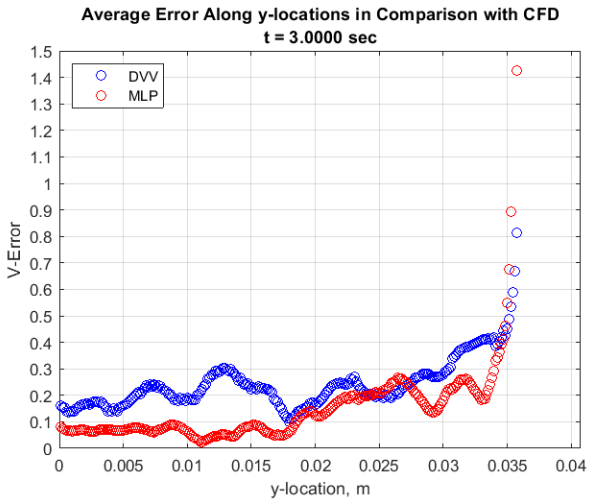

Figure 94: Average v-velocity error in comparison with CFD for DVV and MLP along various y-locations for simulation time 3.0000 seconds.

The average error indicates the largest error occurs near the dye inlet around y = 0.035 m, which results in about 40% error for both MLP and DVV. MLP tends to improve the accuracy for most of the y-locations with the exception of y-locations near 0.025 meters, where the accuracy declines by as much as 6%. Though, downstream of y = 0.017 m, the error for DVV fluctuates around 18% whereas MLP maintains error at or below 10%.

Observing the three time points, the MLP model is able to correct the y-component velocities and improve the accuracy in comparison to raw DVV measurements. However, the U-velocity requires attention as well since this correction method plans to be used in more complex geometry. Thus, the U-velocity contours for each of the time points are illustrated below to observe the accuracy of MLP and DVV with respect to CFD.

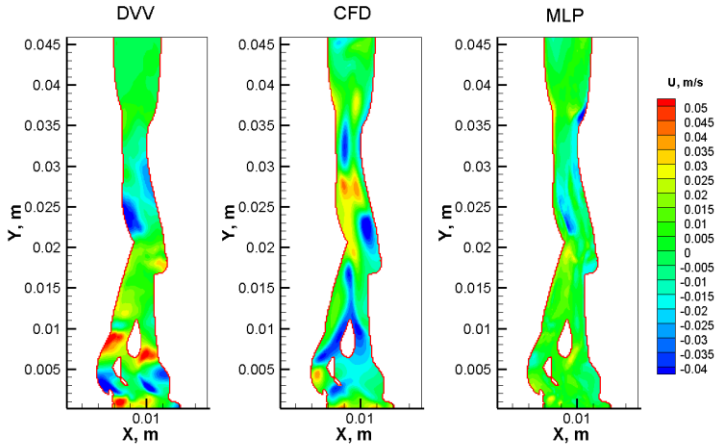
DVV
CFD
MLP
Y, m
X, m
U, m/s
0.05
0.045
0.04
0.035
0.03
0.025
0.02
0.015
0.01
0.005
0
-0.005
-0.01
-0.015
-0.02
-0.025
-0.03
-0.035
-0.04

(a)

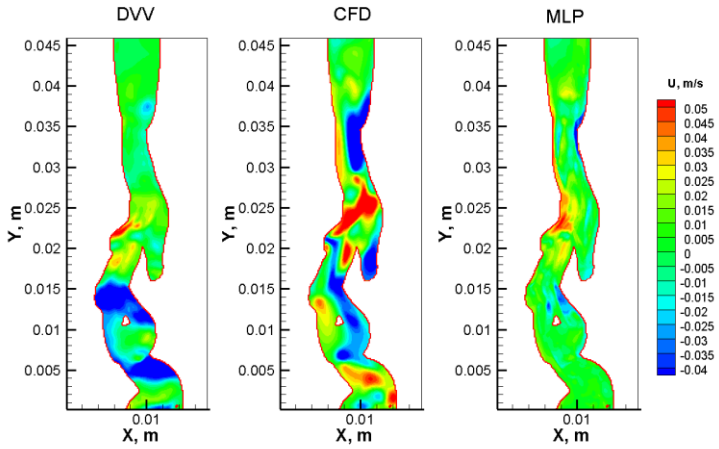
DVV
CFD
MLP
Y, m
X, m
U, m/s
0.05
0.045
0.04
0.035
0.03
0.025
0.02
0.015
0.01
0.005
0
-0.005
-0.01
-0.015
-0.02
-0.025
-0.03
-0.035
-0.04

(b)

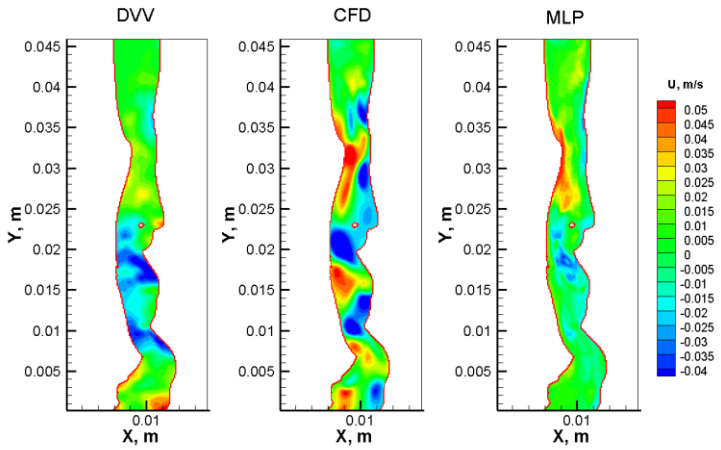

(c)

Figure 95: U-velocity contour comparison between DVV, CFD, and MLP for each of the time steps: (a) 1.0 sec, (b) 2.0 sec, and (c) 3.0 sec.

For the U-contours at 1.0 seconds, the DVV measurements tend to have opposite magnitudes from CFD. For instance, at y = 0.025 m the velocity is negative, but CFD is positive and at y = 0.008 m the U-velocity is positive for DVV and CFD is negative. MLP attempts to correct this, but the results are poor, especially near y = 0.008 m where the average velocity is about 0.015 m/s for MLP and DVV is -0.037 m/s. Measurements from DVV are slightly better at 2.0 seconds, where the velocity at y = 0.024 m is 0.016 m/s and CFD has a velocity of 0.051 m/s. MLP is able to correct DVV to achieve a velocity of 0.039 m/s, which is 23.5% error and is not sufficient enough. Additionally, there are regions where MLP increases the error such as the y-locations between 0.01 m and 0.016 m. DVV calculates a velocity of -0.046 m/s, CFD is -0.039 m/s, and MLP predicts a velocity of -0.005 m/s. MLP introduces almost five times as much error than raw DVV measurements at that particular region. Results from MLP are similar for 3.0 seconds, with some improvement around y = 0.03 m, but overall, the results are not comparable with CFD. From a general perspective, the contour plots for both CFD and DVV incorporate

sharp changes in velocity (as indicated with red and blue regions in close proximity to one another), but MLP seems to have an averaged U-velocity for most of the regions. This may be a result of training the model with all phases of the vortex shedding, which is causing these averaging effects. Since the vortex shedding has a time period of 0.084 seconds and each DVV measurement pertains to 0.005 seconds, there are about 16 possible phases during the time period. Developing a method to train several MLP models based on phase dependent data may provide better accuracy with respect to the U-velocity and V-velocity.

The last case involved all of the instantaneous data sets and averaged their values to form an averaged test case. The same MLP model was used to correct the DVV results and provided the following V-contour plots.

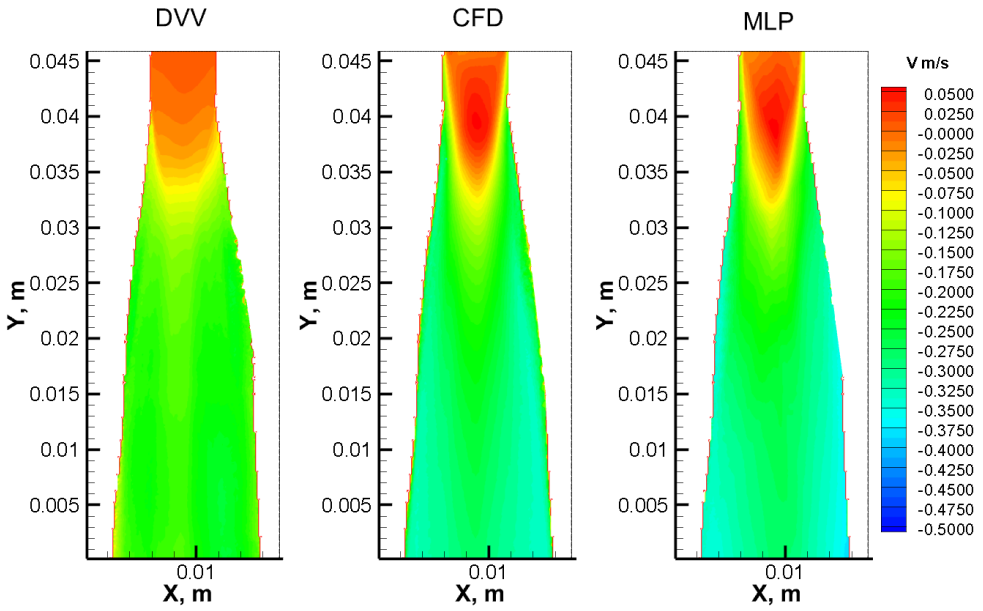

Figure 96: V-velocity contours of DVV (left), CFD (middle), and MLP (right) for averaged test data.

The V-velocity contour for DVV above illustrates a fairly uniform profile between y = 0.045 to 0.035 m, however, CFD and MLP have a parabolic type of profile in that region. Further downstream near y = 0.01 m, CFD exhibits faster flow of -0.320 m/s near the edges and slightly

slower velocity of -0.257 m/s near the core of x = 0.009. Whereas DVV has a speed of -0.207 m/s near the edges and MLP has a velocity of -0.324 m/s, and at the core DVV reveals speeds of -0.190 m/s and MLP has -0.273 m/s. From a qualitative perspective, MLP is able to correct DVV to similar features CFD displays. Velocity profiles were extracted along various y-locations to further compare DVV, CFD, and MLP.

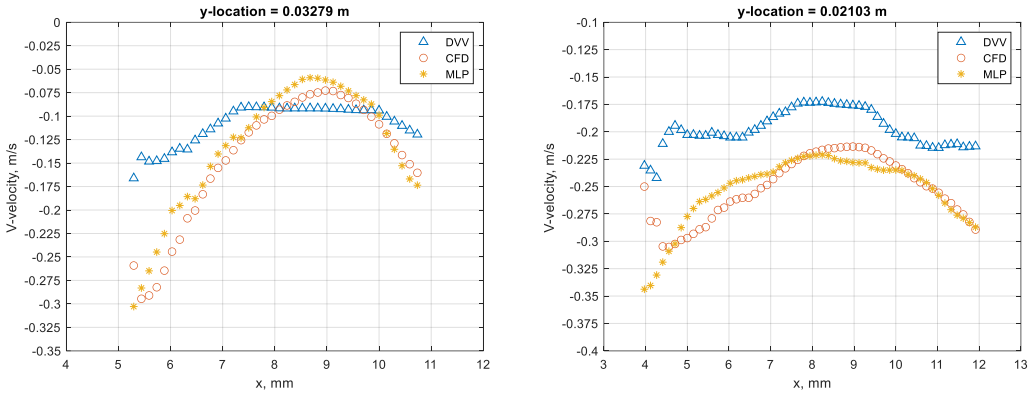

(a) (b)

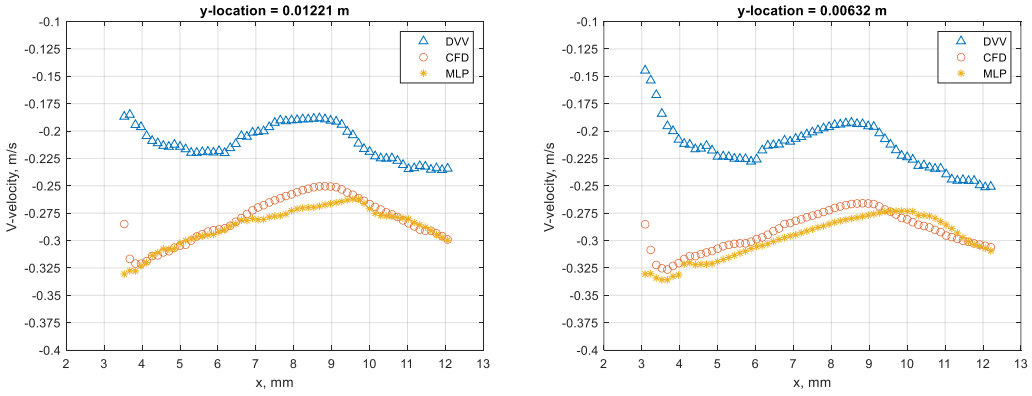

(c) (d)

Figure 97: V-velocity profiles of average data set along y-locations (a) 0.03279 m, (b) 0.02103 m, (c) 0.01221 m, and (d) 0.00632 m for DVV, CFD, and MLP.

Notice in Figure 97(a) the velocity profile for DVV is fairly uniform with a value of about -0.1 m/s, whereas CFD and MLP have parabolic profiles. The MLP profile has similar shape to CFD

profile, but between x = 5 mm to x = 6.5 mm the two methods have a separation in values of about 0.025 m/s. For y = 0.02103 m, the velocity profile from DVV is still fairly uniform with a value of about -0.2 m/s, however CFD and MLP exhibit a parabolic profile. The largest difference between CFD and MLP, away from the edges, is about 0.025 m/s at 5.5 mm which roughly equates to 8.7% error. For the comparisons of Figure 97 (c) and (d), the profiles of MLP and CFD are similar, but DVV has a difference of about 0.06 m/s with CFD which is roughly 24% at x = 8.5 mm. Though, MLP has a difference of 0.02 m/s at x = 8.5 mm which has an error of 8%. To determine the overall improvement of MLP, the two methods, MLP and DVV, are compared with average error along various y-locations.

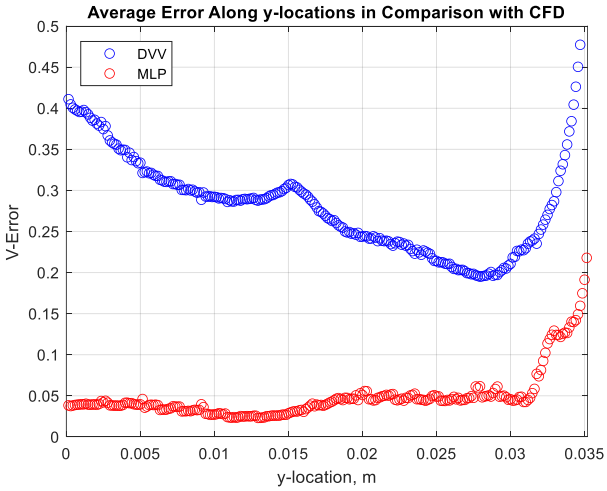

Figure 98: Average v-velocity error in comparison with CFD for DVV and MLP along various y-locations for averaged test set.

The results above illustrate a distinguishable difference between DVV and MLP, with the lowest decrease in error of about 15% at y = 0.028 meters. The error downstream of 0.03 meters, tends to oscillate around 5% error or less, which is half the error seen by the instantaneous cases analyzed prior. This provides encouraging results to use MLP for correcting DVV v-velocity measurements, however the accuracy of shear stress measurements is of upmost importance since wall shear stress is related to initiation, growth, and rupturing of aneurysms. Therefore,

fluid shear stress contours were compared to determine regions where DVV and MLP differ from CFD and where they are similar.

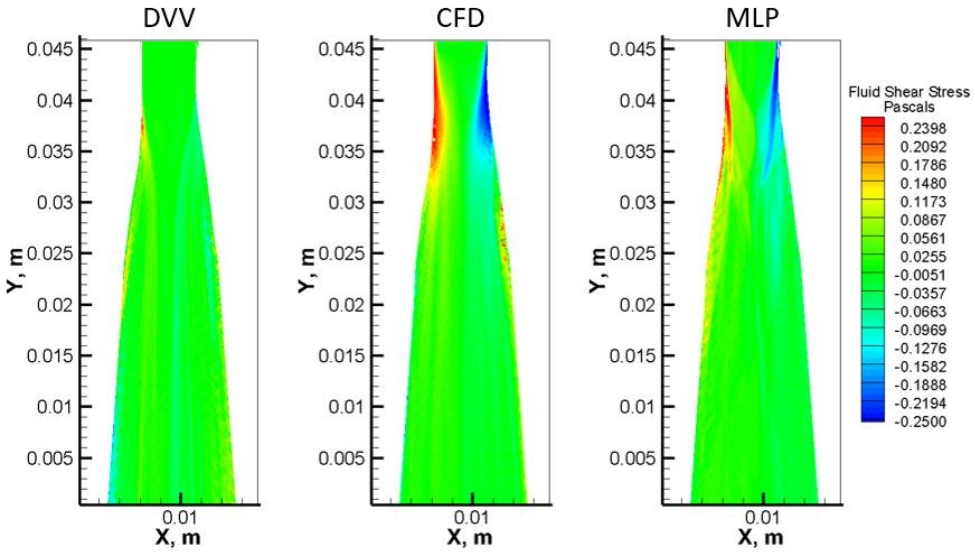

Figure 99: Fluid shear stress contours of DVV (left), CFD (middle), and MLP (right) for averaged test data.

The shear stress contours highlight where DVV suffers to calculate high and low shear stress near the dye inlet region. MLP is able to correct DVV to some degree, however there could be improvements made to MLP for better shear stress predictions. With regards to the average shear stress error along various y-locations, the comparison of DVV and MLP are shown in the figure below.

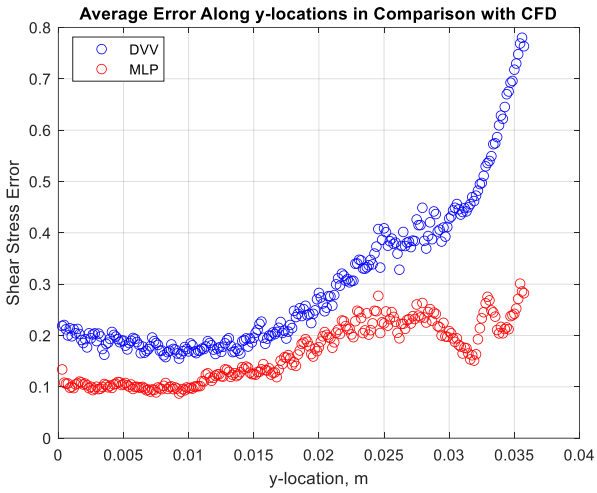

Figure 100: Average fluid shear stress error in comparison with CFD for DVV and MLP along various y-locations for averaged test set.

The average error plot shown above, exposes the error in DVV especially near the dye inlet region. DVV has error as much as 80% near y = 0.035 meters, however MLP was able to reduce the error down to 30%. Further downstream, MLP continues to correct DVV measurements to increase the accuracy of the fluid shear stress measurements up to about 90% accurate. Main insight from these contours and error plots, is that MLP is able to correct DVV measurements to provide an increase an accuracy especially near the dye inlet which is where the high and low shear stress values are located. This provides promising results for using MLP in correcting raw DVV measurements as a method for analyzing medical imaging.

6.1.3. Conclusion

Machine learning algorithm, more specifically MLP, was trained for the laminar case as well as the turbulent case with dye injected in the center. When comparing the velocity profile results for the laminar case, the DVV profile disagreed with the CFD and MLP profiles by exhibiting more of a concave up or uniform shape, while CFD and MLP showed a concave down shape in a parabolic manner. The average v-velocity error for various y-locations showed MLP can increase

the accuracy of raw DVV measurements on a consistent basis. MLP was able to decrease the error associated with DVV from 65% down to 8% and achieve as low of error as 3%. Based on the velocity profiles, MLP reduces the difference between DVV and CFD largely when $|x| > 1.5$ mm which is where the dye edge is formed. This improvement is also seen in the turbulent case, where DVV has difficulties in regions near the edge of the dye and MLP is able to recover some of the difference with CFD. Velocity profiles for the turbulent case are not as simple as the laminar case which is why the MLP and CFD profiles do not agree as well in comparison to the laminar flow. However, the velocity profiles of turbulent MLP do agree better with CFD than the raw DVV profile. This is evident from the average v-error plot for various y-locations, where the error consistently decreases for y-locations downstream of 0.017 m at each of the three time points analyzed. For y-locations upstream of 0.017 m, the error typically decreases for MLP however there are some regions where the accuracy declines, such as the region near y = 0.025 m for t = 3.0 seconds. The error for MLP tends to fluctuate about 10% for locations less than 0.02 meters and around 20% between 0.02 m and 0.033 m. When an average test case was analyzed with MLP, the comparison between CFD and MLP measurements resulted in error of about 5% for the v-velocity. Comparisons of the fluid shear stress were also compared and identified MLP was able to correct DVV measurements near the dye inlet where high and low shear stress were present. The error of DVV was about 80%, but MLP was able to correct the measurements and reduce the error to 30%. Overall, for the laminar and turbulent case, MLP does provide more accurate results than the raw DVV results, which provides encouraging results in the application of machine learning in improving DVV to acquire more accurate results.

6.2. Transition to Medical Applications

Proceeding forward with this research requires additional simulations to transition to medical applications. Since cerebral aneurysms are patient specific, the need for a general machine learning algorithm is necessary. First would be using CFD to simulate flow through multiple aneurysms with various geometries of neck diameter and height. This would lead to a collection of aneurysms with varying aspect ratios (i.e. height with respect to neck diameter). The range of aspect ratios would be based on clinical research on the effect of aneurysm aspect ratio, for instance the work by Huang et al. determined an aspect ratio of 1.6 or greater was significantly associated with rupturing [73]. Therefore, the aneurysms being simulated would focus on an aspect ratio range symmetrical to 1.6, thus providing a data base for aneurysms suspect of high risk. Projective images would be generated from each of the simulations and used for DVV measurements. During the data processing phase, prior to training the machine learning algorithm, the raw DVV coordinates would convert to non-dimensional quantities where the origin (0,0) would be aligned with the center of the aneurysm and the orientation of the aneurysm would need to be consistent among the aneurysm models. This would provide a common ground for each of the aneurysms with respect to geometry, and then the other input variables may include the aspect ratio, pixel intensity, intensity gradients, and DVV velocities. Note, saccular aneurysms are most common for cerebral aneurysms, and there are two types of saccular aneurysms with different flow features. For instance, bifurcated aneurysms are more susceptible to flow impingement on the dome as opposed to side wall aneurysms. Therefore, two machine learning algorithms would be necessary to correct flow features within a side wall aneurysm or a bifurcated aneurysm. Capturing the flow features for every unique aneurysm is

not feasible, however training a model based on the most prevalent and high-risk aneurysm geometries would lead to viable information for medical professionals for most patients.

7. Limitations

There are limitations with this research regarding the experimental, numerical, and machine learning which are beneficial to discuss for moving forward with this project. The experimental limitations include PIV uncertainties, optical distortion, and differences between the in-vitro setup and in-vivo setup. With regards to CFD, there are concerns with flow conditions related to the transition to blood flow characteristics. Some limitations concerning machine learning relate to the ability to handle different geometries and correct the raw DVV measurements. Understanding these limitations can provide beneficial information to determine additional experiments or simulations to conduct for further progress in this subject.

7.1. Experiments

The first limitation to discuss, with regards to in-vitro experiments, is the uncertainty associated with PIV analysis. Since PIV was used in validating CFD, and PIV is not perfect, the uncertainty is needed to understand why CFD comparisons have differences. In positioning the laser, a ruler with 1mm markings was used, which means the centering of the laser may have been off by as much as 1mm. Another factor to consider is the laser sheet, though thin, had a thickness of 2mm which means particles within that thickness were illuminated causing some flow characteristics outside of the intended center plane. When additional planes were analyzed, for instance 5mm plane from center, the laser was translated through the use of a linear stage coupled with a micrometer. The resolution of the micrometer was 0.01mm, therefore translating the laser to the 5mm position may have resulted in an offset of ±0.01mm additional to the uncertainty in

centering the laser. The laser sheet required parallel alignment with the test section which incorporated the use of a ruler with 1mm resolution to measure the distance from the laser sheet to the edge of the test section along the length of the tube in the vertical direction. Therefore, the angle of the laser could have incorporated as much as 1mm displacement along 150mm of travel. Another consideration involves the window size resolution in the cross-correlation process with relation to the test section wall. When the search window includes the wall boundary along with the flow particles, the velocity is averaged between the wall intensity pattern and the moving particle pattern. Thus, additional uncertainty is introduced especially since the velocity gradient is large near the wall. The overall relative uncertainty of PIV measurement on velocity magnitude is estimated less than 2%, but near the wall the relative uncertainty may reach 5-6%.

When comparing DVV with DSA, there are several differences which need to be addressed to understand the implications of using DVV as compared to DSA. DVV uses light ray energy to provide a projective image, which requires attention to light refraction and reflection. DSA uses x-rays which are highly transmissive and therefore not concerned with refraction. The refraction observed in light rays is a result of index refraction which is a property of the medium the light transmits through and is governed by Snell's law. For instance, the index refraction of air is 1.0002 which is different from the index refraction of acrylic ($n_{acrylic} = 1.49$). Based on the incidence angle in which the light ray encounters the medium and the index refraction ratio between the two mediums, there will be a set amount of distortion. This can be viewed in the figure below which illustrates light rays transmitting through the various mediums of the test section.

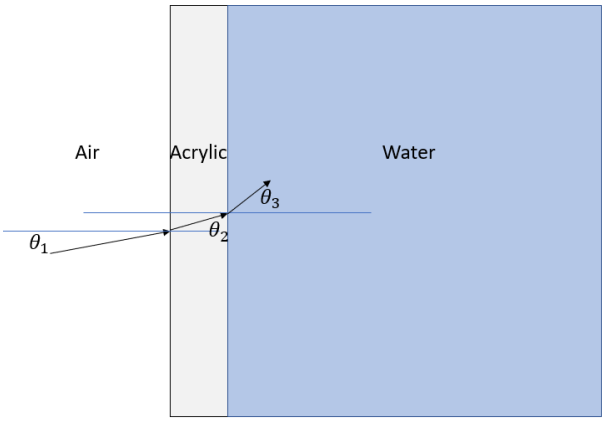

Figure 101: Optical distortion of light ray due to varying index refraction of air, acrylic, and water within the test section.

Assuming $\theta_1 = 3°$ between the light and acrylic wall, the resulting angle would be $\theta_2 = 2.01°$ into the acrylic. For the acrylic and water interaction, the refracted light would have an angle of $\theta_3 = 2.25°$. Applying this back through the other side of the acrylic wall and back in the air would result in an overall angle of 3° again. This type of distortion would result in slight differences in dye projection images if the incidence angle was normal to the acrylic wall, due to the reduction in angle through the acrylic as well as the small amount of travel through the water. However, if the test section was larger, say 1 foot by 1 foot, then the distortion caused by the differences in index refraction would be greater due to the larger distance traveled. Lastly, the rate in which images are acquired successively from DSA and DVV are vastly different. In the DVV experiment, a high-speed camera was used which had the ability to capture images at 6000 frames per second or faster. This constrained dye contrast pixel movement to less than 1.5 pixels, since OFM suffers in accuracy when the movement is any larger. However, DSA images currently acquire rates of about 1-3 frames per second to reduce radiation exposure to the patient, but in some instances the frame rate can achieve 7.5 fps [74]. At these rates, the pixel movement from successive images would result in a much larger displacements (>> 2 pixels), thus hindering the accuracy of OFM. Opposed to increasing the frame rate, and increasing the

radiation dosage to the patient, it may be beneficial to develop a double pulsed x-ray to achieve shorter time durations between successive images. This concept would be similar to double pulsed laser systems used in PIV which allows shorter time durations between two frames. As for the radiation dosage, the time between the double pulse x-ray could be further increased since the main priority is to decrease the time between successive images. Another method to decrease pixel movement between images would be generating additional images between the typical low frame rate as demonstrated by the work of Haouchine et al [75].

7.2. CFD/Numerical Analysis

Regarding CFD simulations, there are limitations to the current research which are critical for progressing this research towards the medical applications. First, the fluid used was water which is Newtonian, whereas the medical application incorporates blood which is non-Newtonian. This is less critical, since other researchers have modeled blood flow as non-Newtonian, however this does raise concern with regards to contrast diffusion. There is some research which studies the diffusion of contrast media in blood, but these simulations model blood as Newtonian fluid [76,77]. This identifies the need for additional experiments to determine if the diffusion effects are significantly different when the fluid is either Newtonian or non-Newtonian. Note, the simulations conducted by Vali et al. assumed the diffusion effects within the transport equations were negligible as a result of the advection effects dominating the flow [77]. Another limitation in progressing this project toward medical applications is the modeling of the wall boundary for the vessel walls. Most simulations model the wall with rigid wall conditions, which differs from in-vivo since the blood vessel walls are elastic. Therefore, additional work is needed to understand the effects of using rigid wall boundary conditions as compared to elastic wall boundary conditions.

7.3. Machine Learning

With the current research, the machine learning model was able to improve the accuracy of laminar and turbulent flow, however there are questions as to whether or not machine learning can correct velocities associated with complex geometries such as aneurysms. This is a reasonable concern especially with the experimental results obtained from the pulsatile flow through an aneurysm model. Due to the complex 3D flow features of the aneurysm, the current technique of using projective images from a single view orientation may not be sufficient to train the machine learning model for obtaining accurate measurements. Therefore, generating a 3D flow structure through the use of projective images from various view orientations would be highly beneficial in complex geometries such as aneurysms. Constructing the 3D flow structure may entail the use of methods such as the algebraic reconstruction technique, or ART, which works well with asymmetric objects and requires about 5 to 10 views with relatively small angles, ±30° [78]. Generating volumetric contrast objects would allow 3D OFM to evaluate the structure thus providing 3D flow measurements. As a result, the raw 3D OFM measurements would allow better patterns and relationships for the machine learning algorithm to detect, as compared to 2D measurements, thus leading to improved accuracy for complex geometries.

8. Conclusion

Initial stages of this research investigated the accuracy of dye visualization velocimetry for a pulsatile flow through a horizontal tube and an in-vitro aneurysm model. Results were promising in measuring detailed flow velocity for the horizontal tube, especially when flow near the center of the tube was estimated. However, when DVV was applied to a more complex flow structure such as the one within the aneurysm, the velocity magnitude suffered in underestimations compared to PIV and failed to capture the change in direction up the aneurysm wall. This exposed the need for a correction method to obtain more accurate measurements from DVV. Thus, a vertical square-tube chamber was designed and constructed to achieve flow within the laminar and turbulent phase for further analysis of DVV. This design provided a simple geometric domain to analyze in CFD simulations for easier comparisons. Three flow cases were studied: 1) Laminar flow with dye injected in the center, 2) laminar flow with dye injected near the wall, and 3) turbulent flow with dye injected in the center. PIV was conducted for each case on various planes to establish a velocity benchmark for comparisons with DVV as well as CFD validation. Over 100 dye visualization trials were conducted, for both laminar cases, and over 200 trials for the turbulent case. These measurements were compared with PIV and the experimental images provided comparisons with the projective dye images generated with CFD. Velocity comparisons between PIV and DVV were made and demonstrated the feasibility in using DVV, though a correction method was still needed to improve the accuracy. CFD simulations for each case were conducted where each case underwent mesh independency

studies and then validated with PIV measurements. Experimental images from the laminar dye visualization cases were used to compare the dye head location with the CFD results and projective images were generated from the CFD simulation to compare dye pattern throughout time. CFD laminar results exhibited good comparison with both the PIV results as well as the dye visualization results. For the turbulent case, the instantaneous PIV measurements were used to calculate the vortex shedding frequency to compare with the frequency associated with the CFD results. This comparison led to good agreement between PIV and CFD on top of the v-velocity comparison. In correcting DVV measurements, machine learning with neural networks was used for the laminar and turbulent case with dye injected in the center. Multi-layer perceptron models were used with one hidden layer for the laminar case and three layers for the turbulent case. Results from the laminar case demonstrated consistent improvement throughout the domain with most significant improvements occurring at the dye edge. The turbulent case displayed improvements by MLP in comparison to raw DVV, however the improvement was consistent mainly downstream. In comparing the velocity profiles, MLP would have similar shape to CFD downstream, however near the dye inlet the profiles struggled to remain comparable throughout the x-locations. Shear stress comparisons showed MLP was able to improve the accuracy of raw DVV consistently throughout the domain, even where high and low shear stress were present. Through this research, several flow cases and geometries were examined which demonstrated the advantages and limitations of DVV, and provided encouraging results when DVV was corrected through the use of machine learning models. This research can have significant impact on applications such as dye diffusion, DSA angiography, and others.

9. Future Work

Research performed in this paper consisted of DVV for pulsatile flow in a horizontal tube and in an aneurysm model as well as constant flow in the laminar and turbulent regime within a vertical square tube. The pulsatile experiments exposed pitfalls in using dye visualization since the method attempts to calculate velocity from a 2D image which incorporates the compressing of a 3D flow onto a 2D image. However, these experiments did provide hope in improving DVV through some sort of correction method. This led to the vertical square tube apparatus to study the feasibility in using CFD to aid in correcting velocity measurements from dye visualization. Machine learning was applied to DVV for the laminar and turbulent case, however the error associated with the turbulent case could be improved further. To improve the machine learning model, it may require several separate models which are used for separate phases of the flow, since the vortex shedding causes variations in the flow field. This could then serve as a technique for improving DVV results in pulsatile flow by creating separate MLP models for the separate phases of the flow. Another experiment which could assist in transitioning DVV to medical images such as DSA, is constant flow through an aneurysm model to provide continuous streams of dye into the aneurysm sac. This would allow dye to propagate into aneurysm sac with optimal intensity gradients within the images. Note the introduction of a convex lens for DVV was during the vertical squared chamber experiment, therefore additional error may have been presented in the aneurysm experiment. Lastly, the machine learning model may benefit from bounding the predicted results to physical conditions such as the Navier-Stokes equations, which

has been demonstrated by Raissi et al. [79]. This would provide predictions consistent with the laws of fluid dynamics.

Bibliography

1. Brody, W. R. (1982) ‘Digital Subtraction Angiography’, *IEEE Transactions on Nuclear Science*, 29(3), pp. 1176–1180. Available at: https://search-ebscohost-com.ezproxy.libraries.wright.edu/login.aspx?direct=true&db=edb&AN=93142644&site=eds-live (Accessed: 17 November 2021).
2. Chilcote, W. A. *et al.* (1981) ‘Digital subtraction angiography of the carotid arteries: a comparative study in 100 patients’, *Radiology*, 139(2), pp. 287–295. doi: 10.1148/radiology.139.2.7012921.
3. Shaughnessy, G. *et al.* (2018) ‘Measuring blood velocity using 4D-DSA: A feasibility study’, *Medical physics*, 45(10), pp. 4510–4518. doi: 10.1002/mp.13120.
4. Taylor, H. G. and Waldram, J. M. (1933) ‘Improvements in the Schlieren method’, *Journal of Scientific Instruments*, 10, pp. 378–389. doi: 10.1088/0950-7671/10/12/304.
5. Hargather, M. J. *et al.* (2011) ‘Seedless Velocimetry Measurements by Schlieren Image Velocimetry’, *AIAA Journal*, 49(3), pp. 611–620. doi: 10.2514/1.J050753.
6. Ozawa, Y. *et al.* (2020) ‘Single-pixel resolution velocity/convection velocity field of a supersonic jet measured by particle/schlieren image velocimetry’, *Experiments in Fluids*, 61(6), pp. 1–18. doi: 10.1007/s00348-020-02963-1.
7. Kouchi, T., Masuya, G. and Yanase, S. (2017) ‘Extracting dominant turbulent structures in supersonic flow using two-dimensional Fourier transform’, *EXPERIMENTS IN FLUIDS*, 58(8), p. 98. doi: 10.1007/s00348-017-2377-z.

8. Estevadeordal, J. and Goss, L., 2005, January. PIV with LED: particle shadow velocimetry (PSV) technique. In *43rd AIAA aerospace sciences meeting and exhibit* (p. 37).
9. Hessenkemper, H. and Ziegenhein, T. (2018) 'Particle Shadow Velocimetry (PSV) in bubbly flows', *International Journal of Multiphase Flow*, 106, pp. 268–279. doi: 10.1016/j.ijmultiphaseflow.2018.04.015.
10. L. P. Goss, J. Estevadeordal and J. W. Crafton, "Velocity Measurements Near Walls, Cavities, and Model Surfaces Using Particle Shadow Velocimetry (PSV)," 2007 22nd International Congress on Instrumentation in Aerospace Simulation Facilities, 2007, pp. 1-8, doi: 10.1109/ICIASF.2007.4380874.
11. Estevadeordal, J. and Goss, L., 2005, June. An Investigation of Particle-Shadow Velocimetry (PSV) For Transonic-Flow Applications. In *35th AIAA Fluid Dynamics Conference and Exhibit* (p. 5009).
12. Aguirre-Pablo, A. A., Langley, K. R. and Thoroddsen, S. T. (2020) 'High-Speed Time-Resolved Tomographic Particle Shadow Velocimetry Using Smartphones', *APPLIED SCIENCES-BASEL*, 10(20), p. 7094. doi: 10.3390/app10207094.
13. Durhasan, T. and Karasu, I. (2019) 'Dye visualization over double delta wing with various kink angles', *JOURNAL OF VISUALIZATION*, 22(4), pp. 669–681. doi: 10.1007/s12650-019-00562-9.
14. Kawaji, M. (1998) 'Two-phase flow measurements using a photochromic dye activation technique', *Nuclear Engineering and Design*, 184(2), pp. 379–392. doi: 10.1016/S0029-5493(98)00210-6.

15. Yang, Z., and Johnson, M., "Velocimetry based on dye visualization for a pulsatile tubing flow measurement," Appl. Opt. **58**, C7-C13 (2019)
16. Yu, H. *et al.* (2019) 'An In-Vitro Flow Study Using an Artificial Circle of Willis Model for Validation of an Existing One-Dimensional Numerical Model', *ANNALS OF BIOMEDICAL ENGINEERING*, 47(4), pp. 1023–1037. doi: 10.1007/s10439-019-02211-6.
17. Hammer, M. (2014). X-Ray Physics: X-Ray Interaction with Matter, X-Ray Contrast, and Dose - XRayPhysics. [online] xrayphysics.com. Available at: http://xrayphysics.com/attenuation.html.
18. Mayfield (2020). angiogram. [online] Mayfieldclinic.com. Available at: https://mayfieldclinic.com/pe-angio.htm.
19. Meng, H. *et al.* (2014) 'High WSS or Low WSS? Complex Interactions of Hemodynamics with Intracranial Aneurysm Initiation, Growth, and Rupture: Toward a Unifying Hypothesis', *AMERICAN JOURNAL OF NEURORADIOLOGY*, 35(7), pp. 1254–1262. doi: 10.3174/ajnr.A3558.
20. Munarriz, P.M., Gómez, P.A., Paredes, I., Castaño-Leon, A.M., Cepeda, S. and Lagares, A. (2016). Basic Principles of Hemodynamics and Cerebral Aneurysms. World Neurosurgery, 88, pp.311–319.
21. Hashimoto, T., Hui Meng and Young, W. L. (2006) 'Intracranial aneurysms: links among inflammation, hemodynamics and vascular remodeling', Neurological Research, 28(4), pp. 372–380.

22. Sho, E. et al. (2002) ‘Arterial Enlargement in Response to High Flow Requires Early Expression of Matrix Metalloproteinases to Degrade Extracellular Matrix’, Experimental and Molecular Pathology, 73(2), pp. 142–153. doi: 10.1006/exmp.2002.2457.

23. Miura, Y. et al. (2013) ‘Low Wall Shear Stress Is Independently Associated with the Rupture Status of Middle Cerebral Artery Aneurysms’, STROKE, 44(2), p. 519–+. doi: 10.1161/STROKEAHA.112.675306.

24. Szajer, J. and Ho-Shon, K. (2018) ‘A comparison of 4D flow MRI-derived wall shear stress with computational fluid dynamics methods for intracranial aneurysms and carotid bifurcations — A review’, *Magnetic Resonance Imaging*, 48, pp. 62–69. doi: 10.1016/j.mri.2017.12.005.

25. Foundation, J.N. (n.d.). Types of Cerebral Aneurysms. [online] Joe Niekro Foundation. Available at: https://www.joeniekrofoundation.com/understanding/types-of-cerebral-aneurysms/.

26. Withers, K., Carolan-Rees, G. and Dale, M. (2013). Pipeline™ Embolization Device for the Treatment of Complex Intracranial Aneurysms. Applied Health Economics and Health Policy, 11(1), pp.5–13.

27. Van Rooij, W. J., and M. Sluzewski. "Procedural morbidity and mortality of elective coil treatment of unruptured intracranial aneurysms." *American Journal of Neuroradiology* 27, no. 8 (2006): 1678-1680.

28. Wardlaw, J. M. and White, P. M. (2000) ‘The detection and management of unruptured intracranial aneurysms’, *Brain: a journal of neurology*, 123 (Pt 2), pp. 205–221. doi: 10.1093/brain/123.2.205.

29. Wentland, A. L., Grist, T. M. and Wieben, O. (2013) 'Repeatability and Internal Consistency of Abdominal 2D and 4D Phase Contrast MR Flow Measurements', *Academic Radiology*, 20(6), pp. 699–704. doi: 10.1016/j.acra.2012.12.019.
30. Cibis, M. *et al.* (2016) 'Relation between wall shear stress and carotid artery wall thickening MRI versus CFD', *Journal of Biomechanics*, 49(5), pp. 735–741. doi: 10.1016/j.jbiomech.2016.02.004.
31. Bonner R.F., Clem T.R., Bowen P.D., Bowman R.L. (1981) Laser-Doppler Continuous Real-Time Monitor of Pulsatile and Mean Blood Flow in Tissue Microcirculation. In: Chen SH., Chu B., Nossal R. (eds) Scattering Techniques Applied to Supramolecular and Nonequilibrium Systems. NATO Advanced Study Institutes Series, vol 73. Springer, Boston, MA. https://doi.org/10.1007/978-1-4684-4061-4_31.
32. Obeid, A. N. *et al.* (1990) 'A critical review of laser Doppler flowmetry', *Journal of medical engineering & technology*, 14(5), pp. 178–181. doi: 10.3109/03091909009009955.
33. Brigida R, Misciasci T, Martarelli F, Gangitano G, Ottaviani P, Rollo M, Marano P. Evolution of digital angiography systems. Rays. 2003 Jan-Mar;28(1):21-8. PMID: 14509177.
34. Conforto, Adriana Bastos, Fregni, Felipe, Puglia Jr., Paulo, Leite, Claudia da Costa, Yamamoto, Fabio Iuji, Coracini, Karen F., & Scaff, Milberto. (2006). Comparison between digital subtraction angiography and magnetic resonance angiography in investigation of nonlacunar ischemic stroke in young patients: preliminary results. Arquivos de Neuro-Psiquiatria, 64(2b), 353-358. https://doi.org/10.1590/S0004-282X2006000300001.

35. Byun, H. S. and Rhee, K. (2004) ‘CFD modeling of blood flow following coil embolization of aneurysms’, *Medical Engineering and Physics*, 26(9), pp. 755–761. doi: 10.1016/j.medengphy.2004.06.008.

36. SimScale. (n.d.). Non-Newtonian Models : SimScale Documentation. [online] Available at: https://www.simscale.com/docs/simulation-setup/materials/non-newtonian-models/.

37. Yi, H., Yang, Z., Johnson, M., Bramlage, L., & Ludwig, B. (2022). Developing an in vitro validated 3D in silico internal carotid artery sidewall aneurysm model. *Frontiers in Physiology*, *13*, 2669.

38. Yi, H., Yang, Z., Johnson, M., Bramlage, L., & Ludwig, B. (2022). Hemodynamic characteristics in a cerebral aneurysm model using non-Newtonian blood analogues. *Physics of Fluids*, *34*(10), 103101.

39. Malvè, M. et al. (2012) ‘Unsteady blood flow and mass transfer of a human left coronary artery bifurcation: FSI vs. CFD’, International Communications in Heat and Mass Transfer, 39(6), pp. 745–751. doi: 10.1016/j.icheatmasstransfer.2012.04.009.

40. Javadi, A, Karbaschi, M, Bastani, D, Ferri, JK, Kovalchuk, VI, Kovalchuk, NM, Javadi, K & Miller, R 2014, ‘Marangoni instabilities for convective mobile interfaces during drop exchange: Experimental study and CFD simulation’, *Colloids and Surfaces A: Physicochemical and Engineering Aspects*, vol. 441, pp. 846–854.

41. Karch, G. K. *et al.* (2012) ‘Visualization of Advection-Diffusion in Unsteady Fluid Flow’, *Computer Graphics Forum*, 31(3pt2), pp. 1105–1114. doi: 10.1111/j.1467-8659.2012.03103.x.

42. Cebral, J.R., Mut, F., Sforza, D., Löhner, R., Scrivano, E., Lylyk, P. and Putman, C.M., 2011. Clinical application of image-based CFD for cerebral aneurysms. International journal for numerical methods in biomedical engineering, 27(7), pp.977-992.

43. Quènot, G. M., Pakleza, J., & Kowalewski, T. A. (1998) 'Particle image velocimetry with optical flow'. *Experiments in Fluids* 25, 177-189.

44. Raffel, M., Willert, C. E., Wereley, S. T., & Kompenhans, J. (2007) 'Particle Image Velocimetry: A Practical Guide', chapter 3-5. Springer.

45. Hu, H., Saga, T., Kobayashi, T., Okamoto, K., & Taniguchi, N. (1998) 'Evaluation of the Cross Correlation Method by Using PIV Standard Images'. Journal of Visualization, Vol. 1, No. 1, 87-94.

46. Keane, R. D., & Adrian, R. J. (1992) 'Theory of cross-correlation analysis of PIV images'. Applied Scientific Research 49, 191-215.

47. Hart, D. P. (1999) 'Super-Resolution PIV by Recursive Local-Correlation'. Journal of Visualization, Vol. 10.

48. Pust, Oliver (2000) 'PIV: Direct Cross-Correlation compared with FFT-based Cross-Correlation'. In: Proceedings of the 10th International Symposium on Applications of Laser Techniques to Fluid Mechanics. Lisbon, Portugal.

49. Bastiaans, R. J. M. (2000) 'Cross-correlation PIV; theory, implementation and accuracy'. Eindhoven University of Technology, Eindhoven, Netherlands.

50. Yang, Z. and Johnson, M. (2017) 'Hybrid particle image velocimetry with the combination of cross-correlation and optical flow method', *JOURNAL OF VISUALIZATION*, 20(3), pp. 625–638. doi: 10.1007/s12650-017-0417-7.

51. Horn, B. K.P., & Schunck, B. G. (1981) ‘Determining Optical Flow’. Artificial Intelligence 17, 185-203.

52. Liu, T., & Shen, L., (2008) ‘Fluid flow and optical flow’. Journal Fluid Mech., Vol. 614, 253-291.

53. Wang, B., Cai, Z., Shen, L., & Liu, T. (2014) ‘An analysis of physics-based optical flow’. *Journal of Computational and Applied Mathematics* 276, 62-80.

54. Quènot, G. M., Pakleza, J., & Kowalewski, T. A. (1998) ‘Particle image velocimetry with optical flow’. *Experiments in Fluids* 25, 177-189.

55. Barbu, V., & Marinoschi, G. (2016) ‘An optimal control approach to the optical flow problem’. Systems & Control Letters 87, 1-9.

56. Heitz, D., Mèmin, E., & Schnörr, C. (2010) ‘Variational fluid flow measurements form image sequences: synopsis and perspectives’. Exp. Fluids 48, 369-393.

57. Corpetti, T., Heitz, D., Arroyo, G., Mèmin, E., & Santa-Cruz, A. (2005) ‘Fluid experimental flow estimation based on an optical-flow scheme’. Experiments in Fluids.

58. Hèas, P., Mèmin, E., Papadakis, N., & Szantai, A. (2007) ‘Layered Estimation of Atmospheric Mesoscale Dynamics from Satellite Imagery’. IEEE Transactions on Geoscience and Remote Sensing, Vol. 45, No. 12.

59. Liu, T., Merat, A., Makhmalbaf, M. H. M., Fajardo, C., & Merati, P. (2015) ‘Comparison between optical flow and cross-correlation methods for extraction of velocity fields from particle images’. Experiments in Fluids 56: 166.

60. Hurlburt, N., & Jaffey, S. (2015) ‘A spectral optical flow method for determining velocities from digital imagery’. Earth Science Informatics 8: 959-965.

61. www.cospheric.com. (n.d.). Tween solutions for Suspension of Hydrophobic Particles in Water for Density Marker Beads in Percoll or other gradients or Flow Visualization. [online] Available at: https://www.cospheric.com/tween_solutions_density_marker_beads.htm [Accessed Feb. 2019].

62. Gonzalez Hernandez, M.A., Moreno Lopez, A.I., A., A., Perales, J.M., Wu, Y. and Xiaoxiao, S. (2013). Design Methodology for a Quick and Low-Cost Wind Tunnel. Wind Tunnel Designs and Their Diverse Engineering Applications.

63. Stonebridge, P.A., Suttie, S.A., Ross, R. and Dick, J., 2016. Spiral laminar flow: a survey of a three-dimensional arterial flow pattern in a group of volunteers. *European Journal of Vascular and Endovascular Surgery*, *52*(5), pp.674-680.

64. Zhang, H., Liang, S., & Lv, X. (2021). Intra-aneurysmal thrombosis and turbulent flow on MRI of large and giant internal carotid artery aneurysms. *Neuroscience Informatics*, *1*(4), 100027.

65. Javadi, A., Karbaschi, M., Bastani, D., Ferri, J.K., Kovalchuk, V.I., Kovalchuk, N.M., Javadi, K. and Miller, R. (2014). Marangoni instabilities for convective mobile interfaces during drop exchange: Experimental study and CFD simulation. *Colloids and Surfaces A: Physicochemical and Engineering Aspects*, 441, pp.846–854.

66. Versteeg, H.K. and W Malalasekera (2011). *An introduction to computational fluid dynamics : the finite volume method*. Harlow: Pearson Education.

67. Michalcová, V., & Kotrasová, K. (2020). The numerical diffusion effect on the CFD simulation accuracy of velocity and temperature field for the application of sustainable architecture methodology. *Sustainability*, *12*(23), 10173.

68. Simeone, O. (2018). A brief introduction to machine learning for engineers. *Foundations and Trends® in Signal Processing*, *12*(3-4), 200-431.

69. Gardner, M. W., & Dorling, S. R. (1998). Artificial neural networks (the multilayer perceptron)—a review of applications in the atmospheric sciences. *Atmospheric environment*, *32*(14-15), 2627-2636.

70. Padhee, S., Johnson, M., Yi, H., Banerjee, T. and Yang, Z., 2022. Machine Learning for Aiding Blood Flow Velocity Estimation Based on Angiography. *Bioengineering*, *9*(11), p.622.

71. Moore, R. C., & DeNero, J. (2011). L1 and L2 regularization for multiclass hinge loss models.

72. Scikit-learn: Machine Learning in Python, Pedregosa *et al.*, JMLR 12, pp. 2825-2830, 2011.

73. Huang, Z.Q., Meng, Z.H., Hou, Z.J., Huang, S.Q., Chen, J.N., Yu, H., Feng, L.J., Wang, Q.J., Li, P.A. and Wen, Z.B., 2016. Geometric parameter analysis of ruptured and unruptured aneurysms in patients with symmetric bilateral intracranial aneurysms: a multicenter CT angiography study. *American Journal of Neuroradiology*, *37*(8), pp.1413-1417.

74. Pearl, M.S., Torok, C., Wang, J., Wyse, E., Mahesh, M. and Gailloud, P., 2015. Practical techniques for reducing radiation exposure during cerebral angiography procedures. *Journal of neurointerventional surgery*, *7*(2), pp.141-145.

75. Haouchine, N., Juvekar, P., Xiong, X., Luo, J., Kapur, T., Du, R., Golby, A. and Frisken, S., 2021. Estimation of High Framerate Digital Subtraction Angiography Sequences at Low Radiation Dose. In *Medical Image Computing and Computer Assisted Intervention*–

MICCAI 2021: 24th International Conference, Strasbourg, France, September 27–October 1, 2021, Proceedings, Part VI 24 (pp. 171-180). Springer International Publishing.

76. Lu, Y.H., Cai, Y., Zhang, Y., Wang, R. and Li, Z.Y., 2021. Digital subtraction angiography contrast material transport as a direct assessment for blood perfusion of middle cerebral artery stenosis. *Frontiers in Physiology*, *12*, p.716173.
77. Vali, A., Abla, A.A., Lawton, M.T., Saloner, D. and Rayz, V.L., 2017. Computational fluid dynamics modeling of contrast transport in basilar aneurysms following flow-altering surgeries. *Journal of biomechanics*, *50*, pp.195-201.
78. Gordon, R., Bender, R. and Herman, G.T., 1970. Algebraic reconstruction techniques (ART) for three-dimensional electron microscopy and X-ray photography. *Journal of theoretical Biology*, *29*(3), pp.471-481.
79. Raissi, M., Yazdani, A., and Karniadakis, G.E. "Hidden fluid mechanics: Learning velocity and pressure fields from flow visualizations." *Science* 367, no. 6481 (2020): 1026-1030.

Appendix A

a. Velocity profiles for “T” regions

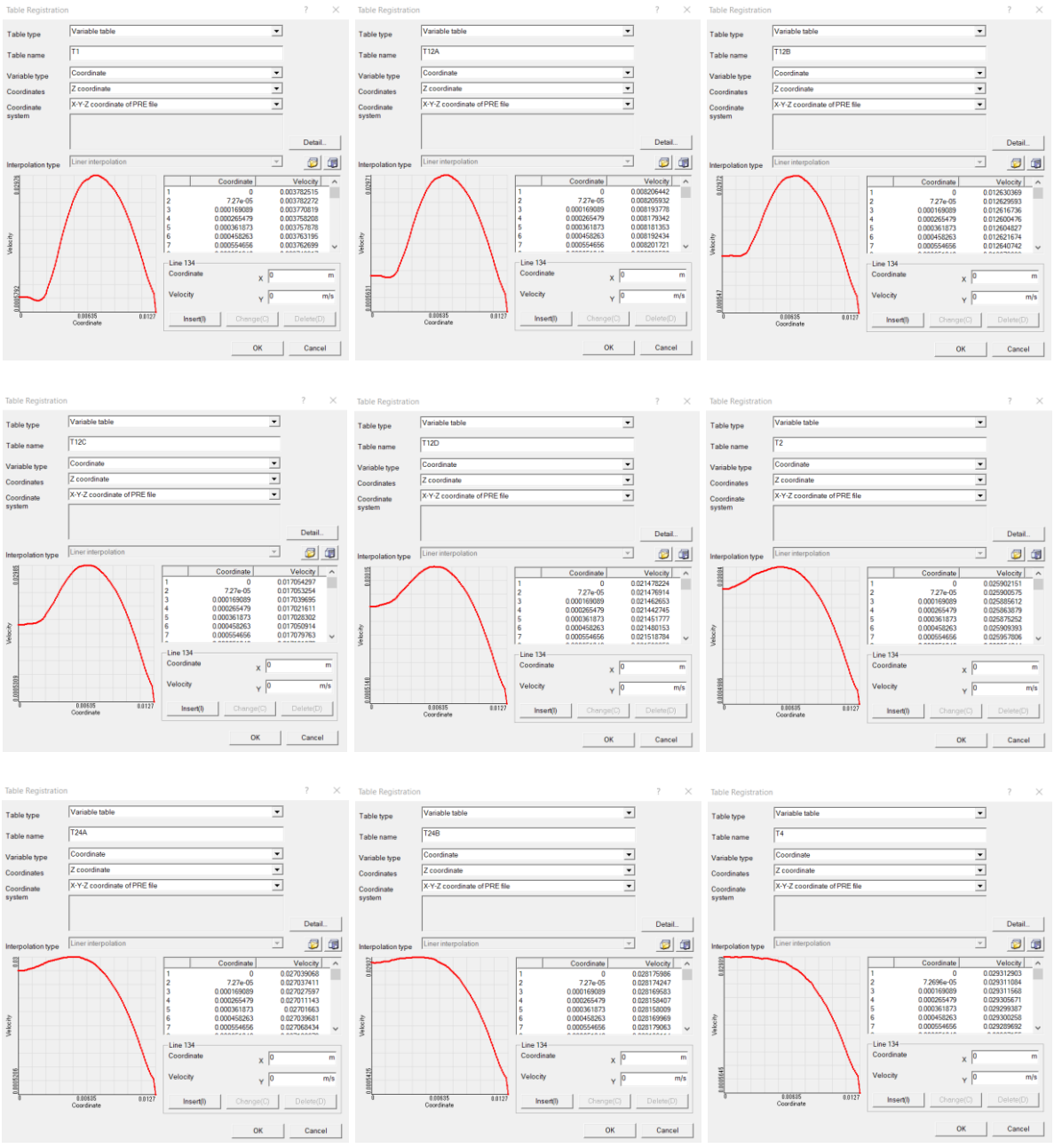

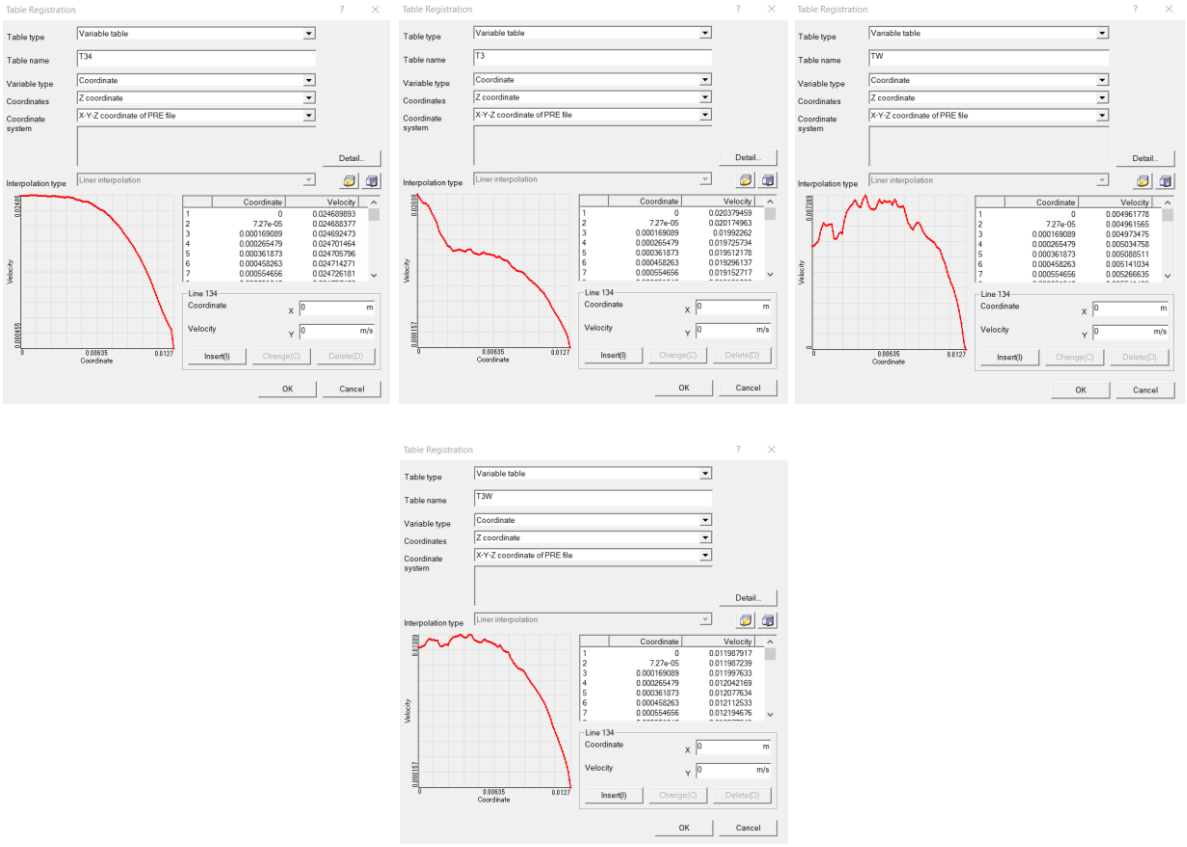

b. Dye concentration profiles for “R” regions

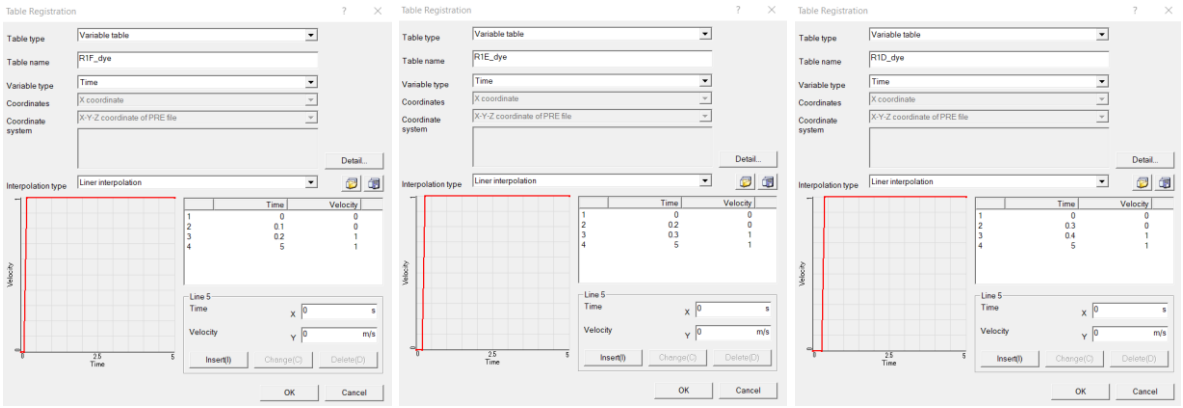

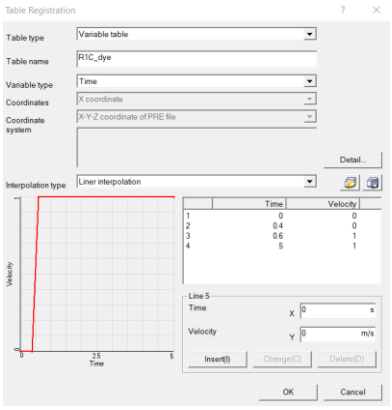
Table Registration
Table type
Variable table
Table name
R1C_dye
Variable type
Time
Coordinates
X coordinate
Coordinate system
X-Y-Z coordinate of PRE file
Detail...
Interpolation type
Liner interpolation
Time
Velocity
1 0 0
2 0.4 0
3 0.6 1
4 5 1
Line 5
Time
Velocity
X 0 s
Y 0 m/s
Insert(I)
Change(C)
Delete(D)
OK
Cancel

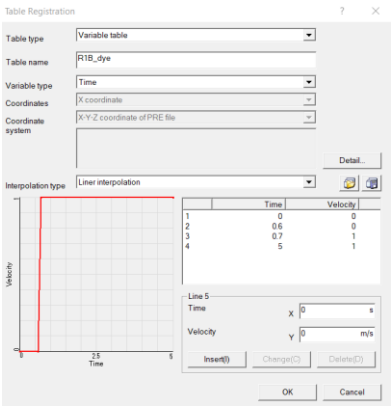
Table Registration
Table type
Variable table
Table name
R1B_dye
Variable type
Time
Coordinates
X coordinate
Coordinate system
X-Y-Z coordinate of PRE file
Detail...
Interpolation type
Liner interpolation
Time
Velocity
1 0 0
2 0.6 0
3 0.7 1
4 5 1
Line 5
Time
Velocity
X 0 s
Y 0 m/s
Insert(I)
Change(C)
Delete(D)
OK
Cancel

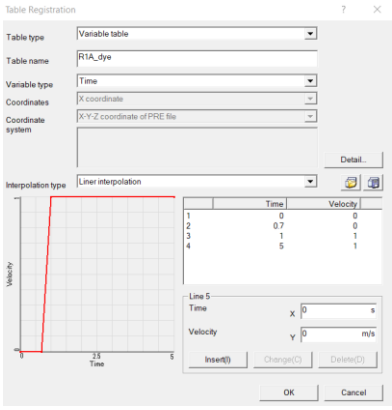
Table Registration
Table type
Variable table
Table name
R1A_dye
Variable type
Time
Coordinates
X coordinate
Coordinate system
X-Y-Z coordinate of PRE file
Detail...
Interpolation type
Liner interpolation
Time
Velocity
1 0 0
2 0.7 0
3 1 1
4 5 1
Line 5
Time
Velocity
X 0 s
Y 0 m/s
Insert(I)
Change(C)
Delete(D)
OK
Cancel

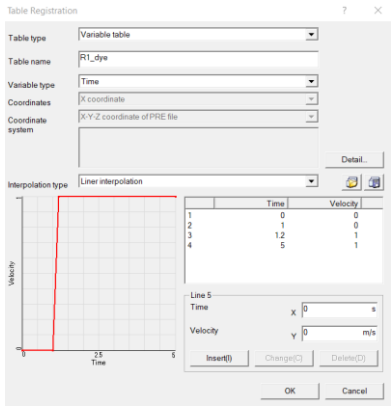
Table Registration
Table type
Variable table
Table name
R1_dye
Variable type
Time
Coordinates
X coordinate
Coordinate system
X-Y-Z coordinate of PRE file
Detail...
Interpolation type
Liner interpolation
Time
Velocity
1 0 0
2 1 0
3 1.2 1
4 5 1
Line 5
Time
Velocity
X 0 s
Y 0 m/s
Insert(I)
Change(C)
Delete(D)
OK
Cancel

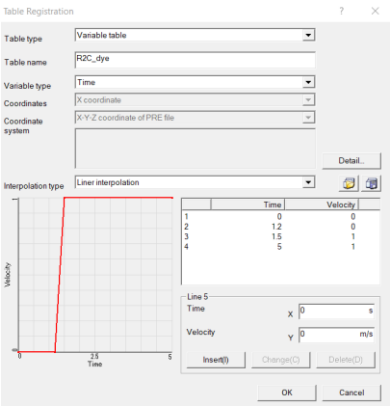
Table Registration
Table type
Variable table
Table name
R2C_dye
Variable type
Time
Coordinates
X coordinate
Coordinate system
X-Y-Z coordinate of PRE file
Detail...
Interpolation type
Liner interpolation
Time
Velocity
1 0 0
2 1.2 0
3 1.5 1
4 5 1
Line 5
Time
Velocity
X 0 s
Y 0 m/s
Insert(I)
Change(C)
Delete(D)
OK
Cancel

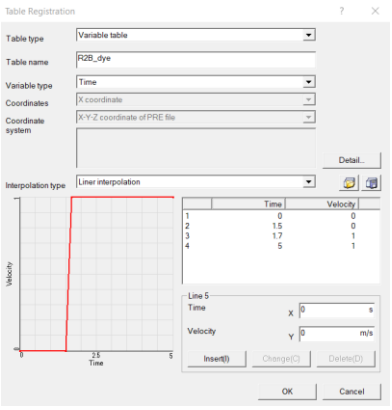
Table Registration
Table type
Variable table
Table name
R2B_dye
Variable type
Time
Coordinates
X coordinate
Coordinate system
X-Y-Z coordinate of PRE file
Detail...
Interpolation type
Liner interpolation
Time
Velocity
1 0 0
2 1.5 0
3 1.7 1
4 5 1
Line 5
Time
Velocity
X 0 s
Y 0 m/s
Insert(I)
Change(C)
Delete(D)
OK
Cancel

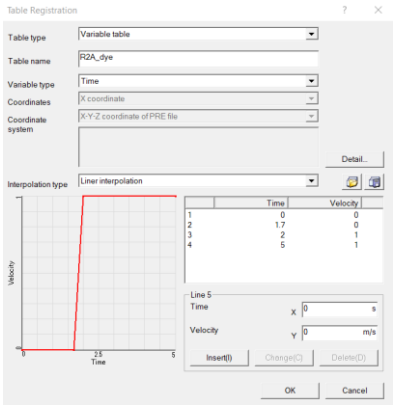
Table Registration
Table type
Variable table
Table name
R2A_dye
Variable type
Time
Coordinates
X coordinate
Coordinate system
X-Y-Z coordinate of PRE file
Detail...
Interpolation type
Liner interpolation
Time
Velocity
1 0 0
2 1.7 0
3 2 1
4 5 1
Line 5
Time
Velocity
X 0 s
Y 0 m/s
Insert(I)
Change(C)
Delete(D)
OK
Cancel

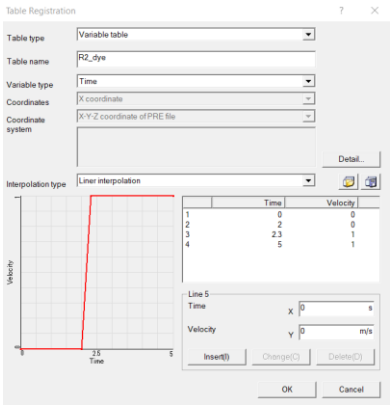
Table Registration
Table type
Variable table
Table name
R2_dye
Variable type
Time
Coordinates
X coordinate
Coordinate system
X-Y-Z coordinate of PRE file
Detail...
Interpolation type
Liner interpolation
Time
Velocity
1 0 0
2 2 0
3 2.3 1
4 5 1
Line 5
Time
Velocity
X 0 s
Y 0 m/s
Insert(I)
Change(C)
Delete(D)
OK
Cancel

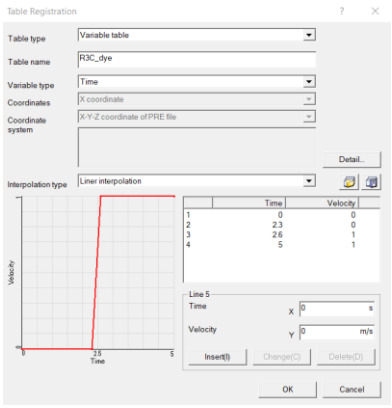
Table Registration
Table type
Variable table
Table name
R3C_dye
Variable type
Time
Coordinates
X coordinate
Coordinate system
X-Y-Z coordinate of PRE file
Detail...
Interpolation type
Liner interpolation
Time
Velocity
1 0 0
2 2.3 0
3 2.6 1
4 5 1
Line 5
Time
Velocity
X 0 s
Y 0 m/s
Insert(I)
Change(C)
Delete(D)
OK
Cancel

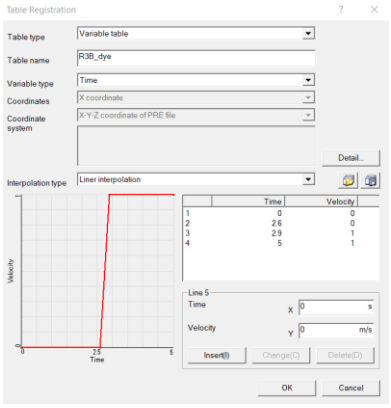
Table Registration
Table type
Variable table
Table name
R3B_dye
Variable type
Time
Coordinates
X coordinate
Coordinate system
X-Y-Z coordinate of PRE file
Detail...
Interpolation type
Liner interpolation
Time
Velocity
1 0 0
2 2.6 0
3 2.9 1
4 5 1
Velocity
Time
Line 5
Time
Velocity
X 0 s
Y 0 m/s
Insert(I)
Change(C)
Delete(D)
OK
Cancel

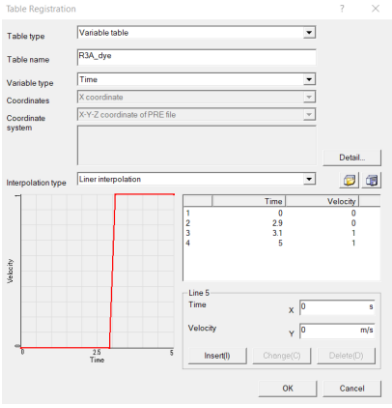
Table Registration
Table type
Variable table
Table name
R3A_dye
Variable type
Time
Coordinates
X coordinate
Coordinate system
X-Y-Z coordinate of PRE file
Detail...
Interpolation type
Liner interpolation
Time
Velocity
1 0 0
2 2.9 0
3 3.1 1
4 5 1
Velocity
Time
Line 5
Time
Velocity
X 0 s
Y 0 m/s
Insert(I)
Change(C)
Delete(D)
OK
Cancel

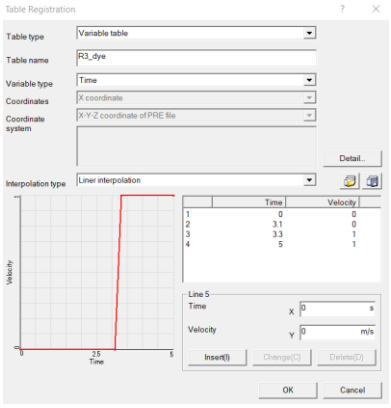
Table Registration
Table type
Variable table
Table name
R3_dye
Variable type
Time
Coordinates
X coordinate
Coordinate system
X-Y-Z coordinate of PRE file
Detail...
Interpolation type
Liner interpolation
Time
Velocity
1 0 0
2 3.1 0
3 3.3 1
4 5 1
Velocity
Time
Line 5
Time
Velocity
X 0 s
Y 0 m/s
Insert(I)
Change(C)
Delete(D)
OK
Cancel

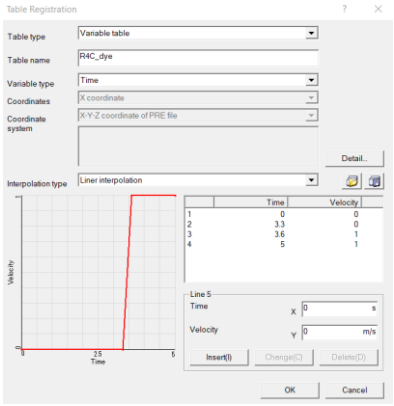
Table Registration
Table type
Variable table
Table name
R4C_dye
Variable type
Time
Coordinates
X coordinate
Coordinate system
X-Y-Z coordinate of PRE file
Detail...
Interpolation type
Liner interpolation
Time
Velocity
1 0 0
2 3.3 0
3 3.6 1
4 5 1
Velocity
Time
Line 5
Time
Velocity
X 0 s
Y 0 m/s
Insert(I)
Change(C)
Delete(D)
OK
Cancel

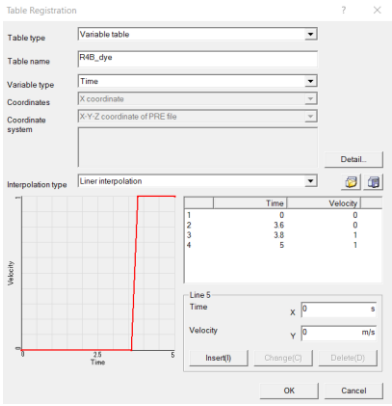
Table Registration
Table type
Variable table
Table name
R4B_dye
Variable type
Time
Coordinates
X coordinate
Coordinate system
X-Y-Z coordinate of PRE file
Detail...
Interpolation type
Liner interpolation
Time
Velocity
1 0 0
2 3.6 0
3 3.8 1
4 5 1
Velocity
Time
Line 5
Time
Velocity
X 0 s
Y 0 m/s
Insert(I)
Change(C)
Delete(D)
OK
Cancel

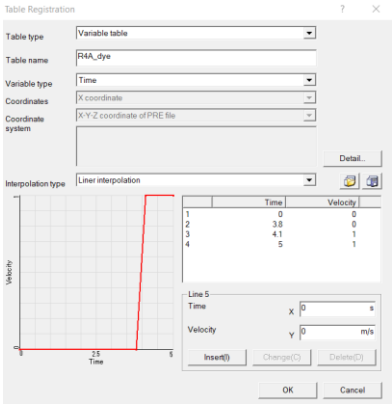
Table Registration
Table type
Variable table
Table name
R4A_dye
Variable type
Time
Coordinates
X coordinate
Coordinate system
X-Y-Z coordinate of PRE file
Detail...
Interpolation type
Liner interpolation
Time
Velocity
1 0 0
2 3.8 0
3 4.1 1
4 5 1
Velocity
Time
Line 5
Time
Velocity
X 0 s
Y 0 m/s
Insert(I)
Change(C)
Delete(D)
OK
Cancel

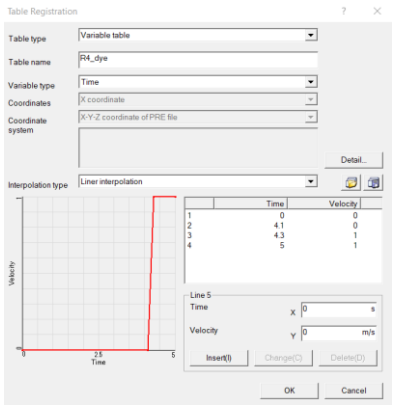
Table Registration
Table type
Variable table
Table name
R4_dye
Variable type
Time
Coordinates
X coordinate
Coordinate system
X-Y-Z coordinate of PRE file
Detail...
Interpolation type
Liner interpolation
Time
Velocity
1 0 0
2 4.1 0
3 4.3 1
4 5 1
Velocity
Time
Line 5
Time
Velocity
X 0 s
Y 0 m/s
Insert(I)
Change(C)
Delete(D)
OK
Cancel

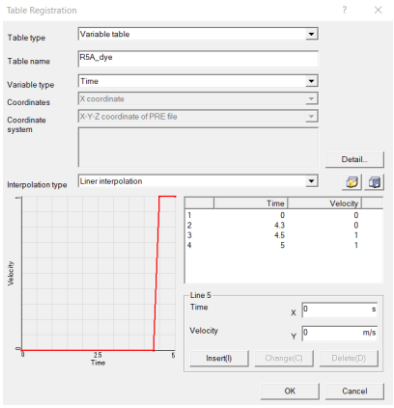
Table Registration
Table type
Variable table
Table name
R5A_dye
Variable type
Time
Coordinates
X coordinate
Coordinate system
X-Y-Z coordinate of PRE file
Detail...
Interpolation type
Liner interpolation
Time
Velocity
1 0 0
2 4.3 0
3 4.5 1
4 5 1
Velocity
Time
Line 5
Time
Velocity
X 0 s
Y 0 m/s
Insert(I)
Change(C)
Delete(D)
OK
Cancel

c. MATLAB script file for creating projective images

```
amp = 1000;
time = 670;
section = 'S1b';

filename = sprintf("T0p%u_%s.csv",time,section);
Im_name = sprintf("Image_T0p%u_%s.tif",time,section);

fprintf("Reading %s\n\n",filename);



T = readtable(filename);
TT = table2array(T);
clear T;

%Im_itp = 237;
%       jtp = 31; itp = 237;
jtp = 104; itp = 119;

Image = zeros(jtp,itp) + 255;

i = 1; j = 1; j_inc = 1; x_first = 0; jcorr = 0;

x = 2; y = 3; z = 4; CN = 5;
sum = 0;



dz = abs(TT(1,z) - TT(2,z));
```

```
II = 255*exp(-1*amp*TT(1,CN)*dz);


for k = 2:numel(TT(:,1))-1
   %=========================================
   % Check to see if x-coordinates are aligned
   %=========================================
   if (TT(k,x) == TT(k-1,x))
      %Previous x-value is equal to current, middle
      if (TT(k,y) == TT(k-1,y))
         %Previous y-value is equal to current, middle
         II = II*exp(-1*amp*TT(k,CN)*dz);
         sum = sum + 1;
      elseif (TT(k,y) == TT(k+1,y))
         %Next value is equal to current, start of next y-value line
         II = II*exp(-1*amp*TT(k,CN)*dz);
         sum = 1;
      elseif (sum == 0)
         %Do nothing, inbetween y-value lines (bad values)
      else
         %Previous y-value is not equal to current. Need to write
         %intensity value to pixel. Reached end of y-value line.
         Image(j+jcorr,i) = II;
% %            fprintf("j = %u , j_inc = %u\n",j,j_inc);
         sum = 0;
         II = 255;
         j = j + j_inc;
      end
```

```
    else
        %Previuos x-value doesn't match current value. Need to see if
        %this is the end of the x-value line.
        if(TT(k-1,x) == TT(k-2,x))
            %We have reached the end of the x-value line and need to
            %output the Intensity to the pixel
            x_first = x_first + 1;
            Image(j+jcorr,i) = II;
% %             fprintf("j = %u , j_inc = %u\n",j,j_inc);
            sum = 0;
            II = 255;
            j = j + 0;
            if (j_inc == 1)
                if (x_first == 1)
                    j = j + 1;
                end
                j_inc = -1;
            else
                j_inc = 1;
            end

            if(x_first == 1)
                jcorr = -1;
            end

            i = i + 1;
        elseif(TT(k,x) == TT(k+1,x))
            %We are at the start of the next x-value line
```

```
            II = II*exp(-1*amp*TT(k,CN)*dz);
            sum = 1;
        else
            %We are in between x-value lines, bad data (do nothing)
        end
    end

end


imshow(uint8(Image));
imwrite(uint8(Image),Im_name,'Compression','none')
```